Important Notice

UNIVERSITY OF CALGARY

Amplitude-variation-with frequency (AVF) analysis of seismic data over anelastic targets

by

Christopher Bird

A DISSERTATION

SUBMITTED TO THE FACULTY OF GRADUATE STUDIES

IN PARTIAL FULFILLMENT OF THE REQUIREMENTS FOR THE

DEGREE OF MASTER OF SCIENCE

DEPARTMENT OF GEOSCIENCE

CALGARY, ALBERTA

April, 2012

UNIVERSITY OF CALGARY

FACULTY OF GRADUATE STUDIES

The undersigned certify that they have read, and recommend to the Faculty of Graduate Studies for acceptance, a dissertation entitled "Amplitude-variation-with frequency (AVF) analysis of seismic data over anelastic targets" submitted by Christopher Bird in partial fulfillment of the requirements for the degree of MASTER OF SCIENCE.

Supervisor,
Dr. Kris Innanen
Department of Geoscience

Co-supervisor,
Dr. Larry Lines
Department of Geoscience

Dr. Don Lawton
Department of Geoscience

Dr. Michael Lamoureux
Department of
Mathematics and
Statistics

Date

Abstract

In this thesis we develop methods of estimating amplitude-variations-with-frequency (AVF) signatures in seismic data for the inversion of anelastic reflectivity. AVF inversion requires estimates of the anelastic reflection coefficient as input and allows for the determination of the target Q value. We start by calibrating a fast S-transform to use as our processing tool to estimate the local spectrum of reflection coefficients. We then modify the AVF inverse theory to operate in the S-domain and find accurate inversion results. In a synthetic data environment we test AVF inversion to manage a prioritized set of issues including random noise, nearby/difficult to isolate events, and a source wavelet. We find AVF inversion, in the presence of these seismic data phenomena, to be a tractable problem. We also identify and examine a target reflection from a VSP data set and observe an AVF signature.

A least-squares approach is developed with the goal of making AVF inversion more robust in the presence of a source wavelet. We also extend the least-squares formalism to oblique incidence. We find the least-squares approach is successful at inverting for Q when an estimate of the wavelet is brought into linear AVF inverse theory. Finally, we study the basic nature of full waveform inversion (FWI) on an anelastic reflection coefficient. We find that the first calculation of the gradient yields an imaginary step at the proper location of the anelastic reflector.

Acknowledgements

I wish to thank my supervisor, Dr. Kris Innanen for his mentorship and guidance. Thanks for investing so much time and effort into helping me learn and grow as a scientist.

I would also like to thank my co-supervisor Dr. Larry Lines for his valuable feedback and insight. Thanks to Mostafa Naghizadeh for his contribution of the fast S-transform code, it was great working with you. Thanks to Laura Baird, Kevin Hall, Kevin Bertram and Rolf Maier for all that they do for us students. I wish to thank all of the CREWES staff and students for the excellent learning environment and collegiate atmosphere.

Thanks to CREWES, Husky Energy Inc., and Schlumberger Canada who acquired the Ross Lake VSP data set which I use in this study. I am grateful to VISTA for their processing software.

Thanks to Zimin Zhang who allowed me to show two of his figures in my thesis.

Much thanks to Peter Gagliardi, Ben Wards, David Cho, Matt McDonald, Glen Young, Steven Kim, Heather Lloyd, Mahdi Mahlmut, Diane Lespinasse, and Melissa Hernandez for insightful discussions, feedback, and assistance with the editing of this thesis.

Thanks to my mother Nancy, my father Brian, my Grandmother Pearl and my brother Tommy for always being there for me. Thanks to my newly expanded family Tony, Pamela, Michael, Angela and Nona. Thanks to all my friends and family.

Thanks to MacGarnagle for being a good buddy.

Finally my love and gratitude to Christina Caponigro.

Dedication

To my lovely wife Christina.

Table of Contents

List of Tables

List of Figures

Chapter 1

Introduction

Absorption is the progressive decay of the highest frequencies of a seismic pulse as it travels through Earth materials (O'Doherty and Anstey, 1971). The effect on the seismic pulse is that the peak amplitude decays (O'Doherty and Anstey, 1971) and the pulse becomes broader. A common measure of absorption is the attenuation coefficient α (Toksoz and Johnston, 1981) which is the exponential decay constant of a plane wave amplitude in a homogenous medium. Another quantitative measure of absorption, or anelasticity, is the dimensionless quality factor, Q. Q is a fundamental rock property defined as the ratio of energy stored to energy dissipated of a seismic wave as it travels through the medium, and is given in Toksoz and Johnston (1981) as

$$Q = \frac{2\pi W}{\Delta W}. \tag{1.1}$$

Here, W is the elastic energy at maximum stress and ΔW is the energy lost per cycle. Q is inversely related to the attenuation coefficient α. Q is an important rock parameter in exploration seismology as knowledge of it allows us to remove the effects of attenuation and increase data resolution (Hargreaves and Calvert, 1991) and Q is also an indicator of rock fluid properties such as fluid saturation, viscosity, permeability etc. (Nur et al., 1980; Vasheghani and Lines, 2009; Vasheghani, 2011).

Q is not easy to measure in the field as it is difficult to isolate the effect of absorption on the seismic pulse from other subsurface mechanisms which attenuate seismic energy (Sheriff and Geldart, 1995). These include geometrical spreading, elastic scattering and the thin bed multiple reflection mechanism which acts as a high cutoff filter and appears very much like absorption (O'Doherty and Anstey, 1971; Spencer et al., 1982). However,

methods of estimating Q from seismic data do exist, such as the centroid frequency method (e.g., Quan and Harris, 1997; Vasheghani and Lines, 2009) and the spectral ratio method (e.g., Hauge, 1981).

It is well established that a contrast in the absorptive properties of two media will cause a frequency dependent reflection coefficient (e.g., White, 1965; Kjartansson, 1979; Chapman et al., 2006; Lines et al., 2008; Quintal et al., 2009; Ren et al., 2009; Innanen, 2011). An amplitude-variation-with-frequency (AVF) method of inverting for Q of a target medium developed by Innanen (2011) exists which requires as input the spectrum of the anelastic reflection coefficient. The estimation of the local spectrum of a reflection coefficient in seismic field data is not a straightforward task. First, it requires a method of time-frequency decomposition which can estimate the local spectra of individual seismic events with high fidelity. Further, all other effects on the spectrum of the reflection event of interest which are not associated with the dispersive reflection coefficient must be accounted for and/or removed. This includes the effect of nearby/difficult-to-isolate events, random noise and the seismic wavelet. If these effects on the amplitude spectrum of the reflection are not accounted for or removed they will mask the effect of the contrast in Q on the reflection coefficient and make it impossible to accurately invert for Q of the target medium.

Much is made in modern reflection seismic literature of AVO-compliant processing, meaning workflows which permit amplitude variation with offset, or angle, to meaningfully and accurately represent reflection at an elastic interface. In this thesis we develop some early steps towards AVF-compliant processing, in which the frequency dependence of reflection processes are preserved and exposed, as well as target property estimation based there upon.

In this thesis, we develop and analyze an AVF processing workflow suitable for implementation on seismic field data. The following steps are taken

1. A fast S-transform algorithm (FST) is calibrated to be our time-frequency decomposition tool used for high fidelity estimates of the local spectrum of a target reflection.

2. A linearized, two-parameter AVF inversion equation is modified to take as input the FST estimate of the spectra of reflection coefficients.

3. Using synthetic data, the effects of nearby/difficult-to-isolate events, random/uncorrelated noise and a source wavelet are examined for their adverse effect on the spectra of anelastic reflection coefficients. Recommendations are made for mitigating these effects.

4. A vertical seismic profile (VSP) survey from the Ross Lake heavy oil field in southeast Saskatchewan is processed using the calibrated FST. Evidence of an AVF signature in a candidate anelastic target is presented and analyzed.

5. Further advancements in the inversion of anelastic reflectivity are developed. First, the AVF invese problem is cast as a least-squares minimization problem to stabilize the inversion accuracy in the presence of seismic data phenomena listed in item (3) which prove problematic. Then we study how full waveform inversion (FWI) works on anelastic reflection data by considering a toy problem.

1.1 Anticipated significance of a robust AVF processing workflow

The ability to estimate Q presents an important problem in exploration seismology for two reasons. Consider a surface seismic experiment in which the target is located underneath an attenuating overburden (Figure 1.1(a)), the attenuation of the overburden decays the peak amplitude of the wave and corrupts AVO measurements. Hence, one reason geophysicists may be concerned in determining Q is that both the resolution of the

structural image and amplitude variation with offset (AVO) analysis are compromised when attenuative effects of Q have degraded the seismic signal. Once Q is known the resolution loss of the structural image may be compensated for by applying Q-compensation (for example, see Reine et al., 2009; Hargreaves and Calvert, 1991). Alternatively, Q-compensation can be performed without explicitly determining the Q structure of the Earth (for details, see Innanen and Lira, 2008, 2010). The degradation of the AVO signature caused by Q attenuation in the overburden can thus be accounted for to produce higher fidelity estimates of elastic parameters. The second reason geophysicists may be interested in Q is that it is a valuable reservoir characterization parameter itself. Consider an elastic overburden overlaying an attenuative target (Figure 1.1(b)). The attenuation of the target alters the AVO response, through its effect on the reflection coefficient, and may be an indicator of rock properties of interest. For instance, it is understood that Q may be closely related to the lithology (Dasgupta and Clark, 1998) and fluid properties of rocks (Quan and Harris, 1997). Some researchers have shown that, in some experiments, Q is more sensitive to permeability than seismic velocities are (Best et al., 1994). Synthetic tests have shown that the modeled reflection coefficients for layers partially saturated with water and gas result in significantly high amplitude reflections due solely to a contrast in Q (Quintal et al., 2009). Also, reflection field data in which dispersion anomalies, associated with a highly absorptive, hydrocarbon charged targets have been observed in the literature (Odebeatu et al., 2006). Field data examples of these dispersive reflections are supported by laboratory experiments (Lines. et al., 2011).

It has been shown that the absorptive properties of heavy-oil reservoirs are proportional to fluid viscosity in the reservoir (Vasheghani and Lines, 2009). This is important as an understanding of the heavy-oil viscosity is a key consideration to production planning (Vasheghani and Lines, 2009). In oil sands reservoirs steam assisted gravity drainage (SAGD) horizontal wells are drilled to inject steam in the reservoir to stimulate produc-

tion. The location of these horizontal wells can be mapped in 4D time lapse seismic data because the flow of heat along the well paths causes higher levels of absorption (Miao et al., 2007). This is strongly suggestive that developing an AVF processing workflow could have a broad and positive impact in exploration geophysics.

1.2 Overview of processing and amplitude estimation tools

In this thesis we will make use of a particular S-transform processing tool. We will use it to analyze an event in a VSP data set, which has been pre-processed to correct for transmission losses, in order to determine Q. In this section we review these two issues and the tools we will use to approach them.

1.2.1 S-transform

Time-frequency decomposition methods provide a means to estimate the local spectrum of seismic data. There are a range of time-frequency decomposition methods with applicability to seismic signal analysis (for example, see Margrave, 1997; Margrave et al., 2003). There are many motivations for performing time-frequency decomposition methods on seismic data. For instance they have been used to facilitate nonstationary seismic processing (for example, see Margrave, 1997; Margrave et al., 2003). The S-transform is one such method. It utilizes a Gaussian window and provides progressive resolution (Stockwell et al., 1996). The S-transform, originally developed by Stockwell et al. (1996), has been generalized in several ways, for instance to include non Gaussian windows (for details see Pinnegar and Mansinha, 2003). The S-transform has been shown to be a special case of the continuous wavelet transform (Gibson et al., 2006). More recently, the S-transform has been shown to be part of a broader class of Fourier-type transforms (Brown et al., 2010). The S-transform has been used for a wide range of reasons in seismic processing and analysis. For instance, Pinnegar and Eaton (2003) use the S-

transform for pre-stack noise attenuation and filtering. Further, Pinnegar (2006) used the S-transform on 3-component seismic data to filter Rayleigh waves from shot records. Seismic attenuation has been estimated using the method of spectral ratios (for example, see Hauge, 1981) by employing the S-transform to estimate the local spectra of seismic events with differing arrival times (Du et al., 2010). Further, the S-tranform has been used in qualitative interpretations of seismic data for thin bed thickness (Tian et al., 2002; Miao et al., 2007) and identification of horizontal wells (Miao et al., 2007). Outside of seismology, the S-transform has been used on ground penetrating radar data to remove wavelet dispersion (Irving and Knight, 2003).

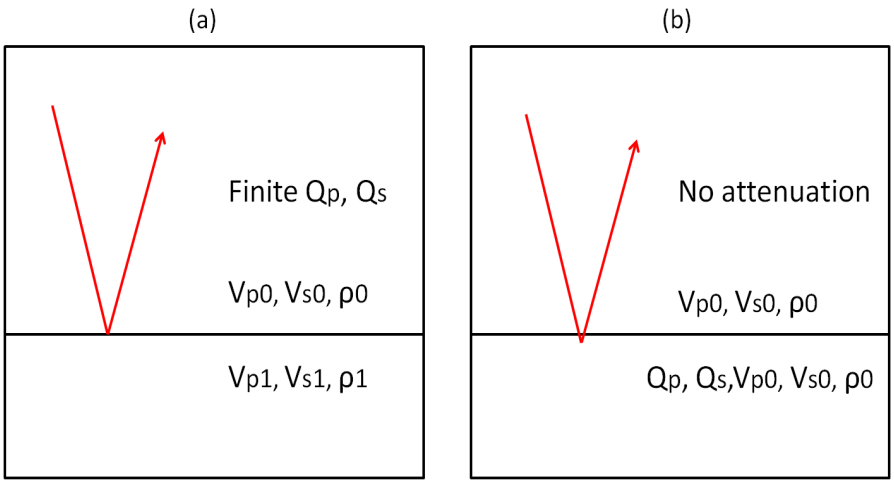

Figure 1.1: Effect of Q on AVO. (a) Attenuation of the wave in the overburden corrupts AVO of the elastic interface; (b) Attenuation of target alters the AVO response itself.

1.2.2 Methods of determining Q from VSP and surface seismic data

A vertical seismic profile (VSP) is a seismic experiment in which a source excited at the surface is measured by receivers located on the wall of a borehole (Hardage, 1985). Vertical seismic profiling, therefore, makes measurements of seismic waves in situ (Spencer

et al., 1982; Stewart, 1983) and should provide deeper understanding of wave propagation within the Earth (Hardage, 1985). Because of this property of VSP experiments, they are ideal for the testing of the AVF inversion processing workflow developed in this thesis. A major difference between a VSP and a surface seismic experiment is that in VSP experiments both the upgoing and downgoing wavefields are recorded by the receivers in the well (Hardage, 1985; Hinds et al., 1996).

Methods of determining Q from VSP data have been an ongoing subject of research with a number of investigators having contributed over the years, see for example (Hauge, 1981; Tonn, 1991; Amundsen and Mittet, 1994; Spencer et al., 1982; Lanning, 1985). The spectral ratio method (explained in detail by Tonn, 1991; Hauge, 1981) is probably the best known method for Q-estimation. When applied to VSP data, the method involves the ratio of amplitude spectra of an event recorded at two different depths. The ratio is proportional to the attenuation of the interval between the two receivers. A serious limitation of the spectral ratio method is the effect of thin bedding near the well (Dietrich and Bouchon, 1985). This is due to the fact that thin bedding acts as a high cutoff frequency filter on seismic signals which appears very similar to the effect of anelastic absorption (O'Doherty and Anstey, 1971). The amplitude decay method involves the ratio of peak amplitudes of a reference wave recorded at two different depths, which are proportional to Q (for details see Tonn, 1991). A drawback of this method is that it is difficult to isolate the effect of attenuation on peak amplitudes from other mechanisms (Sheriff and Geldart, 1995). The centroid frequency method uses the shift in the centroid frequency of a reference wave recorded at two different depths, (for example see Quan and Harris, 1997; Vasheghani and Lines, 2009). Vasheghani and Lines (2009) found that this method has some advantages over the spectral ratio method showing around 10 percent error on VSP data but being much less accurate on synthetic surface seismic. Stewart (1983) developed a full waveform inversion scheme, based on the one-dimensional

acoustic wave equation, to determine attenuation and velocity. Dietrich and Bouchon (1985) developed an iterative procedure of implementing the spectral ratio method which improves estimates of Q when receiver spacing is small. Tonn (1991) compares a number of methods of estimating Q from VSP data including the spectral ratio method (explained in detail by Hauge, 1981; Tonn, 1991) and the amplitude decay method (for details see, Tonn, 1991); He found that no single method is superior and that, depending on noise and recording parameters, some methods are better than others. From the wide array methods for estimating Q from VSP data we can conclude that

1. No method is consistently satisfactory and therefore the development of an AVF workflow to use on VSP data could add value and

2. that these methods provide a natural comparison to which an AVF method should be compared to.

There are a number of examples in the literature of attempts to determine Q from surface seismic reflection data. Dasgupta and Clark (1998) developed a method of applying the spectral ratio method on individual traces of common midpoint (CMP) gathers. The method is called Q-versus-offset (QVO) and involves plotting the spectra of reflectors of individual traces in a CMP gather versus offset, the amplitudes vary with offset because each trace in the gather undergoes a different source-reflector-receiver travelpath and therefore the slope of the amplitude versus offset plot is proportional to the accumulative attenuation in the overburden. Reine et al. (2009) compared variable window time-frequency transforms (such as the S-transform) with fixed window time-frequency transforms such as the short-time Fourier transform (for example, see Hauge, 1981) by applying the QVO method to a surface seismic data set in the Alberta oil sands and found that the variable window transforms produced more stable estimates of Q. Yang et al. (2009) developed a viscoelastic waveform inversion method which jointly inverts both

surface seismic and VSP data by minimizing an objective function which is dependent on both surface seismic and VSP data residuals. Compared to VSP data there are a very limited number of methods for determining Q from surface seismic data and all attempt to invert for Q by analyzing the effect that Q has on the propagation of seismic waves as they travel through Earth material. The novelty of an AVF workflow to estimate Q from surface seismic is that it estimates Q from its effect on the reflection coefficient and not its effect on propagation.

1.3 Outline of thesis

An outline of this thesis will be given here as well as a brief summary of some of the important concepts seen throughout this work.

- In **Chapter 2** we will present a review of the background theory which the rest of this thesis is built on, this will include a presentation of the fast S transform (FST) developed by Brown et al. (2010), a method of estimating the reflection coefficient from VSP data (Lira et al., 2011), and an overview of the theory of AVF inversion of anelastic reflectivity.

- In **Chapter 3** we calibrate the FST to provide high fidelity estimates of local spectra. Limitations of the calibrated FST are examined.

- In **Chapter 4** we build on Chapter 3 by testing the calibrated FST on synthetic anelastic reflection coefficients. The AVF inversion equation is modified to accept input from the FST and inversion accuracy is examined.

- In **Chapter 5** we study practical issues affecting the implementation of AVF inversion on seismic field data. The influence of noise, proximal events and seismic

wavelets on AVF inversion are examined and recommendations are made for mitigating these effects.

- In **Chapter 6** we apply AVF inversion to a VSP field data set from the Ross Lake heavy oil field in south-west Saskatchewan.

- In **Chapter 7** new developments of the inversion of anelastic reflectivity are presented. These include a least-squares framework for AVF inversion which allows for the inclusion of oblique incidence reflections and a seismic wavelet. A study of full waveform inversion (FWI) of anelastic reflection data is also performed.

- **Chapter 8** is the conclusion of this thesis, in which the key results are summarized and recommendations for future work are proposed.

Chapter 2

Theory Review

2.1 Introduction

In this chapter we review key theoretical aspects of the methods which we make use of and build on in this thesis. First an explanation of the fast S-transfrom (FST) by (Brown et al., 2010) is presented as it is the method of time-frequency decomposition used throughout this thesis. This is followed by a review of amplitude-variation-with-frequency AVF inverse theory for Q estimation. We demonstrate how the theory characterizes dispersive reflection coefficients associated with a contrast in Q, and how it permits determination of Q given measurements of the dispersive reflection coefficient. Finally, we review a method developed by Lira et al. (2011) for determining reflection coefficients from vertical seismic profile (VSP) data.

2.2 Fast S-transform

The Fourier transform (FT) does not expose the time-varying spectral content of a signal. This may be problematic because a seismic signal is often non-stationary, meaning its frequency content changes with time. The S-transform is a time-frequency decomposition method utilizing a Gaussian window to provide progressive resolution (Brown et al., 2010). The S-transform of a time signal $g(t)$ is defined by Stockwell et al. (1996) and presented by Brown et al. (2010) as

$$S(\tau, f) = \int_{-\infty}^{\infty} g(t) \frac{|f|}{\sqrt{2\pi}} e^{\frac{-(\tau-t)^2 f^2}{2}} e^{-i2\pi f t} dt, \tag{2.1}$$

where τ and f are the time co-ordinate and frequency co-ordinate of the S-domain respectively and $\frac{|f|}{\sqrt{2\pi}}e^{\frac{-(\tau-t)^2f^2}{2}}$ is the Gaussian window. Using equation (2.1) the S-transform can be calculated directly from the time domain input. It is also possible to calculate the S-transform from frequency domain input. By taking the Fourier transform along the τ axis of the S-domain we generate what Brown et al. (2010) refer to as the α-domain:

$$\alpha(f', f) = \int_{-\infty}^{\infty} S(\tau, f)e^{-i2\pi f'\tau}d\tau, \tag{2.2}$$

where f' is a frequency-shift axis generated by taking the Fourier transform along the τ axis of the S-domain. The α-domain may also be expressed as (Brown et al., 2010)

$$\alpha(f', f) = G(f' + f)W(f', f). \tag{2.3}$$

Here G($f' + f$) is a matrix where each row is the Fourier transform of the signal G(f) shifted by a frequency increment f'. The α-domain is generated by multiplying this matrix by the Fourier transform of the window function W(f',f), which is given by the equation:

$$W(f', f) = \int_{-\infty}^{\infty} \frac{|f|}{\sqrt{2\pi}}e^{\frac{-(\tau-t)^2f^2}{2}}e^{-i2\pi f'(\tau-t)}d(\tau - t). \tag{2.4}$$

Once the α-domain is constructed, the S-domain is obtained by performing an inverse Fourier transform along the f'-axis of the α-domain. The equation for transforming to the S-domain from the α-domain is given in (Brown et al., 2010) as

$$S(\tau, f) = \int_{-\infty}^{\infty} \alpha(f', f)e^{i2\pi f'\tau}df'. \tag{2.5}$$

In Figure 2.1, we illustrate how the S-domain may be constructed from the α-domain with an example time signal. Similar examples can be seen in Brown et al. (2010); Naghizadeh and Innanen (2010). In Figure 2.1(a) a time signal which is a sum of two harmonics of 10 Hz and 50 Hz is illustrated. The FT of this signal is shown in Figure 2.1(b). G($f' + f$), a matrix in which every row is the FT of the original signal shifted by

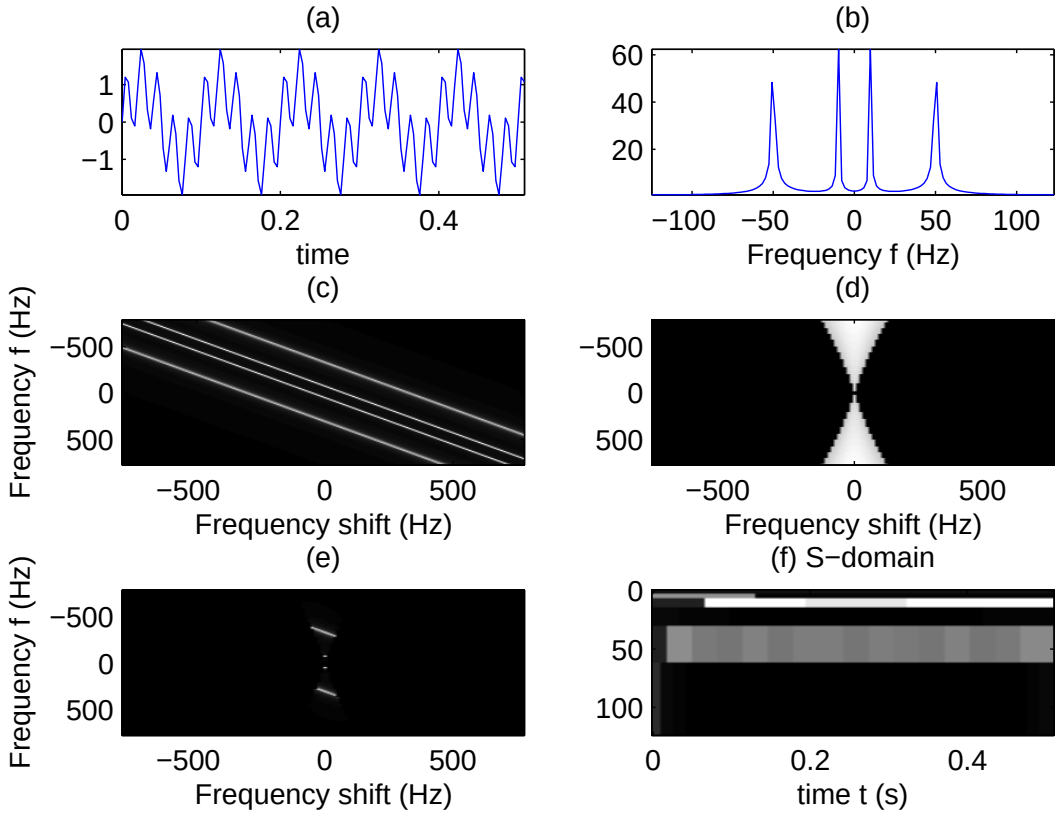

Figure 2.1: Construction of S-domain from α domain. (a) An example time signal produced by the sum of two harmonics of 10 Hz and 50 Hz. (b) The Fourier transform of the time signal. (c) $G(f'+f)$ which consists of shifted versions of (b). (d) $W(f',f)$, the Fourier transform of the window function. (e) The α-domain obtained by mutliplying $G(f'+f)$ with $W(f',f)$. (f) The S-domain of the time signal in (a). After Brown et al. (2010) and Naghizadeh and Innanen (2010).

f', is shown in Figure 2.1(c). W(f',f), the FT of the window function is shown in Figure 2.1(d). The α-domain, Figure 2.1(e), is achieved by multiplying every row of G(f' + f) with every row of W(f',f). Finally, taking the inverse fast Fourier transform (IFFT) along f', expressed by (2.5), yields the S-domain of the original signal (Figure 2.1(f)). Notice that the S-domain correctly represents the signal as stationary and containing two frequencies, 10 Hz and 50 Hz.

2.2.1 Fast S-transform algorithm

As presented by Brown et al. (2010) and implemented by Naghizadeh and Innanen (2010) the ST can be calculated non-redundantly by segmenting in the α-domain, with higher frequencies being coarsely sampled and lower frequencies being finely sampled. The α-domain is divided into segments, with large segments for high frequencies and small segments for low frequencies (Brown et al., 2010). Only one frequency is sampled at the centre of each segment and these values are used for all frequencies enclosed by the segment (Brown et al., 2010). Finally, to generate the S-transform an IFFT is applied to each segment. The IFFT of each segment populates its corresponding frequency range in the S-domain for the entire τ axis. Since at larger frequencies we have larger segments, we gain time resolution but lose frequency resolution. For low frequencies we gain high frequency resolution but have poor time resolution. This method of segmenting the α-domain makes the calculation of the ST fast and non-redundant and yields the fast S-transform (FST). Consider Figure 2.2. In it, the segmentation and sampling of the α-domain is illustrated. The α-domain segments are shown with solid black lines and the dashed lines correspond to the sampled frequency in each segment. Now if we unshift the frequency-shift axis of the α-domain we can see a relationship between this sampling scheme and the frequency domain of the original signal (Figure 2.3). Notice that the horizontal-axis is no longer a frequency-shift axis but is now just a frequency axis and

that the chosen sampling scheme covers the entire frequency domain. All that is required for the construction of the S-domain then is to take the Fourier transform of the signal, partition the frequency domain of the signal according to the described sampling scheme, and then IFFT each segment to populate the S-domain (Figure 2.4). We mention here that Brown et al. (2010) presented the FST as a series of steps, they did not express the FST algorithm as an equation. A valuable topic of future research would be to derive an equation to express the FST.

2.3 Q models

There are a range of Q models designed to characterize the attenuation of seismic waves in the Earth. Viscoelastic theory is a common approach to model attenuation. In this model, a body's response to stress occurs with a time delay caused by the viscous behavior of the material (Vasheghani and Lines, 2009). Viscoelastic models include the Maxwell, Kelvin-Voigt, and Zener models (Vasheghani and Lines, 2009). A problem with viscoelastic models is that they produce Q values which are dependent on frequency (Vasheghani and Lines, 2009) while most observations suggest that Q is independent of frequency in the seismic frequency range (Toksoz and Johnston, 1981; Kjartansson, 1979). Kjartansson (1979) contains a table summarizing a number of different Q models including constant Q and nearly-constant Q models. In this thesis we will adopt a nearly constant Q model, described by Aki and Richards (2002), which includes a convenient dispersion relationship.

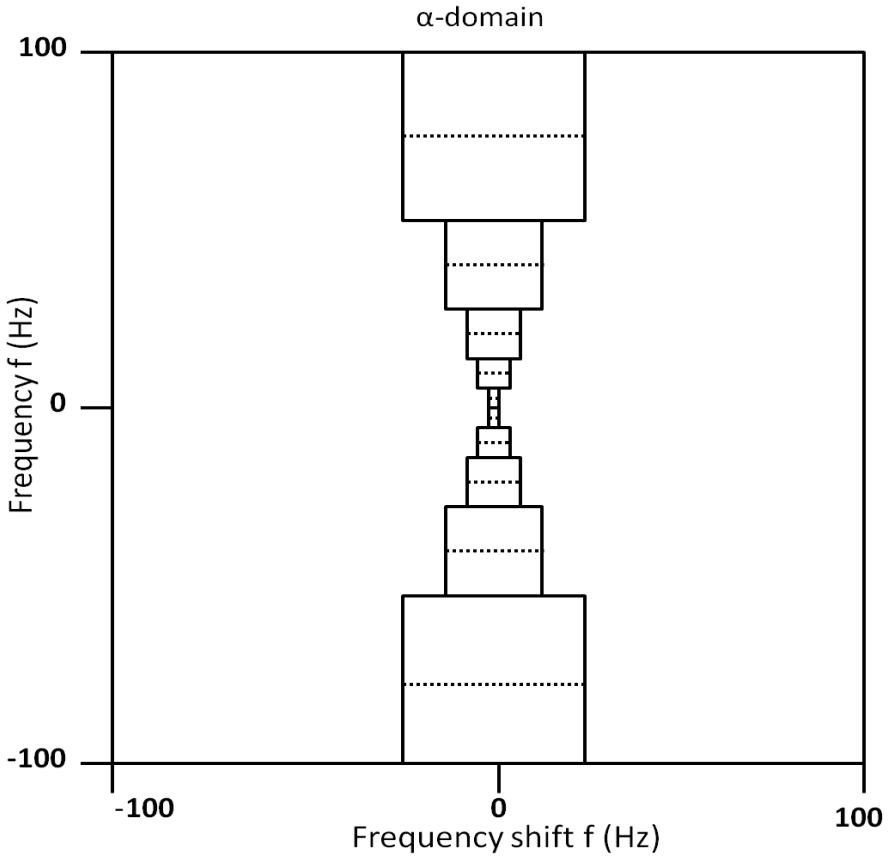

Figure 2.2: Sampling of the α-domain. The solid black lines illustrate how the α-domain is divided into segments. The dashed line corresponds to the frequency of each segment to be sampled. After Brown et al. (2010).

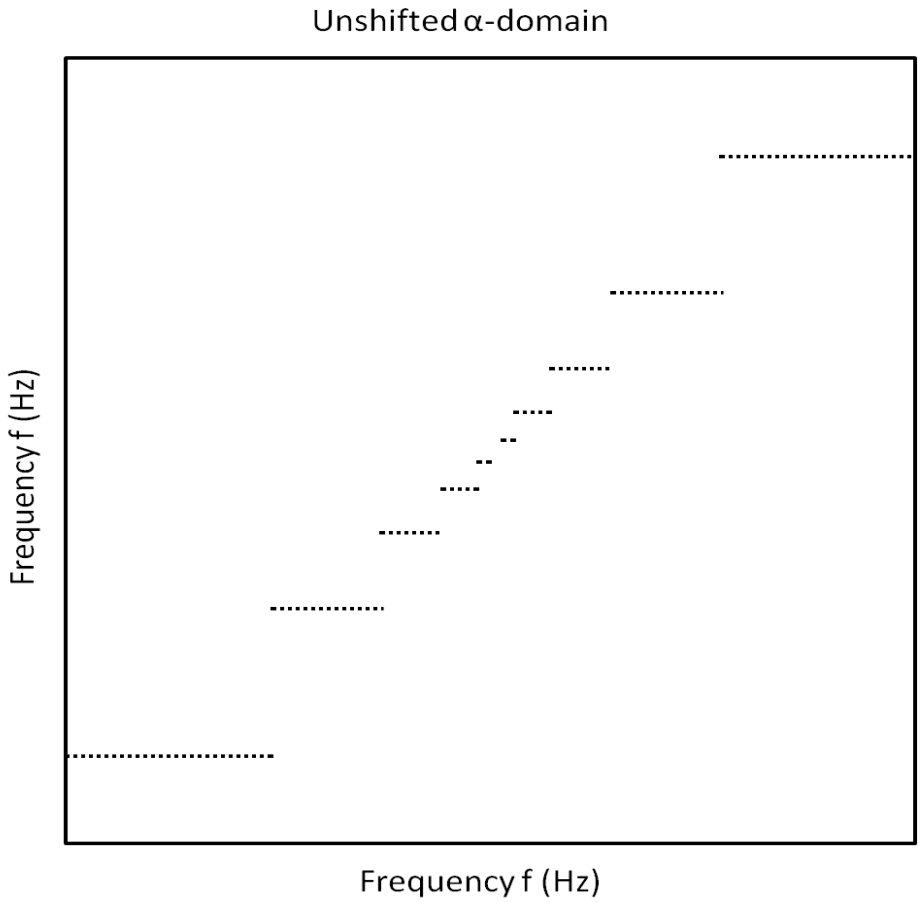

Figure 2.3: Unshifted α-domain, highlighting how the S-domain may be constructed non-redundantly. After Brown et al. (2010).

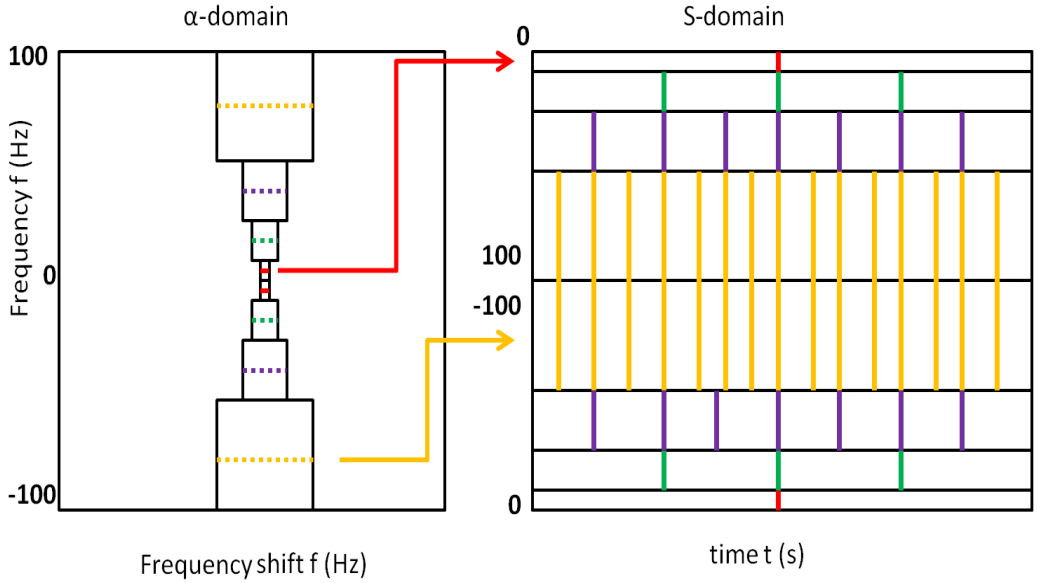

Figure 2.4: Constructing the S-domain from the α-domain. An IFFT is performed on the samples chosen to represent each segment.

2.4 Anelastic reflection coefficients

Consider a plane wave incident upon a planar boundary whose normal is the vertical (z) axis, and separating two homogeneous layers. The reflection coefficient is given by

$$R = \frac{k_{z_0} - k_{z_1}}{k_{z_0} + k_{z_1}}, \tag{2.6}$$

where R is the reflection coefficient, k_{z_0} is the vertical wavenumber in the layer above the interface and k_{z_1} is the vertical wavenumber in the layer below the interface. In order to model anelastic reflection coefficients, we use an expression for the wavenumber which includes a model for nearly constant Q described by Aki and Richards (2002) as

$$k = \frac{\omega}{c}\left(1 + \frac{i}{2Q} - \frac{\log(\omega/\omega_r)}{\pi Q}\right). \tag{2.7}$$

Here Q is the quality factor, ω is the angular frequency, ω_r is a reference frequency, and c is the phase velocity at frequency ω_r. For waves at normal incidence the expression for wavenumber k given in equation (2.7) can be used as the vertical wavenumber k_z in equation (2.6). Hence, the equation which models anelastic reflection coefficients in one dimension is obtained by inserting equation (2.7) into equation (2.6). This is represented by

$$R(\omega) = \frac{\left[\frac{1}{c_0}(1 + \frac{i}{2Q_0} - \frac{\log(\omega/\omega_r)}{\pi Q_0}) - \frac{1}{c_1}(1 + \frac{i}{2Q_1} - \frac{\log(\omega/\omega_r)}{\pi Q_1})\right]}{\left[\frac{1}{c_0}(1 + \frac{i}{2Q_0} - \frac{\log(\omega/\omega_r)}{\pi Q_0}) + \frac{1}{c_1}(1 + \frac{i}{2Q_1} - \frac{\log(\omega/\omega_r)}{\pi Q_1})\right]}, \tag{2.8}$$

where the reflection coefficient, $R(\omega)$, is now complex and frequency dependent. Equation (2.8) is the general form for the normal incidence reflection coefficient in anelastic media. Consider the situation where an elastic overburden (infinite Q) is overlaying a highly anelastic target (low Q). Equation (2.8) becomes

$$R(\omega) = \frac{\left[\frac{1}{c_0} - \frac{1}{c_1}(1 + \frac{i}{2Q_1} - \frac{\log(\omega/\omega_r)}{\pi Q_1})\right]}{\left[\frac{1}{c_0} + \frac{1}{c_1}(1 + \frac{i}{2Q_1} - \frac{\log(\omega/\omega_r)}{\pi Q_1})\right]}. \tag{2.9}$$

Now if we make the following substitutions (from Innanen, 2011), $F(\omega) = \frac{i}{2} - \frac{1}{\pi}\log(\omega/\omega_r)$, $a_C = 1 - \frac{c_0^2}{c_1^2}$ and $a_Q = \frac{1}{Q_1}$ we obtain

$$R(\omega) = \frac{1 - \sqrt{1-a_C}\,(1 + a_Q F(\omega))}{1 + \sqrt{1-a_C}\,(1 + a_Q F(\omega))}. \tag{2.10}$$

We then take the Taylor series expansion of $\sqrt{1-a_C}$ to obtain

$$R(\omega) = \frac{1 - \left(1 - \frac{1}{2}a_C + \frac{1}{8}a_C^2 + \ldots\right)(1 + a_Q F(\omega))}{1 + \left(1 - \frac{1}{2}a_C + \frac{1}{8}a_C^2 + \ldots\right)(1 + a_Q F(\omega))}, \tag{2.11}$$

from which we obtain

$$\begin{aligned} R(\omega) &= \frac{1 - \left(1 + a_Q F(\omega) - \frac{1}{2}a_C - \frac{1}{2}a_C a_Q F(\omega) + \ldots\right)}{1 + \left(1 + a_Q F(\omega) - \frac{1}{2}a_C - \frac{1}{2}a_C a_Q F(\omega) + \ldots\right)} \\ &= \frac{\left(-\frac{1}{2}a_Q F(\omega) + \frac{1}{4}a_C + \frac{1}{4}a_C a_Q F(\omega) + \ldots\right)}{1 - \left(-\frac{1}{2}a_Q F(\omega) + \frac{1}{4}a_C + \frac{1}{4}a_C a_Q F(\omega) + \ldots\right)} \\ &= \frac{\Omega}{1-\Omega}, \end{aligned} \tag{2.12}$$

where $\Omega = \left(-\frac{1}{2}a_Q F(\omega) + \frac{1}{4}a_C + \frac{1}{4}a_C a_Q F(\omega) + \ldots\right)$. We can further form a Taylor series for $R(\omega)$ by expanding around Ω to obtain

$$\begin{aligned} R(\omega) &= \Omega\,(1 + \Omega + \ldots) = \Omega + \Omega^2 + \ldots \\ &= \left(-\frac{1}{2}a_Q F(\omega) + \frac{1}{4}a_C + \ldots\right) + \left(-\frac{1}{2}a_Q F(\omega) + \frac{1}{4}a_C + \ldots\right)^2. \end{aligned} \tag{2.13}$$

Finally, linearizing equation (2.13) assuming small a_C and a_Q gives

$$R(\omega) \approx -\frac{1}{2}a_Q F(\omega) + \frac{1}{4}a_C, \tag{2.14}$$

where a_Q and a_C are the dimensionless perturbations measuring the contrasts across the boundary in Q and acoustic seismic velocity respectively. $F(\omega)$ is a known function reflecting our particular choice of nearly-constant Q model. Equation (2.14) defines the forward problem of calculating $R(\omega)$ given a_C and a_Q. We use a simple model in this thesis, in which the reflection coefficient is dependent only upon contrasts in wavespeed and Q. The reason for this is that we are developing the application AVF inverse theory

to field data from the ground up and so we begin with a simple model and we are free to add complexity as needed. Further, considering a simple model for reflection coefficients like this exposes the basic nature of the AVF problem. As AVF inversion is built upon in the future (ie. for oblique incidence) the effects of density are readily included.

The goal of AVF inversion is to determine a_Q or a_C from measurements of $R(\omega)$. Equation (2.14) contains two unknowns, a_C and a_Q. If we can determine $R(\omega)$ for two different frequencies, ω_1 and ω_2, we can take the difference between $R(\omega_1)$ and $R(\omega_2)$ and obtain an expression for a_Q:

$$a_Q \approx -2\left(\frac{R(\omega_2)-R(\omega_1)}{F(\omega_2)-F(\omega_1)}\right). \tag{2.15}$$

2.4.1 Using amplitude spectra

Implementing equation (2.15) to solve for a_Q, in practise, amounts to taking the difference between the real part of $R(\omega)$ and the real part of $F(\omega)$:

$$\begin{aligned}
a_Q &\approx -2\left(\frac{R(\omega_2)-R(\omega_1)}{F(\omega_2)-F(\omega_1)}\right)\\
&\approx -2\left(\frac{\left(-\frac{1}{2}a_Q F(\omega_2)+\frac{1}{4}a_C\right)-\left(-\frac{1}{2}a_Q F(\omega_1)+\frac{1}{4}a_C\right)}{F(\omega_2)-F(\omega_1)}\right)\\
&\approx -2\left(\frac{\left(-\frac{1}{2}a_Q\left[\frac{i}{2}-\frac{1}{\pi}\log(\omega_2/\omega_r)\right]+\frac{1}{4}a_C\right)-\left(-\frac{1}{2}a_Q\left[\frac{i}{2}-\frac{1}{\pi}\log(\omega_1/\omega_r)\right]+\frac{1}{4}a_C\right)}{\left[\frac{i}{2}-\frac{1}{\pi}\log(\omega_2/\omega_r)\right]-\left[\frac{i}{2}-\frac{1}{\pi}\log(\omega_1/\omega_r)\right]}\right)\\
&\approx -2\left(\frac{\left(-\frac{i}{4}a_Q+\left[\frac{1}{2\pi}\log(\omega_2/\omega_r)a_Q+\frac{1}{4}a_C\right]\right)-\left(-\frac{i}{4}a_Q+\left[\frac{1}{2\pi}\log(\omega_1/\omega_r)a_Q+\frac{1}{4}a_C\right]\right)}{\left[\frac{i}{2}-\frac{1}{\pi}\log(\omega_2/\omega_r)\right]-\left[\frac{i}{2}-\frac{1}{\pi}\log(\omega_1/\omega_r)\right]}\right)\\
&\approx -2\left(\frac{\left[\frac{1}{2\pi}\log(\omega_2/\omega_r)a_Q+\frac{1}{4}a_C\right]-\left[\frac{1}{2\pi}\log(\omega_1/\omega_r)a_Q+\frac{1}{4}a_C\right]}{\left[-\frac{1}{\pi}\log(\omega_2/\omega_r)\right]-\left[-\frac{1}{\pi}\log(\omega_1/\omega_r)\right]}\right)\\
&\approx -2\left(\frac{\Re[R(\omega_2)]-\Re[R(\omega_1)]}{\Re[F(\omega_2)]-\Re[F(\omega_1)]}\right).
\end{aligned} \tag{2.16}$$

Here $\Re$ denotes the real part. In the coming chapters we will use estimates of $R(\omega)$ obtained from the FST. It will be much more convenient for us to extract the amplitude spectrum of $R(\omega)$ from the FST. Further, when we examine VSP data in Chapter 6,

we will use a method of estimating reflection coefficients which requires as input the amplitude spectra of primary and direct arrivals (described in the following section). As we see in equation 2.16 the real part of $R(\omega)$, $\Re[R(\omega)]$, is

$$\Re[R(\omega)] \approx \frac{1}{2\pi}\log(\omega/\omega_r)a_Q + \frac{1}{4}a_C. \tag{2.17}$$

Now, we find an expression for the amplitude spectrum of $R(\omega)$, $|R(\omega)|$, given by

$$\begin{aligned} |R(\omega)| &\approx \sqrt{\Re[R(\omega)]^2 + \Im[R(\omega)]^2} \\ &\approx \sqrt{\left(\frac{1}{2\pi}\log(\omega/\omega_r)a_Q + \frac{1}{4}a_C\right)^2 + \left(\frac{a_Q}{4}\right)^2} \end{aligned} \tag{2.18}$$

where $\Im[R(\omega)] \approx \frac{a_Q}{4}$ is the imaginary part of $R(\omega)$. Now if the imaginary part of $R(\omega)$ is small then we can drop it from equation (2.22) and obtain

$$|R(\omega)| \approx \sqrt{\Re[R(\omega)]^2} \approx \Re[R(\omega)] \tag{2.19}$$

To illustrate the accuracy of equation (2.19) the amplitude spectra for a number of dispersive reflection coefficients, for varying contrasts in Q, are shown in Figure 2.5. Each panel in Figure 2.5 shows the exact amplitude spectrum of the dispersive reflection coefficient (red), calculated using equation (2.6), associated with a large contrast in Q and velocity. It also shows the corresponding elastic reflection coefficient in blue. The caption in Figure 2.5 lists the value of Q of the target medium. The amplitude spectra of the dispersive reflection coefficients shown in Figure 2.5 serve as input into equation (2.15) to perform AVF inversion. Figure 2.6 shows the result of inverting for Q using equation (2.15) on the amplitude spectra of reflection coefficients, such as shown in Figure 2.5. The inverted Q value is in red and the blue curve represents the true Q values. The accuracy of the inversion indicates that the amplitude spectrum of the reflection coefficient is a good approximation to the real part of the reflection coefficient.

Further, this inversion is a straightforward task given access to exact values of the reflection coefficient at two or more frequencies. In real data, we require a method of

time-frequency decomposition to isolate the reflection of interest from all other events in the recorded data. Further, the presence of random/uncorrelated noise, proximal events and a seismic wavelet must be expected to have an effect on the spectra of dispersive reflection coefficients. These issues must be contended with before AVF inversion can be carried out. In this thesis, we examine and address these problems.

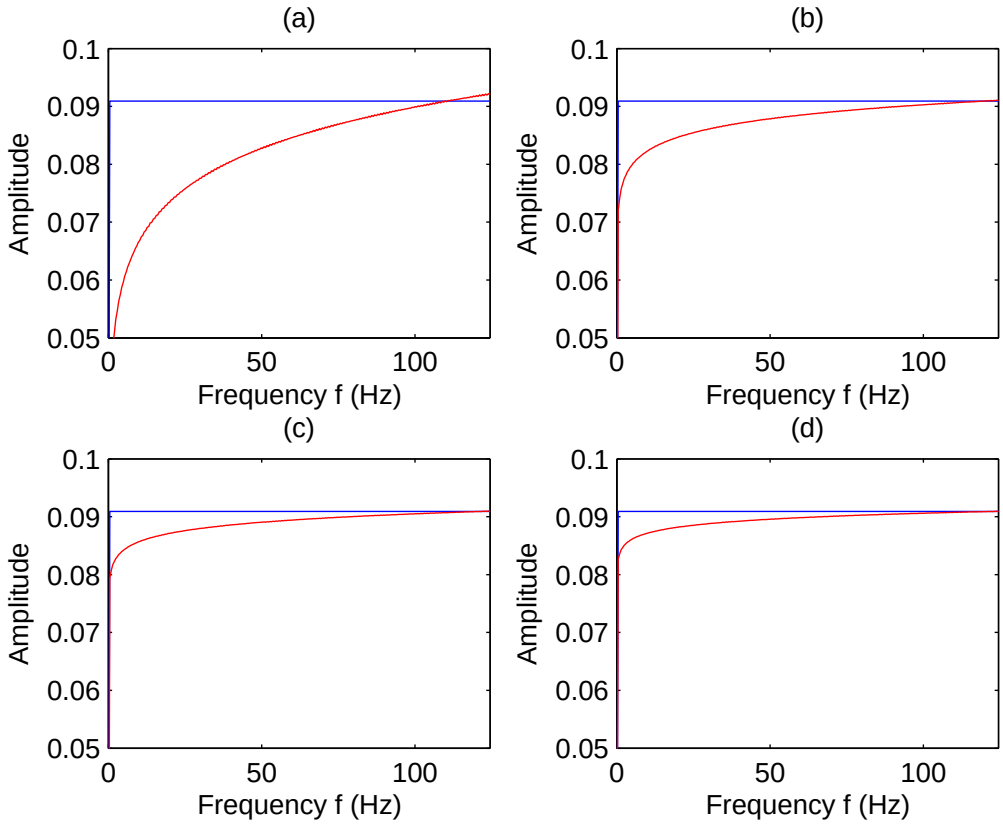

Figure 2.5: Dispersive reflection coefficients. In blue is the amplitude spectrum of a frequency independent elastic reflection coefficient. In red, the amplitude spectrum of the dispersive reflection coefficient associated with a large contrast in Q. $Q_0 = \infty$, $c_0 = 1500m/s$, $c_1 = 1800m/s$. In (a) $Q_1 = 15$. In (b) $Q_1 = 45$. In (c) $Q_1 = 75$ and in (d) $Q_1 = 105$.

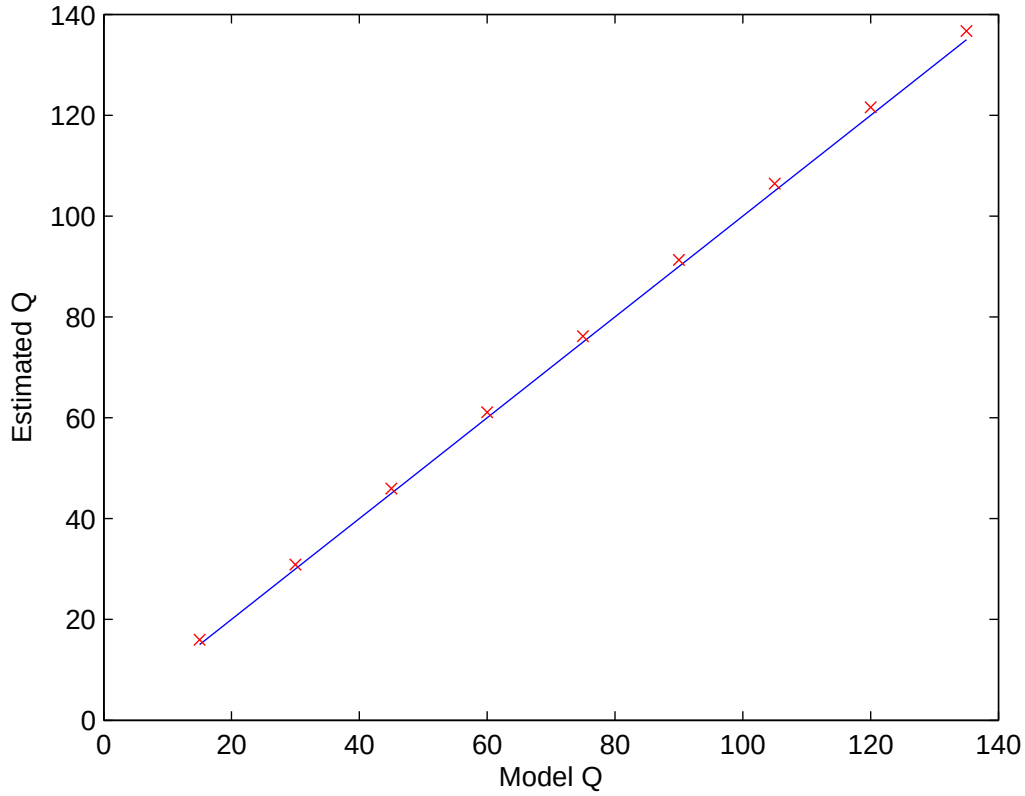

Figure 2.6: Inversion for Q from the reflection coefficients shown in Figure 2.5. The blue line is the actual target Q value and the red x's are the inversion result.

2.5 A method for determining reflection coefficients from VSP data

In Chapter 6 of this thesis, we apply our AVF workflow to a VSP data set from the Ross Lake heavy oil field in south-west Saskatchewan. In order to apply the AVF workflow, we will require a method of estimating the reflection coefficient of our chosen target reflector. We describe here a method developed by Lira et al. (2011) which allows for the recovery of the reflection coefficient in VSP data. The method is related to the work of Hardage (1985) and Stewart (1983).

We consider a zero offset VSP experiment in two geophysical settings; one for layered acoustic media and the other for anelastic media (Figure 2.7). In this simple model the

Earth has been divided into n layers where the nth layer is located between the nth and $(n+1)$th interface. In both cases a target reflector is located at depth z_n, and a receiver at depth z is located above the reflector. In the VSP geometry illustrated in Figure 2.8 the receiver at z will record a primary reflection from the interface at z_n and a direct wave which travels directly from the source to the receiver.

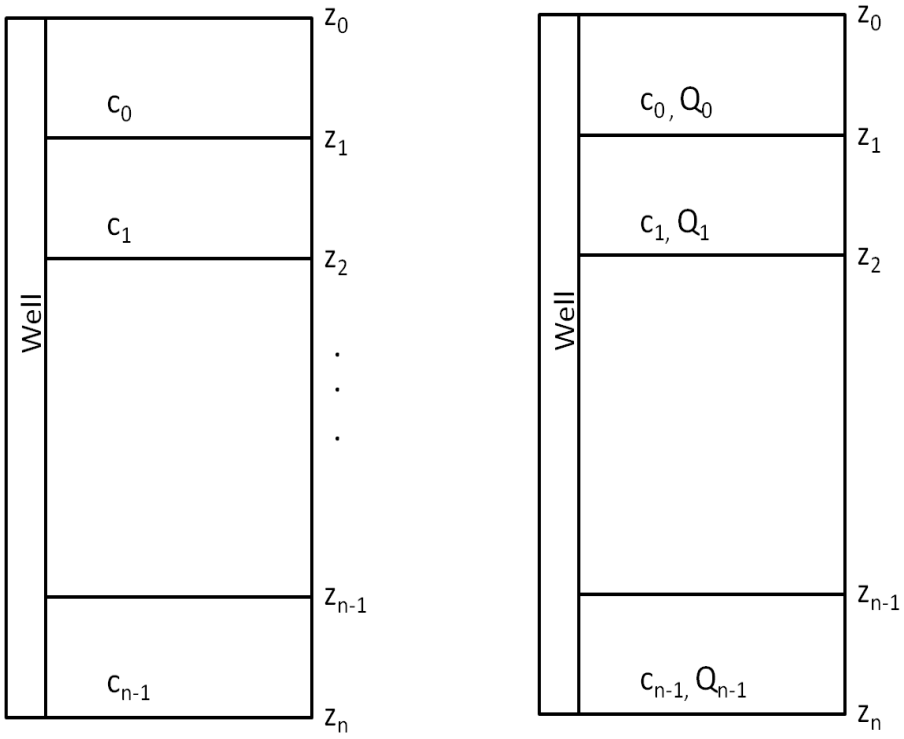

Figure 2.7: VSP geometry and idealized Earth model consisting of flat layers. On the left: elastic model. On the right: anelastic model. Image adapted from Lira et al. (2011).

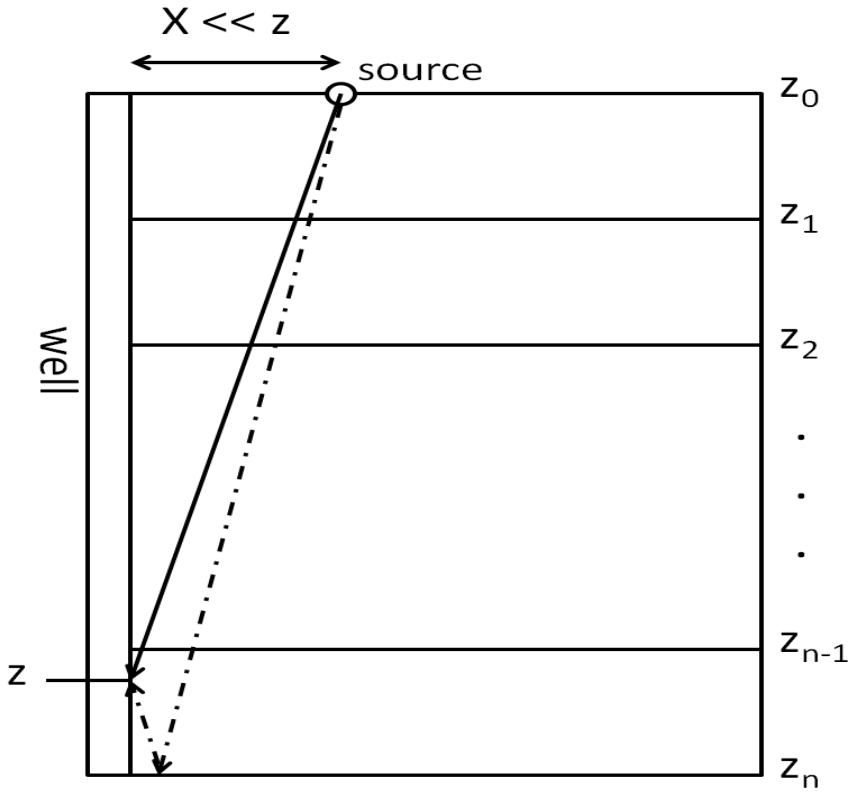

Figure 2.8: VSP survey showing the direct wave (solid black line) and reflected primary (dashed line). Image adapted from Lira et al. (2011).

2.5.1 Elastic formulation

For the elastic case we can mathematically describe the primary event in the frequency domain as

$$P_n(\omega) = e^{ik_0(z_1-z_0)}T_{01}e^{ik_1(z_2-z_1)}T_{12}e^{ik_2(z_3-z_2)} \times \ldots \times R_n e^{(ik_{n-1}(2z_n-z_{n-1}-z))} \tag{2.20}$$

where P_n is the recorded primary, k_n is the wavenumber in the nth layer, T_{ij} is the transmission coefficient from layer i to layer j and R_n is the reflection coefficient of the

target. The amplitude spectrum of the primary is

$$|P_n| = \left[T_{01}T_{12}\ldots T_{(n-1)(n)}\right] R_n. \tag{2.21}$$

In order to isolate the reflection coefficient R_n from the primary we need to remove the effect of the transmission and propagation through the overburden. In order to achieve this let us look at the expression describing the direct wave in the frequency domain

$$D(\omega) = e^{ik_0(z_1-z_0)}T_{01}e^{ik_1(z_2-z_1)}T_{12}e^{ik_2(z_3-z_2)} \times \ldots \times e^{ik_{n-1}(z-z_{n-1})}, \tag{2.22}$$

where D is the direct arrival. The amplitude spectrum of D is then

$$|D| = \left[T_{01}T_{12}\ldots T_{(n-1)(n)}\right]. \tag{2.23}$$

Hence, equation (2.23) prescribes the operator OP that we apply to the primary $P_n(\omega)$ to obtain an estimate of the reflection coefficient. This operator is simply

$$OP = \frac{1}{|D|}. \tag{2.24}$$

We can apply this operator to the primary event to obtain an estimate of the reflection coefficient which we will denote as P_C for corrected primary, given by

$$P_C = OP \times |P_n| = \frac{1}{|D|} \times |P_n| = R_n. \tag{2.25}$$

2.5.2 Anelastic formulation

The formulation of an operator to correct the primary is more complicated when the overburden is anelastic. This is because absorption acts on the wave as it travels through the medium. Continuing to use the Q model given in Aki and Richards (2002), in which the wavenumber k is replaced by a complex $\tilde{k}$, we have

$$\tilde{k}_j = \frac{\omega}{c_j}\left[1 + \frac{F(\omega)}{Q_j}\right], \tag{2.26}$$

where $\tilde{k}_j$ is the complex wavenumber in layer j, ω is radial frequency, c_j is the seismic wavespeed in layer j, Q_j is the value of Q in layer j, and $F(\omega) = \frac{i}{2} - \frac{1}{\pi}\log(\omega/\omega_r)$ is a known function with ω_r being a reference frequency. By replacing k_j with $\tilde{k}_j$ in equation (2.20) we obtain the following expression for the anelastic primary

$$P_n(\omega) = e^{i\tilde{k}_0(z_1-z_0)}\mathcal{T}_{01}e^{i\tilde{k}_1(z_2-z_1)}\mathcal{T}_{12}e^{i\tilde{k}_2(z_3-z_2)}\mathcal{T}_{23} \times \ldots \times \mathcal{T}_{(n-1)(n)}e^{i\tilde{k}_{n-1}(2z_n-z_{n-1}-z)}R_n(\omega), \tag{2.27}$$

where the absorptive transmission coefficients $\mathcal{T}_{ij}$ are given in Lira et al. (2010) as

$$\begin{aligned}\mathcal{T}_{ij} = &\left[\frac{2c_j\left(1+\frac{F(\omega)}{Q_j}\right)^{-1}}{c_i\left(1+\frac{F(\omega)}{Q_i}\right)^{-1}+c_j\left(1+\frac{F(\omega)}{Q_j}\right)^{-1}}\right] \\ &\times \underbrace{e^{-\frac{\omega}{2Q_ic_i}(z_i-z_{(i-1)})}}_{\text{attenuation component}}\ e^{\frac{i\omega}{\pi Q_ic_i}\log(\frac{\omega}{\omega_0})(z_i-z_{(i-1)})}.\end{aligned} \tag{2.28}$$

Here $e^{-\frac{\omega}{2Q_ic_i}\left(z_i-z_{(i-1)}\right)}$ acts to attenuate the event. Using these definitions for transmission coefficients the direct wave is written as

$$D(\omega) = e^{i\tilde{k}_0(z_1-z_0)}\mathcal{T}_{01}e^{i\tilde{k}_1(z_2-z_1)}\mathcal{T}_{12}e^{i\tilde{k}_2(z_3-z_2)}\mathcal{T}_{23}\ldots e^{i\tilde{k}_{n-1}(z-z_{n-1})}. \tag{2.29}$$

In the same manner as for the acoustic formulation, we can define the operator for the anelastic case, OP_{an} as

$$OP_{an} = \frac{1}{\mathcal{T}_{01}\mathcal{T}_{12}\mathcal{T}_{23}\ldots e^{i\tilde{k}_{n-1}(z-z_{n-1})}}. \tag{2.30}$$

If we apply equation (2.30) to the primary we obtain an estimate of the reflection coefficient. Denoting this corrected primary PC_{an} we have

$$PC_{an} = OP_{an} \times Pn(\omega) = R_n(\omega)e^{i\tilde{k}_{n-1}2(z_n-z)} \tag{2.31}$$

where $e^{i\tilde{k}_{n-1}2(z-z_{n-1})}$ is due to the component of the primary's path which is not shared by the direct wave. If this distance is small ($\tilde{k}_{n-1}2(z_n-z) << 1$) then ($e^{i\tilde{k}_{n-1}2(z_n-z)}$) ≈ 1 and

$$PC_{an} \to R_n(\omega). \tag{2.32}$$

Equation (2.31) does not take into account geometrical spreading, however, if $z_n - z$ is small, the primary and direct arrivals travel nearly identical paths, and the effect of geometric spreading is equivalent.

2.5.3 Synthetic examples of AVF inversion of estimated VSP reflection coefficients

Here we illustrate this method of obtaining the reflection coefficient with synthetic examples of a 1D zero-offset VSP experiment in the anelastic case. We generate zero-offset VSP traces for the model shown in the right hand panel of Figure 2.7, with the Earth parameters listed in Table (2.1). Except for the first layer, all layers are anelastic including layer 4, which is where the receiver is located. The interface below the receiver is associated with a large contrast in Q. We allow the depth of the receiver to vary (Table (2.2)). We generate spectra of the direct and primary events, using equations (2.27) and (2.27), for each of these receiver geometries. As shown in Figure 2.9 to 2.11 we calculate the amplitude spectrum of the analytic reflection coefficient (blue) and we plot with the amplitude spectrum of the reflection coefficient calculated using Lira's method (red x's). As can be seen in Figure 2.9 to 2.11, we lose accuracy as the distance between the receiver and the target reflector grows. This is due to the $e^{i\tilde{k}_{n-1}2(z_n-z)}$ term in equation (2.31). When the receiver is 10 meters above the reflector we obtain a good estimate of the the reflection coefficient because $e^{i\tilde{k}_{n-1}2(z_n-z))} \approx 1$. As the distance distance between receiver and the reflector grows then $(e^{i\tilde{k}_{n-1}2(z_n-z)})$ is far from 1 and our corrected primary becomes a poor approximation to the reflection coefficient.

2.6 Remarks

In this chapter we review theory which is called upon throughout this thesis. We use the FST extensively as a means of estimating the local spectra of reflection events on both synthetic and field data. The review of anelastic reflection coefficients and AVF inversion

is important as it forms the theoretical foundation which this thesis is built on. Finally, Lira's method of estimating the reflection coefficient of a target on VSP data is called upon in Chapter 6 when AVF inversion is applied to a VSP data set from the Ross Lake heavy oil field in south-west Saskatchewan.

Table 2.1: Anelastic Earth model parameters.

Layer	Depth (m)	c (m/s)	Q
0	0-100	1500	∞
1	100-400	1800	250
2	400-650	1950	60
3	650-950	2100	100
4	950-1200	2200	100
5	1200-∞	2500	10

Table 2.2: Depth of receiver

Depth of receiver (m)	Distance above reflector (m)
1190	10
1170	30
1150	50

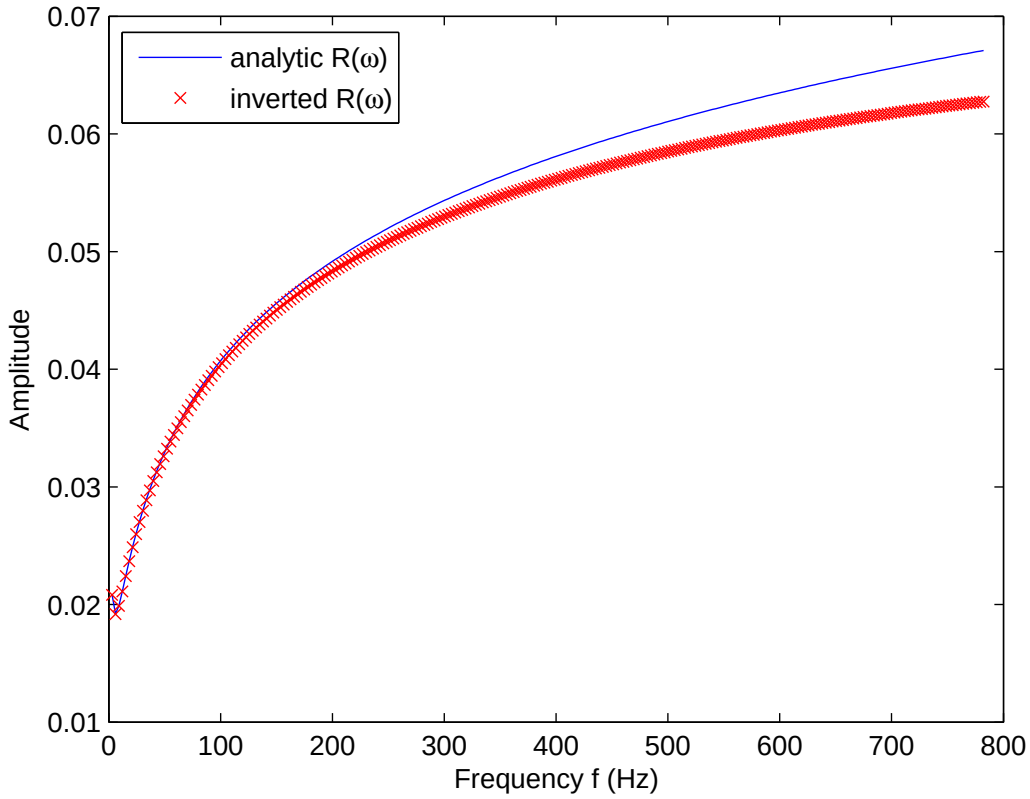

Figure 2.9: Analytic reflection coefficient (blue) and estimated reflection coefficient (red x's) for receiver 10 meters above reflector.

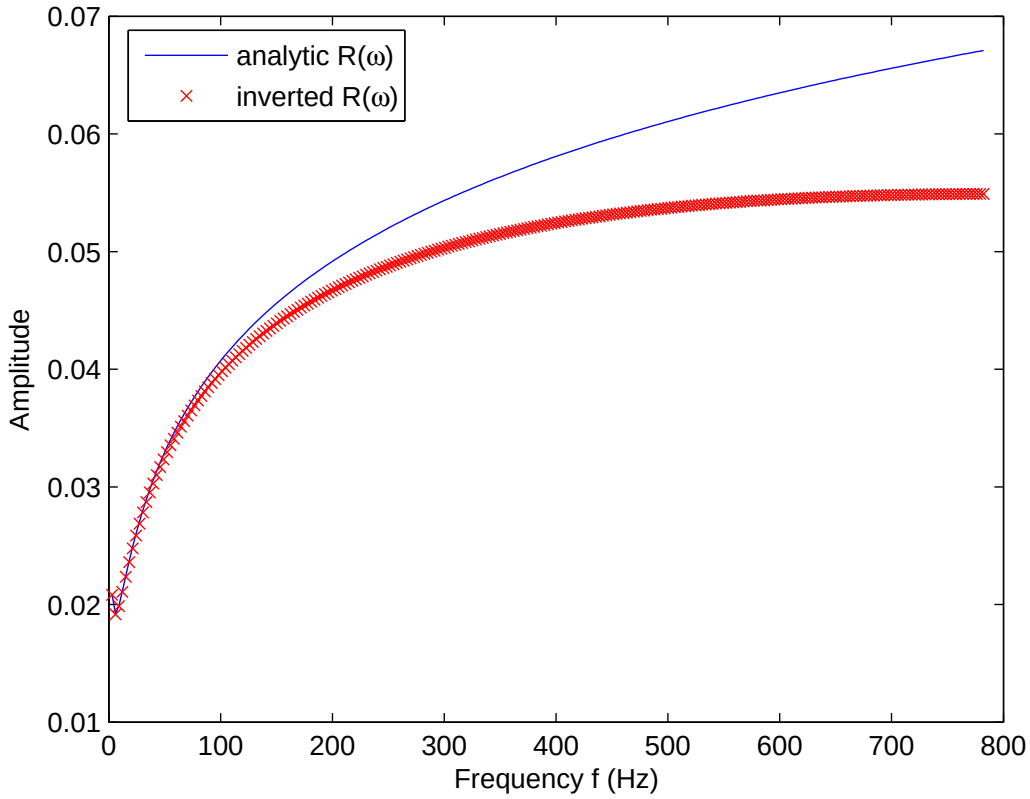

Figure 2.10: Analytic reflection coefficient (blue) and estimated reflection coefficient (red x's) for receiver 30 meters above reflector.

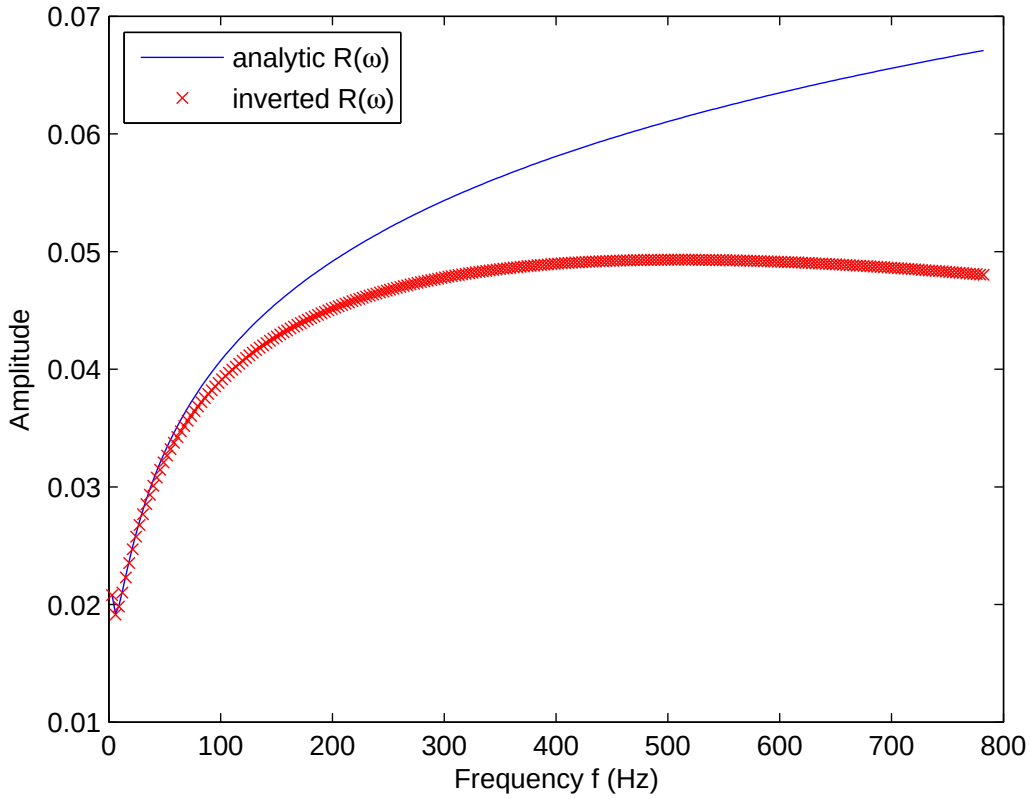

Figure 2.11: Analytic reflection coefficient (blue) and estimated reflection coefficient (red x's) for receiver 50 meters above reflector.

Chapter 3

Calibration of a fast S-transform

3.1 Introduction

Time-frequency decomposition methods provide a means of estimating the local spectra of recorded seismic events (for example, see Du et al., 2010). There are a range of time-frequency decomposition methods with applicability to seismic signal analysis (for example, see Margrave, 1997; Margrave et al., 2003). The S-transform is one such method which utilizes a Gaussian window and provides progressive resolution (Stockwell et al., 1996). The fast general Fourier family transform (FGFT) proposed by Brown et al. (2010) and implemented by Naghizadeh and Innanen (2010) provides a fast, non-redundant method of calculating the S-transform, henceforth referred to as the fast S-transform (FST). There are many applications of time-frequency decomposition methods in seismic data analysis. They have been used to facilitate non stationary processing (Margrave, 1997; Margrave et al., 2003) and analyzing absorption (Miao et al., 2007; Reine et al., 2009). More recently, the FST has been implemented in multiple dimensions and is used as a tool for seismic interpolation (Naghizadeh and Innanen, 2010). In forthcoming chapters we will require high fidelity estimates of local reflection amplitudes as functions of frequency from seismic traces. It is our goal then, to test the ability of the FST in providing high fidelity estimates of the local spectra of seismic reflections. Where it fails to do so, we calibrate the amplitudes by normalizing the unit impulse response of the FST algorithm.

3.2 S-transform review

3.2.1 S-transform theory

The S-transform of a time signal $g(t)$ is defined by Stockwell et al. (1996) and presented by Brown et al. (2010) as

$$S(\tau, f) = \int_{-\infty}^{\infty} g(t) \frac{|f|}{\sqrt{2\pi}} e^{\frac{-(\tau-t)^2 f^2}{2}} e^{-i2\pi f t} dt, \tag{3.1}$$

where τ and f are the time co-ordinate and frequency co-ordinate of the S-domain respectively and $\frac{|f|}{\sqrt{2\pi}} e^{\frac{-(\tau-t)^2 f^2}{2}}$ is the Gaussian window. Equation (3.1) demonstrates how the S-transform is calculated directly from the time domain input. It is also possible to calculate the S-transform from frequency domain input. By taking the Fourier transform along the τ axis of the S-domain we generate what Brown et al. (2010) refer to as the α-domain:

$$\alpha(f', f) = \int_{-\infty}^{\infty} S(\tau, f) e^{-i2\pi f' \tau} d\tau, \tag{3.2}$$

where f' is a frequency-shift axis generated by taking the Fourier transform along the τ axis of the S-domain. The α-domain may also be expressed as (Brown et al., 2010)

$$\alpha(f', f) = G(f' + f) W(f', f). \tag{3.3}$$

Here G(f' + f) is a matrix where each row is the Fourier transform of the signal G(f) shifted by a frequency increment f'. The α-domain is generated by multiplying this matrix by the Fourier transform of the window function W(f',f). Once the α-domain is constructed, the S-domain is obtained by performing an inverse Fourier transform along the f'-axis of the α-domain. The equation for transforming to the S-domain from the α-domain is given in Brown et al. (2010) as

$$S(\tau, f) = \int_{-\infty}^{\infty} \alpha(f', f) \cdot e^{-i2\pi f' \tau} df'. \tag{3.4}$$

3.2.2 Fast S-transform algorithm

As presented in Brown et al. (2010) and implemented by Naghizadeh and Innanen (2010) the ST can be calculated non-redundantly by segmenting in the α-domain, with higher frequencies being coarsely sampled and lower frequencies being finely sampled. The α-domain is divided into segments, with large segments for high frequencies and small segments for low frequencies (Brown et al., 2010). Only one frequency is sampled at the centre of each segment and these values are used for all frequencies enclosed by the segment (Brown et al., 2010). To generate the S-transform an inverse fast Fourier transform (IFFT) is applied to each segment. The IFFT of each segment populates its corresponding frequency range in the S-domain for the entire τ axis.

3.3 Amplitude calibration of the FST algorithm

3.3.1 Errors in uncalibrated FST

In Figure 3.1(a) a unit impulse is illustrated and its corresponding S-domain generated by the FST (Figure 3.1(b)). In Figure 3.1(c) the amplitude spectrum of the unit impulse is obtained by extracting the S-domain amplitudes at the time sample of the unit impulse. Figure 3.1(c) is a plot of the unit impulse response (hereafter UIR) of the FST. The amplitude spectrum of a unit impulse is a constant value at unity for all frequencies. By looking at Figure 3.1(c) it can be seen that the derived spectrum of the unit impulse from the S-domain is not a constant value but rather increases with a stair-case trend. The goal of this chapter is to calibrate the FST by removing the algorithm footprint, as observed in Figure 3.1. We do this by correcting its unit impulse response to be a constant value at unity.

In order to characterize the footprint of the FST algorithm, a series of tests are performed. For the first test, unit impulses at the centre of empty vectors of varying

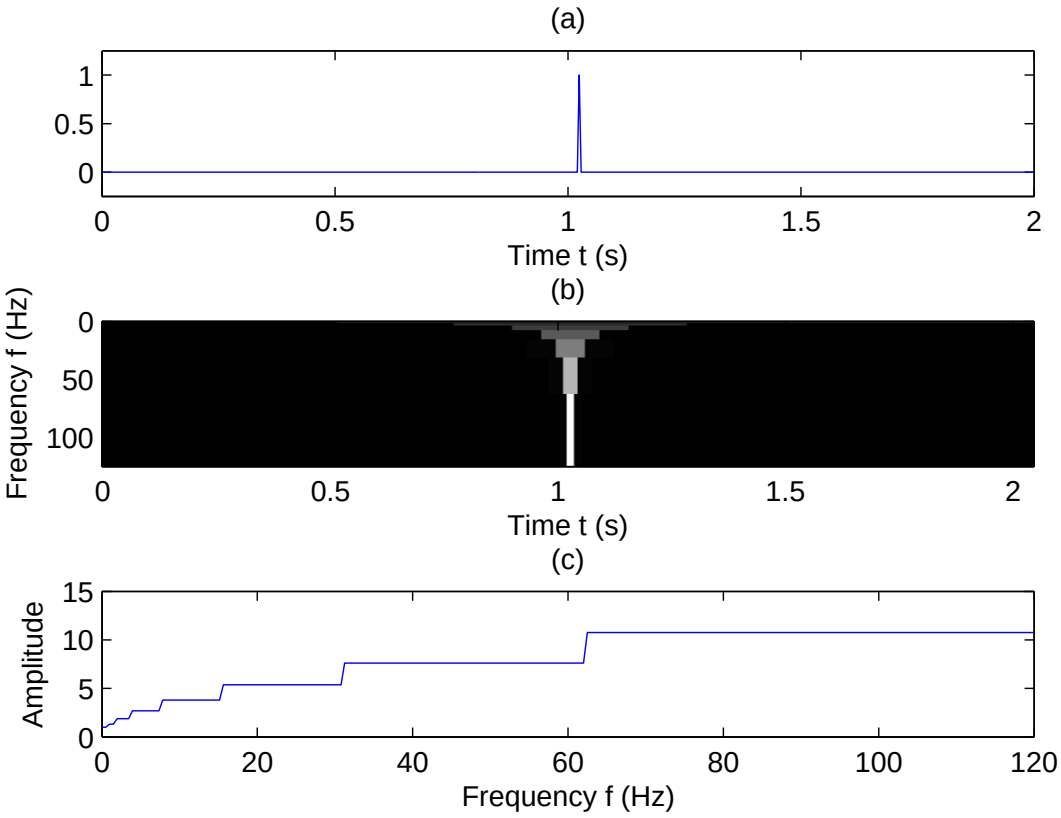

Figure 3.1: UIR of FST before any corrections. (a) A Unit impulse. (b) The S-domain of the unit impulse. (c) The amplitude spectrum of the unit impulse extracted from its S-domain.

lengths are input into the FST algorithm and the UIR is observed for all of these vectors. For example, in Figure 3.1 the unit impulse is at the centre of a 512 point vector. A stair-case pattern of increasing amplitude with frequency, as shown in Figure 3.1(c), is observed for all vector sizes. Upon further investigation, we discover that in the original FST algorithm there is a scaling factor of $1/\sqrt{N}$ applied with the IFFT of the individual segments in the α-domain, where N is the number of samples in the segment. We have corrected to the proper scaling of $1/N$. After implementing this correction the same tests described above are performed again to observe the UIR. Consider Figure 3.2, the

UIR of the FST after this correction is illustrated. In Figure 3.2(a) the unit impulse input into the FST is shown, in Figure 3.2(b) we see the S-domain of the unit impulse. In Figure 3.2(c) we see the amplitudes of the UIR extracted from the S-domain. It is clear from Figure 3.2 that the stair-case increase of amplitude with frequency has been eliminated and the spectrum is closer to the desired result. However, the amplitude of the UIR drops to 0.95 at roughly 5 Hz and then stays relatively constant. This is close to the desired UIR but there is still some residual algorithm footprint which needs to be addressed.

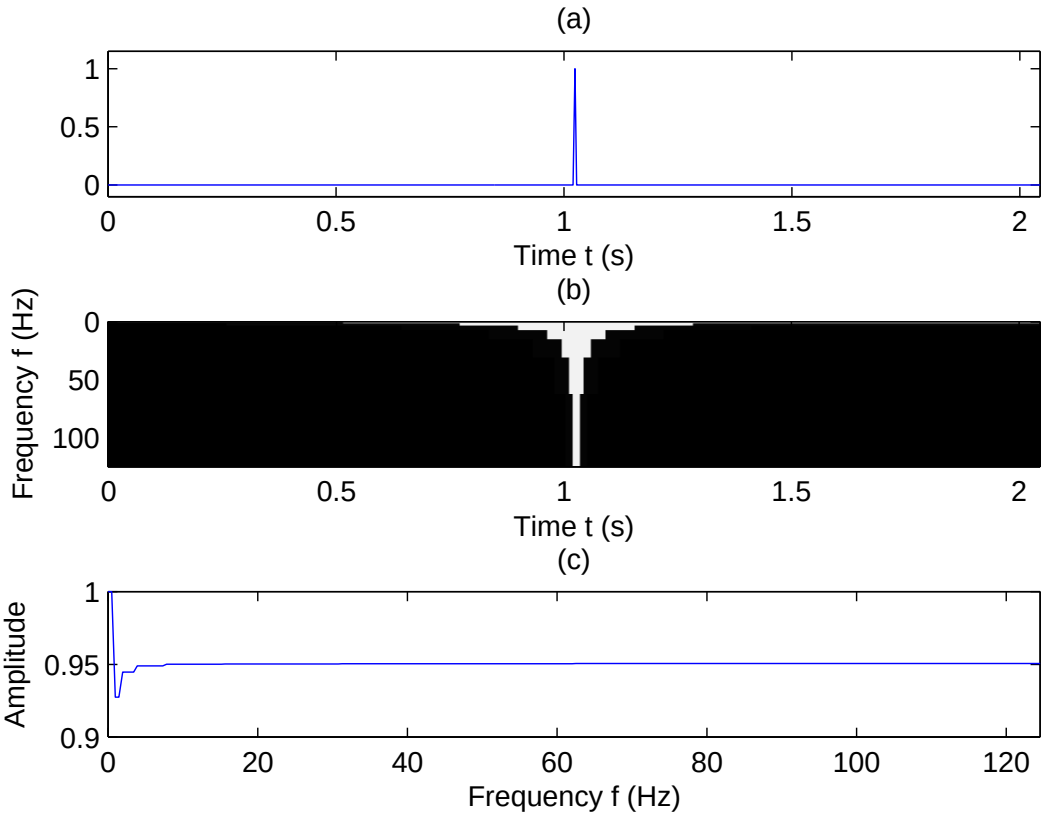

Figure 3.2: UIR after 1/N scaling correction. (a) A unit impulse. (b) Is its S-domain with errors corrected (c) The amplitude spectrum of the unit impulse extracted from its S-domain.

3.3.2 Calibration

Another test we perform is to vary the position of a unit impulse within an empty vector and observe the resulting S-domain of the unit impulse. A number of these unit impulses are input into the FST and the S-domain is examined to determine if the UIR is dependent on the impulse position in time. Consider Figure 3.3. Two separate unit impulses located at roughly 0.2 s and 1.4 s within a 2.044 s time signal, their S-domain signatures, and profiles through the S-domain at their respective arrival times are shown. The distinctly different S-domain profiles of these two unit impulses shows that there is a dependence of the UIR on the location of the unit impulse in time.

In order to correct the UIR for the dependence on position of the impulse, and any other residual footprint, a code is developed which calculates and implements the corrections needed to make the spectrum of a unit impulse a constant at unity for any location in time. The corrections are stored in a matrix which is subsequently multiplied with the S-domain. This matrix will hereafter be referred to as the FST spectrum fidelity correction matrix (SFCM). For every N-point signal there is a corresponding NxN point S-domain and an NxN point SFCM. The SFCM is found by first determining the UIR of the FST at every time sample. Then for each of these UIR's a set of N scaling coefficients is produced by determining the multipliers needed to scale the UIR to a constant value at unity. This is carried out by dividing 1 by the amplitude of the UIR at all frequencies. Hence, the j^{th} row of the SFCM contains the scaling coefficients which needs to be multiplied with the S-domain spectrum at the j^{th} time sample. The SFCM corrects the dependence of the UIR on position in time and it also takes care of all other residual algorithm footprint. With this correction matrix applied to the S-domain, a unit impulse input into the FST algorithm at any location will yield the desired constant value. In Figure 3.4 we see the S-domain for a unit impulse with the SFCM applied and its profile in the S-domain. We find the desired UIR.

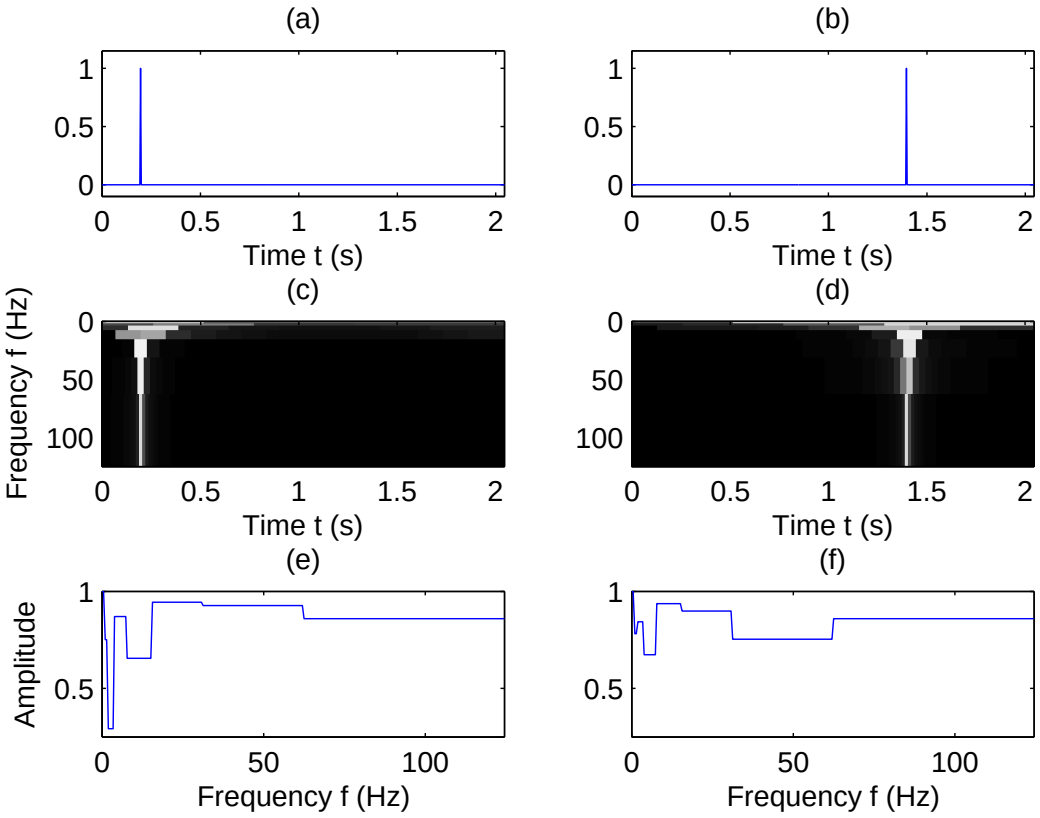

Figure 3.3: Dependence of the position of the unit impulse on the UIR of the FST algorithm. (a) and (b) Two unit impulses at roughly 0.3 s and 1.4 respectively. (c) and (d) S-domains of the unit impulses. (e) and (f) Amplitudes of the unit impulses extracted from their S-domains.

3.3.3 An alternate approach

As an alternative to applying the NxN point SFCM to the S-domain, we have developed a code which allows for the FST amplitude calibration to be carried out only on specific sets of time samples. This code is computationally more efficient by applying the calibration only to time samples of interest. If, for instance, we only desire to calibrate the FST amplitudes of a specific reflection event in a seismic trace, we need only calibrate the amplitudes for the time sample where the reflection is located.

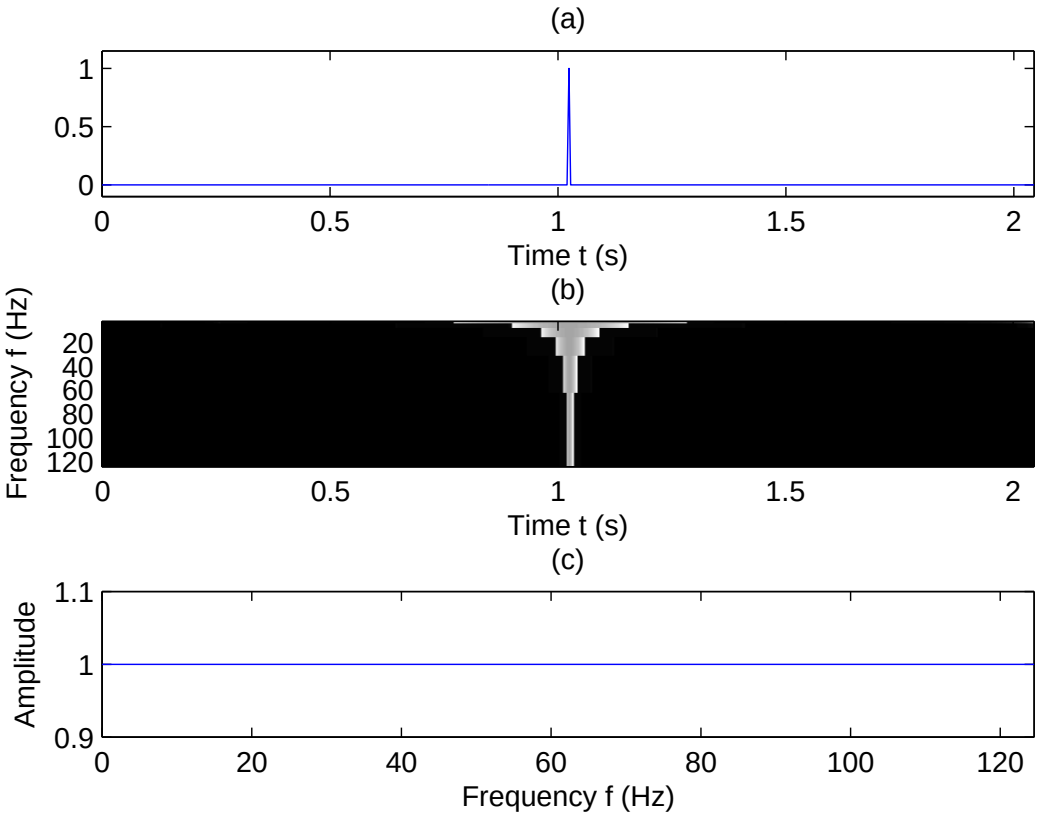

Figure 3.4: Unit Impulse Response of FST after calibration. (a) A unit impulse. (b) The calibrated S-domain of the unit impulse. (c) The amplitude spectrum of the unit impulse extracted from its S-domain.

3.4 Limits of the calibration

The spectrum generated by the FST algorithm has low time resolution at low frequencies. Therefore, even with the SFCM applied, the individual spectra of adjacent events will interfere with each other at low frequencies even when the events are separated in time by a wide margin. Also, the range of frequencies at which the spectra of individual events interfere with each other is greater the closer events are to each other. Because of this, it is important to develop a set of standards which define the fidelity of the spectrum of an event as a function of its proximity to other events. Two unit impulses are input into the FST at opposite ends of an otherwise empty time series. The S-domain is examined to determine the lowest frequency at which the spectra of the individual impulses do not interfere with each other in excess of 8 percent (henceforth called the cut-off frequency). Then each unit impulse is moved one sample closer in time and again the S-domain is examined for the cut-off frequency. This procedure continues until the separation of the impulses approaches zero. Consider Figures 3.5 through to 3.8, in which the S-domain of two unit impulses and their S-domain profiles for time separations of 240, 180, 90 and 20 samples are shown. In Figure 3.5(a) is displayed the S-domain of two unit impulses which are set 240 samples apart, as can be seen from their profiles (Figure 3.5(b) and 3.5(c)) the individual spectra of these two events only interfere with each other at very low frequencies. However, as the separation between impulses decreases (Figure 3.7, 3.8, and 3.9) it can be seen that individual spectra interfere with each other at progressively higher frequencies. To quantify the cutoff frequency, a program is written which determines the lowest frequency at which the amplitude of the unit impulses spectra falls within 8 percent of unity. The cutoff frequency is then plotted against the number of samples separating the unit impulses. This is shown by the blue line in Figure 3.9. As expected, the closer the impulses are to each other the higher the cutoff frequency. The green line in Figure

3.9 is the best-fit exponential decay curve in the least squares sense. Because there is so much variance to the cut-off frequency curve (Figure 3.9), we anticipate that we may come across examples where even a large separation between events renders large regions of the local spectra to be useless. Also a qualitative study of the cutoff frequency as a function of impulse separation is performed and is shown in Figure 3.10. This qualitative plot is obtained by "eyeballing" the general trend exhibited in Figure 3.9. Figure 3.9 and 3.9 provide a guideline for determining the portion of an events spectrum which is high fidelity.

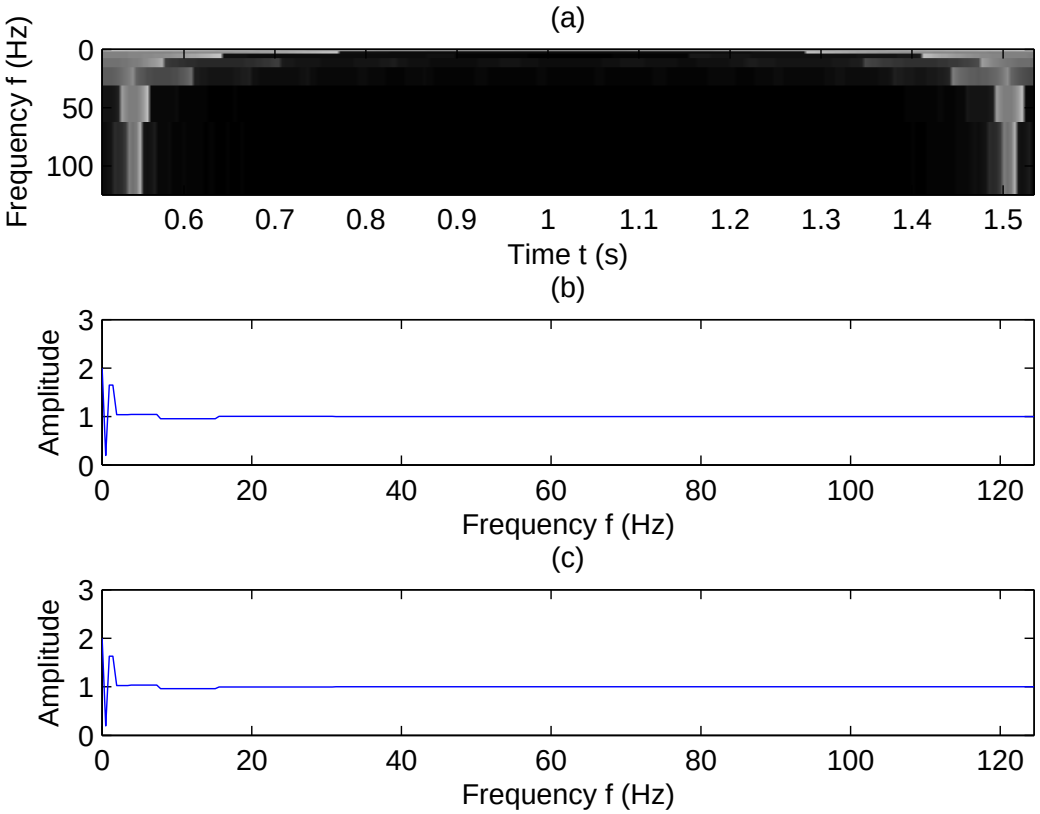

Figure 3.5: (a) S-domain of two unit impulses 240 samples apart. (b) and (c) Their respective amplitude spectra extracted from the S-domain.

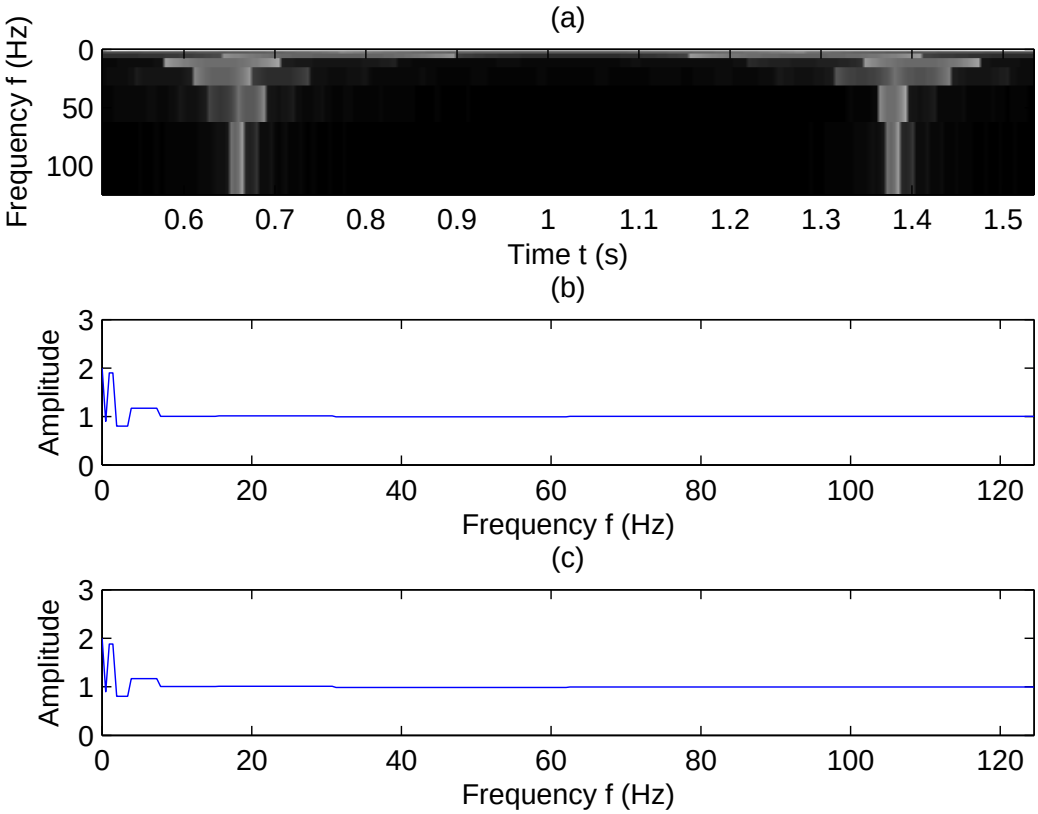

Figure 3.6: a) S-domain of two unit impulses 180 samples apart. (b) and (c) Their respective amplitude spectra extracted from the S-domain.

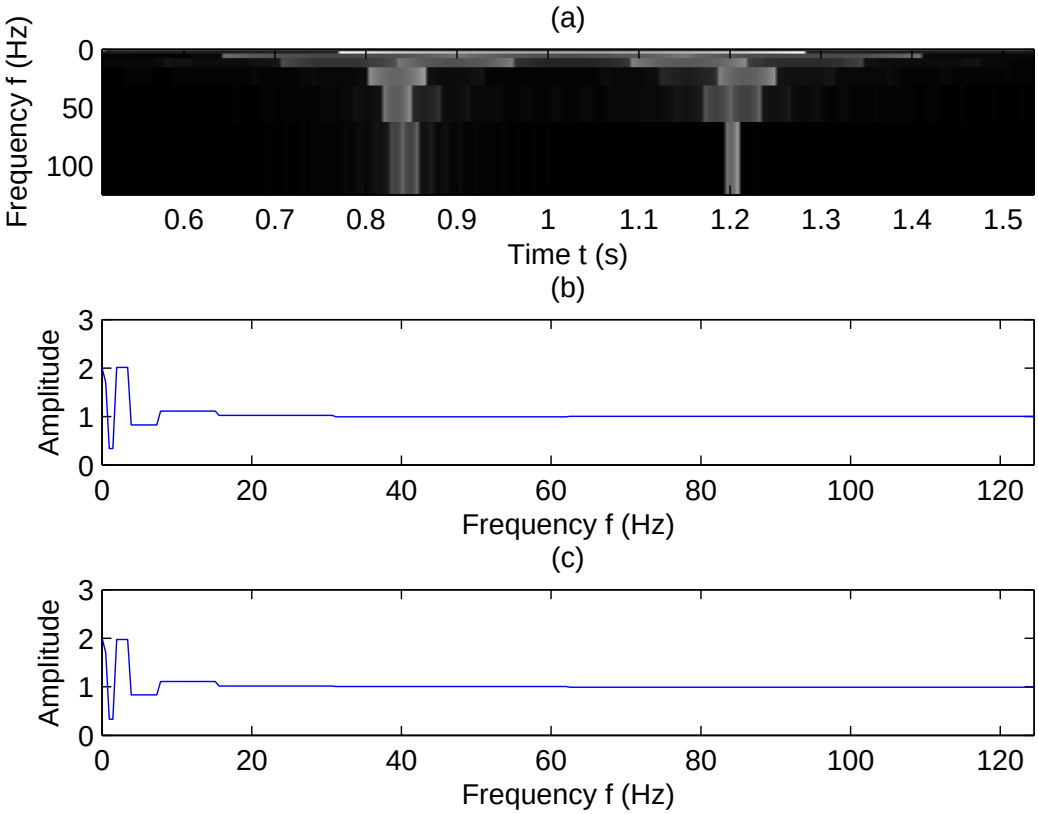

Figure 3.7: a) S-domain of two unit impulses 90 samples apart. (b) and (c) Their respective amplitude spectra extracted from the S-domain.

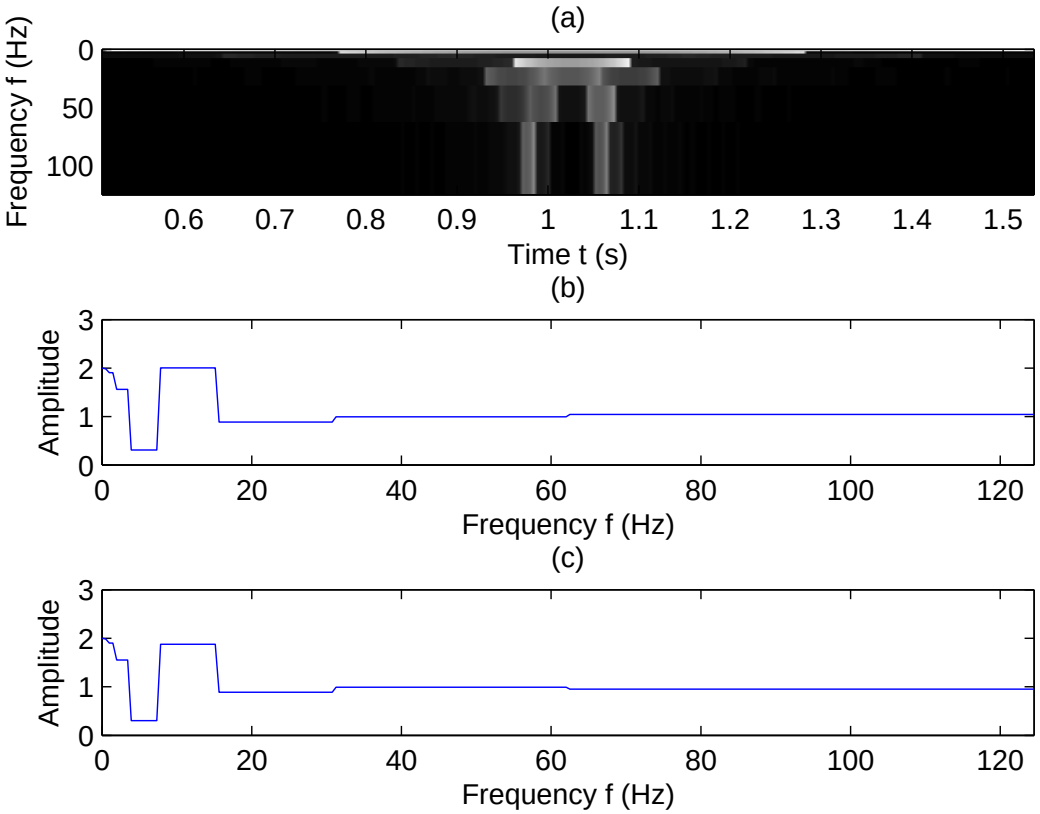

Figure 3.8: a) S-domain of two unit impulses 20 samples apart. (b) and (c) Their respective amplitude spectra extracted from the S-domain.

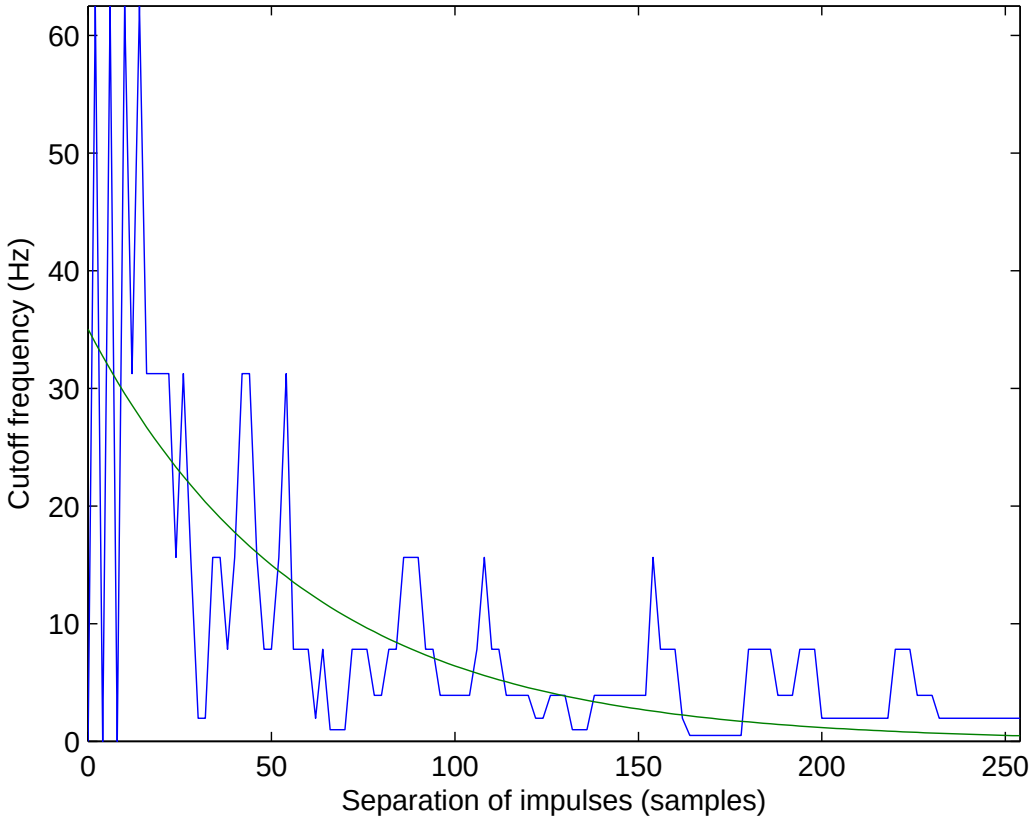

Figure 3.9: Cutoff frequency vs. impulse separation, quantitative approach. The green curve is the best-fit exponential decay curve in the least-squares sense.

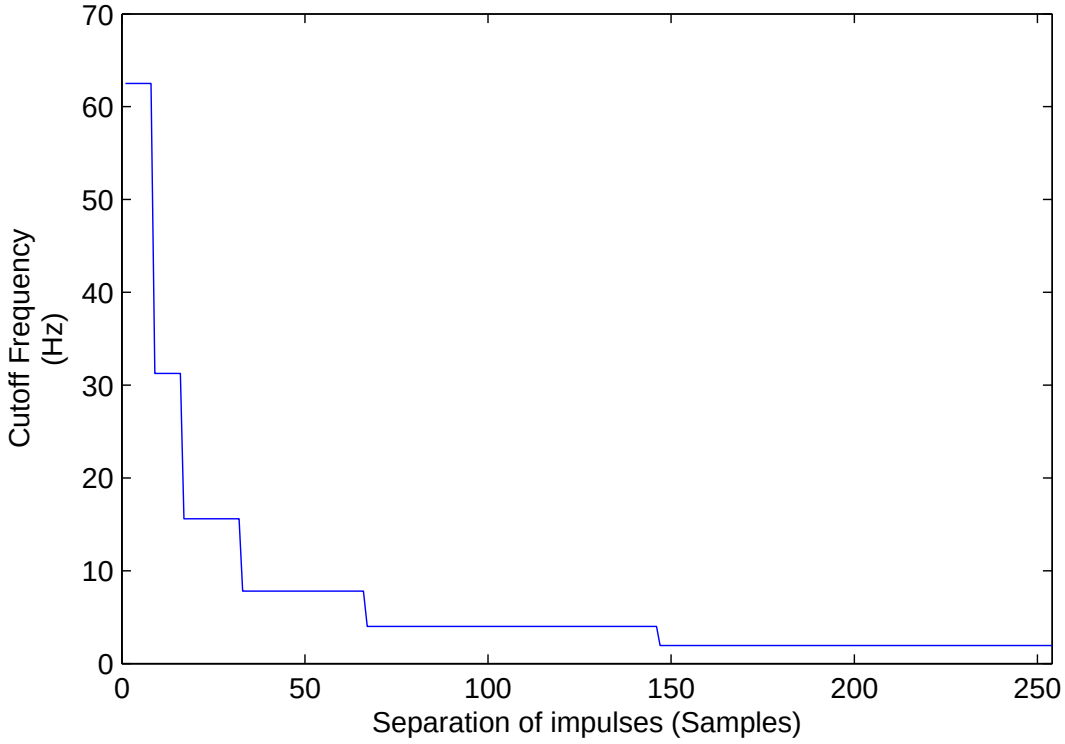

Figure 3.10: Cutoff frequency vs. impulse separation, qualitative approach

3.5 Conclusions

The FST, proposed by Brown et al. (2010) and implemented by Naghizadeh and Innanen (2010) provides a fast, non-redundant method of time-frequency decomposition with a wide range of applicability to seismic signal analysis. In this chapter, the amplitude spectrum of the FST algorithm is calibrated by normalizing the unit impulse response. This calibration is carried out by calculating and implementing the spectrum fidelity calibration matrix which is multiplied directly with the S-domain. Also, limits on the usefulness of the amplitude calibration, due to the low time resolution at low frequencies nature of the algorithm, are discussed and a set of guidelines for determining the validity of the spectra of individual events as a function of proximity to other events is established. As there is a large variance to the calculated cutoff frequency curve, we anticipate problems adhering to these guidelines. In the coming chapters we will use this calibrated tool to analyze the frequency dependence of individual events in a densely populated trace.

Chapter 4

Anelastic reflection coefficients and their estimation

4.1 Introduction

It has been observed that strong absorptive reflection coefficients, caused by reservoirs with very low Q, cause frequency dependent seismic anomalies (for example, see Odebeatu et al., 2006). Our goal is to develop quantitative methods by which the information in such anomalies may be extracted. In this chapter we review briefly the theory covered in Chapter 2 of anelastic reflection coefficients and linear amplitude-variations-with-frequency (AVF) inversion. We then develop the theory for anelastic AVF inversion for the blocky spectra generated in realistic data by the fast S-transform (FST). We test the AVF inversion of blocky spectra on synthetic data and evaluate inversion accuracy.

4.2 Character of an anelastic reflection coefficient

If a plane wave is incident upon a planar boundary whose normal is the vertical (z) axis, and separating two homogenous layers then the reflection coefficient will be given by

$$R = \frac{k_{z_0} - k_{z_1}}{k_{z_0} + k_{z_1}}, \tag{4.1}$$

where R is the reflection coefficient, k_{z_0} is the vertical wavenumber for the layer above the interface and k_{z_1} is the vertical wavenumber for the layer below the interface. In order to model anelastic reflection coefficients, we use an expression for wavenumber which includes a model for nearly constant Q described by Aki and Richards (2002) as

$$k = \frac{\omega}{c}\left(1 + \frac{i}{2Q} - \frac{\log(\omega/\omega_r)}{\pi Q}\right). \tag{4.2}$$

Here c is the seismic velocity, Q is quality factor, ω is the frequency component, and ω_r is a reference frequency. For waves at normal incidence the expression for wavenumber (k) given in (4.2) is equivalent to vertical wavenumber (k_z) and can be implemented in equation (4.1). Hence, the equation which models anelastic reflection coefficients in one dimension, by inserting equation (4.2) into equation (4.1) is given by

$$R(\omega) = \frac{\left[\frac{1}{c_0}(1 + \frac{i}{2Q_0} - \frac{\log(\omega/\omega_r)}{\pi Q_0}) - \frac{1}{c_1}(1 + \frac{i}{2Q_1} - \frac{\log(\omega/\omega_r)}{\pi Q_1})\right]}{\left[\frac{1}{c_0}(1 + \frac{i}{2Q_0} - \frac{\log(\omega/\omega_r)}{\pi Q_0}) + \frac{1}{c_1}(1 + \frac{i}{2Q_1} - \frac{\log(\omega/\omega_r)}{\pi Q_1})\right]}, \tag{4.3}$$

where the reflection coefficient, $R(\omega)$, is now complex and a function of frequency. Equation (4.3) is the general form for the normal incidence reflection coefficient in anelastic media. Consider the situation where an elastic overburden ($Q \to \infty$) is overlaying a highly anelastic target (Q finite). Equation (4.3) becomes

$$R(\omega) = \frac{\left[\frac{1}{c_0} - \frac{1}{c_1}(1 + \frac{i}{2Q_1} - \frac{\log(\omega/\omega_r)}{\pi Q_1})\right]}{\left[\frac{1}{c_0} + \frac{1}{c_1}(1 + \frac{i}{2Q_1} - \frac{\log(\omega/\omega_r)}{\pi Q_1})\right]}, \tag{4.4}$$

now if we make the following substitutions (from Innanen, 2011) $F(\omega) = \frac{i}{2} - \frac{1}{\pi}\log(\omega/\omega_r)$, $a_C = 1 - \frac{c_0^2}{c_1^2}$ and $a_Q = \frac{1}{Q_1}$. We can expand equation (4.4), and linearize (assuming small a_Q and a_C) to obtain the following expression

$$R(\omega) \approx -\frac{1}{2}a_Q F(\omega) + \frac{1}{4}a_C, \tag{4.5}$$

where a_Q and a_C are the perturbation parameters in Q and acoustic seismic velocity respectively. It is also worth noting that $F(\omega)$ is a known function. Equation (4.5) defines the forward problem of calculating $R(\omega)$ given a_C and a_Q.

4.3 Review of the theory of linear anelastic AVF inversion

Recall from our review of linear AVF inverse theory (Chapter 2) that our goal is to invert equation (4.5) to estimate a_Q or a_C from measurements of $R(\omega)$. Equation (4.5) contains

two unknowns, a_C and a_Q. If we can determine $R(\omega)$ for two different frequencies, ω_1 and ω_2 , then we can take the difference between $R(\omega_1)$ and $R(\omega_2)$ and obtain an expression for a_Q given by Innanen (2011):

$$a_Q \approx -2\left(\frac{R(\omega_2) - R(\omega_1)}{F(\omega_2) - F(\omega_1)}\right). \tag{4.6}$$

We point out that the method we use to invert for Q is independent of the method which we use to model the seismic data.

We take a moment here to remind the reader that, although the theoretical derivation for a_Q in equation (4.6) calls for the real part of $R(\omega)$, in practise we will use the amplitude spectrum of $R(\omega)$, $|R(\omega)|$. This is because it is the amplitude spectrum of the FST that we calibrate in Chapter 3 to obtain high fidelity estimates of the local spectra of reflection events. Further, in Chapter 6 when we study a vertical seismic profile (VSP) data set, we follow a method of estimating the reflection coefficient of a target which calls for amplitude spectra as input. In Chapter 2 we show that if the imaginary part of $R(\omega)$ is small then $|R(\omega)|$ is a good approximation to the real part of $R(\omega)$. Henceforth, when we write $R(\omega)$ we refer to the amplitude spectrum of the reflection coefficient.

4.4 A seismic trace containing an anelastic reflection

Consider Figure 4.1, in which a model of an elastic overburden overlaying a highly anelastic target is illustrated. Also illustrated in Figure 4.1 is the seismic trace which would be recorded over this model for a source at z_s and a receiver at z_g. In Figure 4.2 we see the amplitude spectrum of the anelastic (or absorptive) reflection coefficient associated with this model (red). In blue we see the elastic, frequency independent, reflection coefficient due solely to an equivalent contrast in wavespeed. It is this dispersive character of the anelastic reflection coefficient which we wish to use to estimate target parameters.

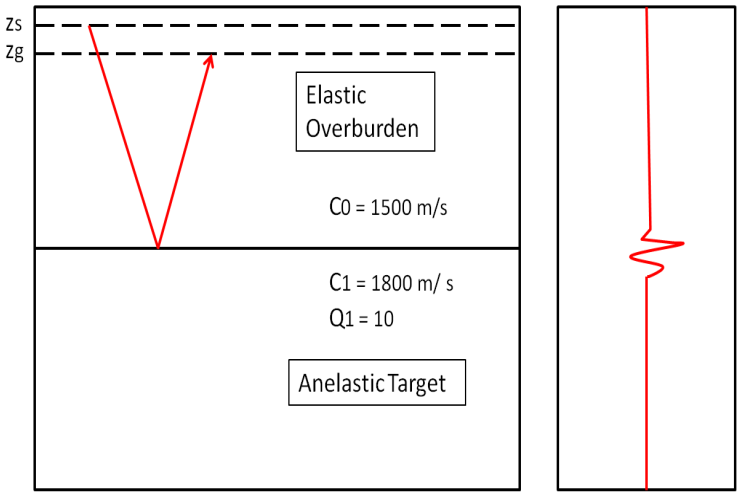

Figure 4.1: A simplified Earth model of an elastic overburden overlaying a highly anelastic target. On the right: a synthetic seismic trace generated for a source at z_s and a receiver at z_g. The exact analytic expression for the reflection is used to generate the synthetic data.

4.5 Estimation of local spectra of anelastic reflection coefficients

In a real seismic data trace with numerous reflection events we will need a method of time-frequency decomposition to extract local spectra of target anelastic reflection events. We can obtain an estimate of a targets dispersive reflection coefficient using the calibrated FST. Consider again the simple Earth model consisting of an elastic overburden overlaying a highly anelastic target (Figure 4.1). In Figure 4.3 we see the analytic anelastic reflection coefficient (blue) for this model and the estimate of the anelastic reflection using the calibrated FST (black). Notice that the FST estimate of the reflection coefficient has a blocky appearance. We will need to modify linear AVF inverse theory to take input from the FST.

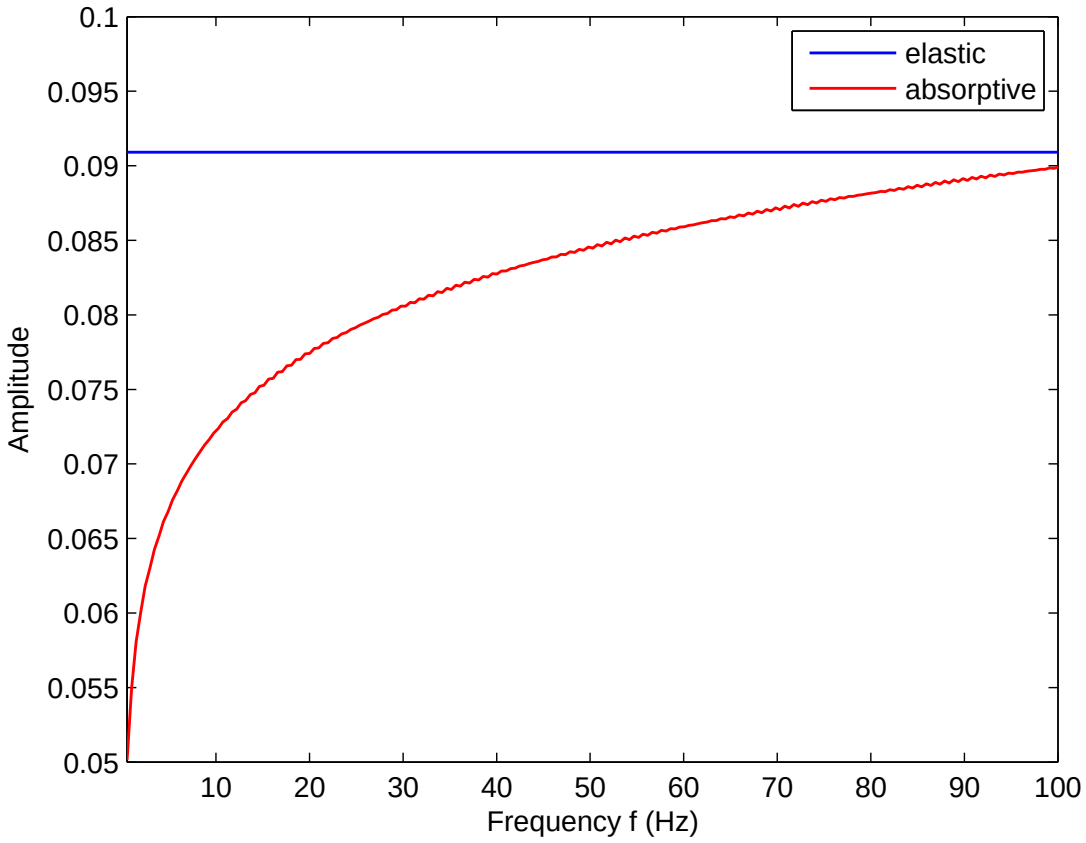

Figure 4.2: Dispersive reflection coefficient associated with the model in Figure 4.1 (red). The elastic reflection coefficient due to the contrast in wavespeed only (blue). $c_0 = 1500m/s$, $c_1 = 1800m/s$, and $Q_1 = 10$.

4.6 Theory for anelastic AVF inversion of blocky spectra

4.6.1 Overview

Equation (4.6) provides an expression to invert for a_Q provided we have an estimate of $R(\omega)$ for at least two different frequencies. The problem is how to estimate $R(\omega)$ from recorded seismic data. It is necessary that we are able to estimate local spectra of seismic events. We will use the calibrated fast S-transform algorithm (FST) which our testing indicates offers high fidelity estimates of local spectra (see Chapter 3).

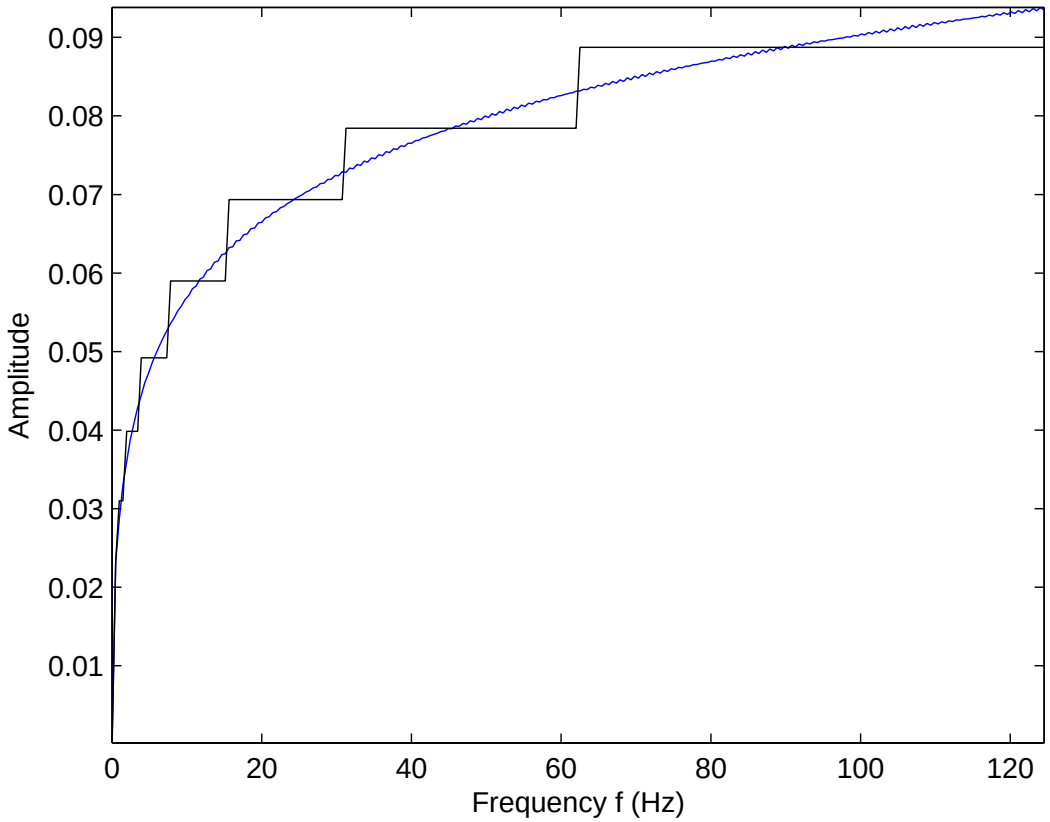

Figure 4.3: Analytic reflection coefficient associated with the model in Figure 4.1 (blue). The FST estimate of the reflection coefficient (black). The reflection is created using the following parameters, $c_0 = 1500m/s$, $c_1 = 1800m/s$, and $Q_1 = 10$.

In this chapter, we define $\tilde{R}(\omega)$ as the estimate of the spectrum of the reflection coefficient, $R(\omega)$, obtained from the calibrated FST. We use forward modeling codes to generate synthetic traces with a single anelastic reflection and then implement the FST to estimate the local spectrum of the anelastic reflection coefficient. Finally, we invert for a_Q using a slightly modified version of equation (4.6). For synthetic traces with a single reflection, the true spectrum of the reflection coefficient, $R(\omega)$, may be obtained by using a fast Fourier transform (FFT). For our synthetic traces with a single anelastic reflection, we compare the spectrum of the reflection coefficient as estimated by the FST

($\tilde{R}(\omega)$), with the true spectrum as calculated by an FFT.

4.6.2 Method

We start by generating a synthetic trace with a single anelastic reflection coefficient (as illustrated by Figure 4.1). Figure 4.4(a) is a plot of the synthetic trace, modeled using a plane wave incident upon a planar boundary separating an elastic overburden from a highly anelastic target. Figure 4.4(b) is a plot of the S-domain of the synthetic trace. The black curve in Figure 4.4(c) is the local spectrum of the reflection ($\tilde{R}(\omega)$) which is obtained by extracting the profile of the reflection through the S-domain. The blue curve in Figure 1(c) is a plot of the analytic spectrum, $R(\omega)$, calculated directly from equation (4.3). Note that $\tilde{R}(\omega)$ in Figure 4.4(c) is not a continuous spectrum; it has a blocky appearance due to the tiling associated with the FST algorithm (see Chapter 2). Notice that the spectrum estimated by the FST is a very good approximation to the average of the true spectrum across the frequency band of each "tile".

Consider the $\tilde{R}$ value in Figure 4.4(c) associated with the band from $f = 31Hz$ to $f = 62Hz$. It is an average of the true spectrum over that frequency range. We can relate the $\tilde{R}$ values to the $R(\omega)$ values by the equation

$$\tilde{R}_j = \frac{\sum_{i=j_s}^{j_e} R(\omega_i)}{(j_e - j_s + 1)}. \tag{4.7}$$

where $\tilde{R}_j$ is the value of the j_{th} S-domain frequency band which spans the continuous spectrum from sample j_s to j_e. We define F'_j as the sum of the known $F(\omega)$ function over the same frequency band

$$F'_j = \sum_{i=j_s}^{j_e} F(\omega_i). \tag{4.8}$$

Now consider $\tilde{R}_k$ which is the average of $R(\omega)$ over the k_{th} S-domain frequency band which spans the continuous spectrum from sample k_s to k_e. Likewise, F'_k is defined as the sum of the known $F(\omega)$ function over the same frequency band as $\tilde{R}_k$. Now, let

$M = (j_e - j_s + 1)$ and $N = (k_e - k_s + 1)$ and define Z such that $Z \times N = M$. Then we can rewrite equation (4.6) in terms of $\tilde{R}_j$, $\tilde{R}_k$, F'_j, and F'_k

$$a_Q = -2\left(\frac{M\tilde{R}_j - ZN\tilde{R}_k}{F'_j - ZF'_k}\right). \tag{4.9}$$

With equation (4.9), we may invert for a_Q using the FST to estimate the local spectrum of anelastic reflection coefficients.

4.7 Evaluation of inversion accuracy with synthetic data

We implement equation (4.9) to invert for Q by generating synthetic seismic traces with a single anelastic reflection. The traces are generated for a two-layer, single interface model in which an elastic overburden overlays a highly anelastic target (such as shown in Figure 4.1). We use the FST to estimate the spectrum of the reflection and then implement equation (4.9) to invert for Q. A number of traces are modeled in which target Q ranges from 200 to 1. The inversion is performed and compared with the actual value for accuracy. This is shown in Figure 4.5 through to 4.7, where the red line is the inverted Q value and the black line is the actual Q value used to model the reflection. From these figures, we observe that the inversion works best for Q values ranging from about 15 to 50 but works satisfactorily until Q drops below 8. This is highlighted in Table (4.1), which shows the difference between the inverted and actual Q values.

As can be seen from Figures 4.5 through 4.7 and Table (4.1) the inversion works satisfactorily until Q drops below 8 and then inversion accuracy degrades rapidly. The failure of the inversion at very low Q is not due to an inability of the FST to estimate the spectrum of the reflection. Rather it is partly because we made a small a_Q assumption in order to linearize equation (4.4). Also we chose a reference frequency, ω_r, which is the highest frequency used in the modeling and this makes linearization error more pronounced at low Q. Thus, when Q is very low, the assumption of a small a_Q is not

satisfied and the linearized expression for a_Q is no longer valid.

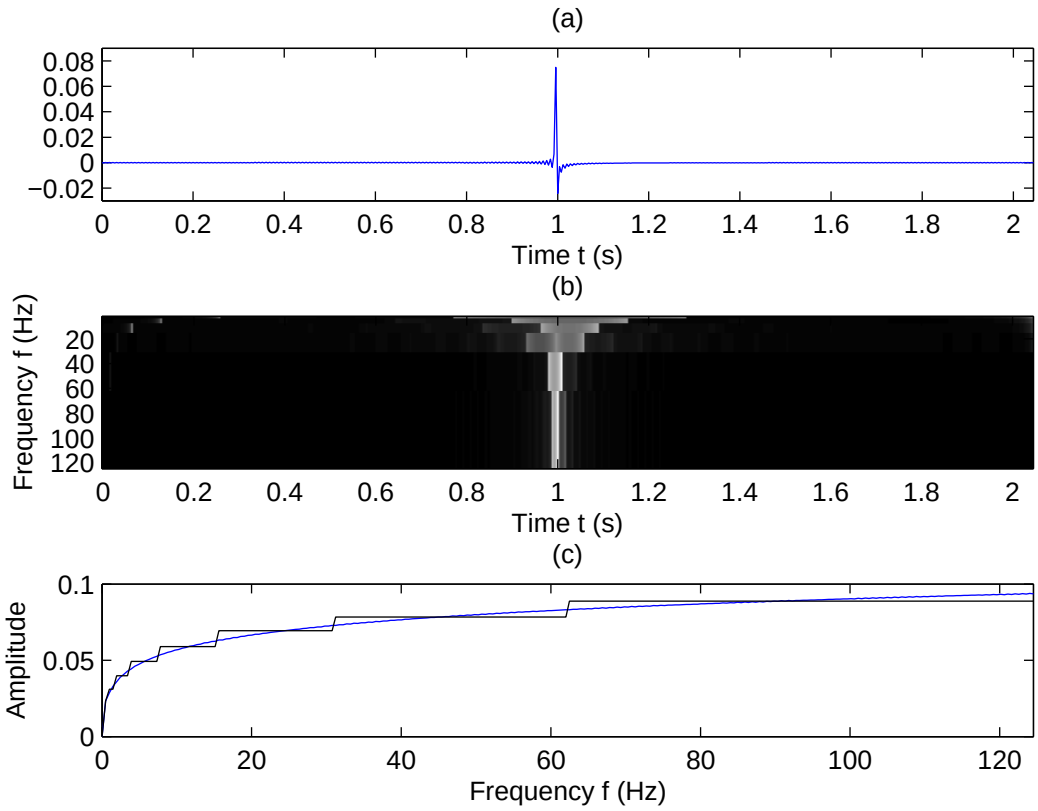

Figure 4.4: How to extract a frequency-dependent reflection coefficient from a seismic trace. In (a) The single primary reflection generated by a contrast from elastic to highly attenuative media is plotted in the time domain; in (b) The calibrated fast S-transform is carried out on the trace in (a), identifying the location of the event and estimating it's spectrum; in (c) The amplitudes picked from the S-transform (in black) is compared with the analytic reflection coefficient (in blue). The reflection is created using the following parameters, $c_0 = 1500m/s$, $c_1 = 1800m/s$, and $Q_1 = 10$.

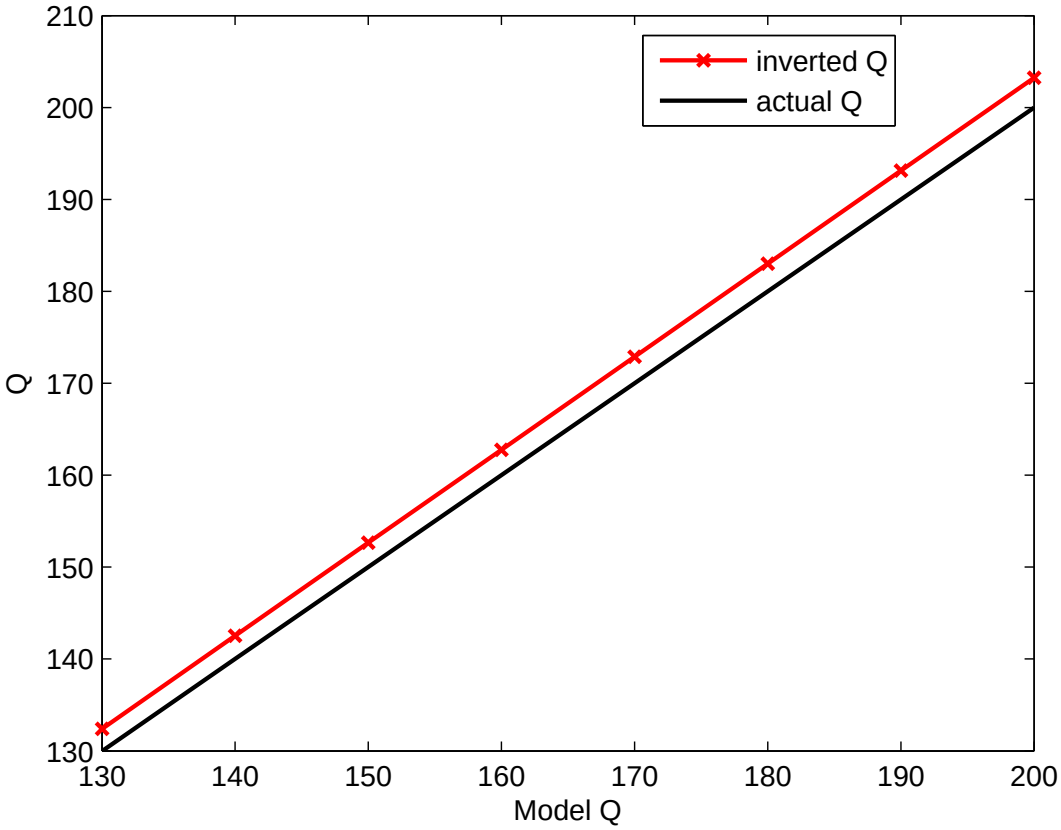

Figure 4.5: Determination of Q using linear AVF inversion. The value of Q used to model the single primary reflections is plotted in black and the value of Q determined by the linear AVF inversion is plotted in red.

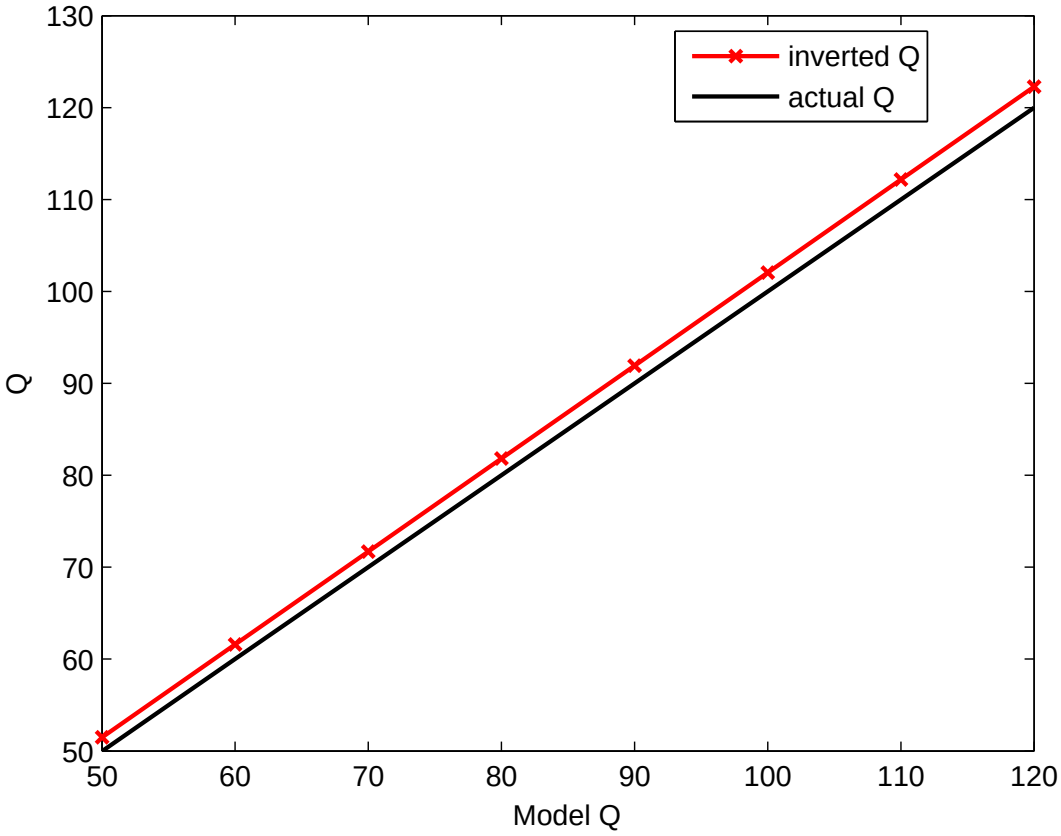

Figure 4.6: Determination of Q using linear AVF inversion. The value of Q used to model the single primary reflections is plotted in black and the value of Q determined by the linear AVF inversion is plotted in red.

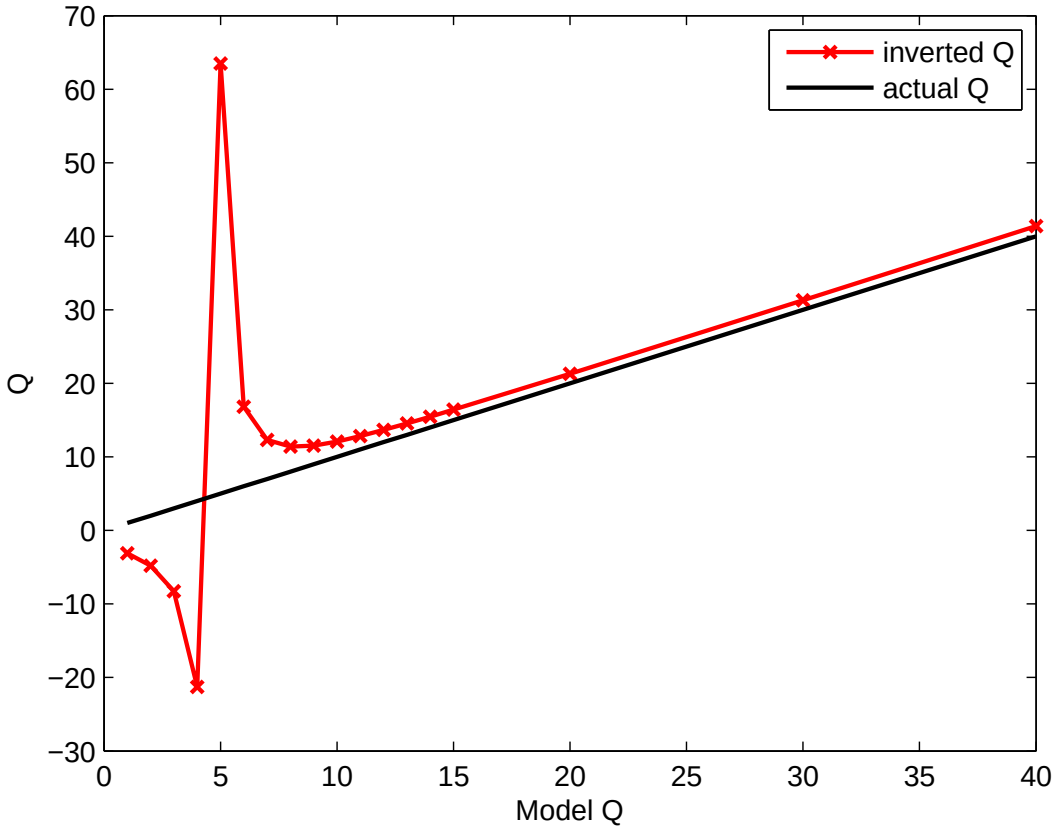

Figure 4.7: Determination of Q using linear AVF inversion. The value of Q used to model the single primary reflections is plotted in black and the value of Q determined by the linear AVF inversion is plotted in red.

Table 4.1: Comparison of inverted Q value to actual Q

Actual Q	Inverted Q	difference(absolute value)
50	51.4	1.48
40	41.3	1.38
30	31.3	1.30
20	21.2	1.29
15	16.4	1.41
14	15.4	1.47
13	14.5	1.54
12	13.6	1.65
11	12.8	1.82
10	12.0	2.09
9	11.5	2.54
8	11.4	3.4
7	12.3	5.3
6	16.8	10.82
5	63.4	58.47

4.8 Conclusions

We conclude that the calibrated FST is a promising time-frequency decomposition tool which may be used to extract AVF information. The FST is shown to produce a very good approximation to the average of the spectrum of the analytic reflection coefficients. Linear AVF inverse theory is modified to take input from the FST. We invert synthetic traces with a single anelastic for Q and find AVF inversion to be accurate except at very low $Q(Q < 8)$. At low Q the assumptions made in order to linearize equation (4.4) are no longer satisfied and inversion accuracy degrades rapidly.

In subsequent chapters we will extend this method of extracting AVF information to more complex traces with numerous reflection events. In Chapter 5 we discuss the ability of the FST to estimate the spectrum of local events as a function of proximity to other events. The more proximal events are to each other, the greater the frequency range that their individual spectra interfere with each other. Therefore, it is important

that we only use values of $\tilde{R}$ which fall outside this zone of interference when performing AVF inversion.

Chapter 5

Practical considerations in anelastic AVF inversion

5.1 Introduction

An amplitude-variations-with-frequency method (AVF) of inverting for Q developed by Innanen (2011) exists which requires as input an estimate of the local spectrum of the anelastic reflection coefficient. We have a calibrated fast S-transform (FST) which we have demonstrated provides a high fidelity estimate of the local spectra of seismic reflection events (Bird et al., 2010) and is suitable as input for AVF inversion. In this chapter we consider a prioritized set of issues a method like this will face when applied in the field. We develop methodologies and recommendations to manage:

1. Nearby/difficult-to-isolate events.

2. Random/uncorrelated noise.

3. Source wavelet.

We begin by describing our synthetic testing environment, including the forward modeling of attenuating traces, and then consider each of these ideas in turn. We determine AVF inversion, though more complicated, to be a likely tractable problem. Wu. et al. (2010) indicates that other research groups are making encouraging though not fully confirmed progress in this regard. Our conclusions in this chapter suggests that there are significant challenges for the quantitative characterization of an anelastic AVF signature in seismic field data. This indicates that refinements of signal analysis tools are required, and warns us that field identification of the data variations we are interested in will tend to be the exception rather than the rule with our current tool kit.

5.2 Synthetic data

We begin by modeling a synthetic seismogram which contains a single anelastic reflection. We start with an Earth model consisting of an elastic overburden overlaying a highly anelastic target (illustrated by the simple Earth model in Figure 4.1). We generate synthetic anelastic reflections for a plane wave normally incident on the target. The data are generated using exact analytic expressions. For example, consider the simple Earth model shown in Figure 4.1. Let the depth of the anelastic target be $z_1 = 300$ meters and the source and receiver be collocated at the surface, then the frequency domain of the seismic data is written as

$$D(\omega) = R(\omega) \exp(ik_0 z_1). \tag{5.1}$$

Here, $D(\omega)$ is the frequency domain of the data, $R(\omega)$ is the frequency domain of the anelastic reflection coefficient calculated using equation (2.6), and k_0 is the wavenumber in the incident medium. The time domain of the data is then obtained by performing an inverse fast Fourier transform on $D(\omega)$.

Once target anelastic reflection coefficients have been generated we further specialize the synthetic data to study the phenomena of interest. For instance, we study the effect of nearby/proximal events by adding our anelastic reflection coefficient to a synthetic trace with a large number of random reflections. To study the effect of a wavelet we convolve the anelastic reflection coefficient with a wavelet. To study random noise we add noise drawn from a Gaussian distribution to the traces.

5.3 Proximal reflections

In order to implement AVF inversion to estimate the Q contrast at a target, we need an estimate of the local spectrum of the target reflection coefficient. However, in realistic seismic data the low frequency spectrum of the reflection will be interfered with by nearby

seismic events. The closer two events are, the more their spectra will interfere. An event which is far away will only interfere with the target at very low frequencies, but closer events will interfere at higher frequencies. Unless the reflection to be analyzed is alone on the trace, some region of the local spectrum of the reflection will be influenced by its neighbors. This region will begin at the lowest frequencies, and move into the higher frequencies as other events approach the reflection of interest. In an event-dense trace, we will unavoidably be restricted to high-frequency regions of the local spectrum of a particular event. In Chapter 3 we developed quantitative guidelines for regions of the spectrum we deem high fidelity by restricting ourselves to an 8% tolerance level. In this section we attempt to confirm these guidelines by examining AVF inversion accuracy for target Q in event-dense traces, we take note where these guidelines fail.

We begin by generating an anelastic reflection coefficient as discussed in the previous section. Then, this single anelastic reflection is added to a synthetic trace with a large number of elastic reflections which precede the anelastic reflection in time, with the number of samples between the anelastic reflection and the nearest elastic reflection being a controlled variable. We define the number of samples between the target anelastic reflection and the nearest elastic reflection event as the separation distance. Figure 5.1(a) shows an example trace, the isolated reflection near 3.7 seconds is the anelastic reflection, it can clearly be seen that the separation distance is quite large for this trace. Each trace is input into the FST and the local spectrum of the anelastic reflection coefficient is obtained. The extracted spectrum of the anelastic reflection is then used to invert for Q of the target media using the modified AVF equation (Chapter 4). The low frequencies are rejected as useless. The numerical experiment is repeated with the separation distance reduced. In Figure 5.1(a) we see an example trace in which the separation distance is quite large. In Figure 5.1(b) we see the local spectrum of the anelastic reflection in blue extracted using the FST. The spectrum of the anelastic reflection alone is shown in red.

Figure 5.2 is similar to Figure 5.1 except that the separation distance has been reduced.

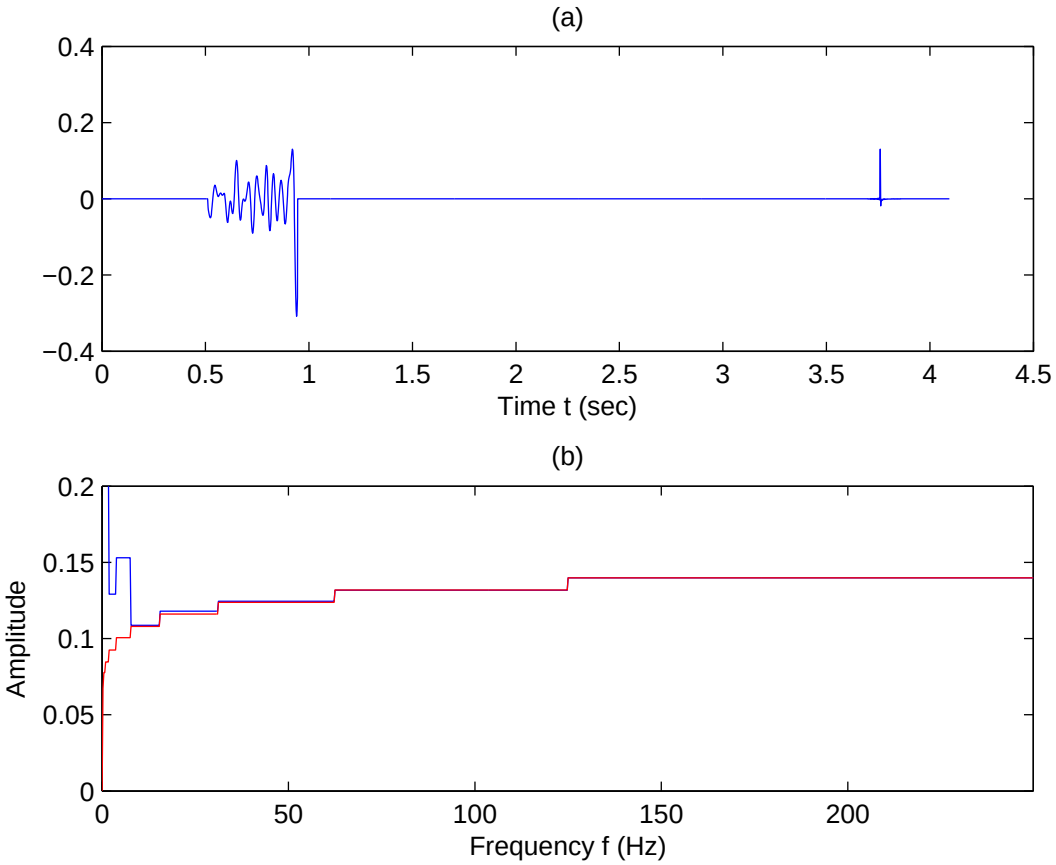

Figure 5.1: In (a) An anelastic reflection on the right and random reflectivity on the far left. Notice the large separation in time between the anelastic reflection and the other reflection events. In (b) The FST spectrum of the anelastic reflection (red) and the FST spectrum of the anelastic reflection with the random reflectivity present (blue). Notice that the spectrum of the anelastic reflection is interfered with by the random reflectivity at low frequencies and so the low frequency information cannot be used for AVF inversion.

5.3.1 FST estimation of local spectra of anelastic reflection coefficient in the presence of proximal reflections and their inversion

A decrease in the separation distance of events results in a greater portion of the local spectrum of the anelastic reflection being interfered with by the spectra of nearby events.

This is apparent when we compare Figure 5.1(b) to Figure 5.2(b). Notice that in Figure 5.2(b), where the separation distance is quite small, there is a greater portion of the spectrum of the anelastic reflection coefficient which is interfered with. However, we observe in Figure 5.2 that the estimate of the spectrum in the presence of numerous events (blue) tracks the analytic spectrum (red) in the high frequency region. Therefore, by only using the high frequencies we may implement AVF inversion. In Figure 5.3 we have plotted the inverted value of Q in red and the actual value of Q used to model the reflection (Q=13) against the separation distance. We can see that the AVF inversion estimate of Q is accurate until a separation distance of around 10 samples is reached and then the estimate degrades rapidly.

We then run this same experiment letting Q range from 8 to 46. Figure 5.4 summarizes the results. There are 9 panels in Figure 5.4, in each panel the separation distance is fixed. The separation distance decreases from Figure 5.4(a) to Figure 5.4(f). Then in each panel Q of the target reflector is varied from 8 to 46 and the inversion result is compared to the actual Q value used in the modeling. As can clearly be seen, there is an inconsistent ability of AVF inversion to predict Q. For instance, in Figure 5.4(f) the separation distance is 209 samples but the inversion is inaccurate for nearly all values of Q. In Figure 5.4(e), where the separation distance is 154 samples (and hence, the inversion result should be even less accurate) we see that the inversion is exceptional at predicting Q. This surprising result would suggest that the amplitude of the event nearest the anelastic reflection has a greater impact on the inversion result than the separation distance. In Chapter 3 we developed initial guidelines and observed that the cutoff frequency vs. the separation distance plot had a high level of variance. This is likely manifesting itself in the inversion results of Figure 5.4. A systematic study of AVF inversion consistency and the amplitudes of proximal events is an important future project.

5.4 Random noise

Because random noise is present in any seismic experiment, it is necessary to test the effectiveness of AVF inversion in its presence. We obtain a random noise vector to be added to our synthetic data by generating a time series containing random numbers drawn from the Gaussian distribution. We then add the random noise to synthetic traces containing a single anelastic reflection coefficient to generate data traces with a signal to noise ratio (SNR) of 7.67. These traces are then added input into the FST and the spectrum of the anelastic reflections is extracted and used to invert for Q. Figure 5.5 shows an example noisy trace. Figure 5.6 shows 9 attempts at performing AVF inversion on spectra derived from noisy traces. In each panel, the actual Q value (blue) and the inverted Q value (red) is shown. The experiment is repeated 9 times. The inversion is poor. This is not surprising as the FST algorithm averages over short time windows at high frequencies (for example, see Chapter 2 and Brown et al., 2010) and so noise will have a significant contribution to the output of the FST at high frequencies. To combat the effect of noise, repeat experiments should be performed (i.e. acquire numerous traces) and then the traces stacked to attenuate the random noise. To model this, we generate a set of synthetic traces with noise and stack them, which attenuates the random noise. Figures 5.7 and 5.8 are repeat experiments of the type shown in Figure 5.6. They illustrate how stacking improves the fidelity of the FST estimate of the spectrum of the reflection coefficient. In Figure 5.7, we stack ten traces together. The inversion accuracy improves. In Figure 5.8, we stack 35 traces and inversion accuracy improves even more. Notice from Figure 5.7 and Figure 5.8 that the inversion works best when Q is low. This is also expected as the variability of the reflection coefficient is higher for a larger contrast in Q.

5.5 Source wavelet

In order to implement AVF inversion to estimate the Q value of a target, we require an estimate of the local spectrum of the target reflection coefficient. However, the embedded wavelet imposes a footprint onto the spectrum of the reflection. This must be removed in order to implement AVF inversion.

To remove the effect of the embedded wavelet we can perform deconvolution of the seismic trace. To test how effective AVF inversion may be on deconvolved traces a number of synthetic traces are generated in which a single anelastic reflection is convolved with a minimum phase wavelet. We use the simple Earth model, such as shown in Figure 4.1, to generate the synthetic anelastic reflections. The traces generated from this model are then deconvolved using the Wiener deconvolution codes from the CREWES toolbox. Next the deconvolved trace is input into the FST to obtain an estimate of the anelastic reflection coefficient. This spectrum is then used to invert for Q using the modified AVF framework (Chapter 4). Figure 5.9 shows an example of a deconvolved trace obtained using Wiener deconvolution from the CREWES toolbox. In Figure 5.9(a) we see the anelastic reflection. In Figure 5.9(b) we see the anelastic reflection convolved with a minimum phase wavelet. In Figure 5.9(c) we see the result of deconvolution. The spectrum of the deconvolved result is obtained by utilizing the FST. An example of this is shown in Figure 5.10. The blue curve in Figure 5.10 is the FST spectrum of the anelastic reflection. The red curve in Figure 5.10 is the FST spectrum of the reflection after deconvolution. Notice that the amplitudes of the deconvolved result are lower than the spectrum of the analytic reflection. This is because the deconvolution code performs an rms power balancing of the input trace and the output deconvolved trace. The deconvolved result is broader band than the input trace and hence the amplitudes of the deconvolved output are uncalibrated after the rms power matching performed by the Wiener deconvolution. Because of this,

there is a discrepancy between the amplitudes of the deconvolved result and the analytic amplitudes. We illustrate this in Figure 5.11. In Figure 5.11(a) a random reflectivity series, in Figure 5.11(b) this reflectivity series is convolved with a wavelet. The result of deconvolving the trace in Figure 5.11(b) using Wiener deconvolution is shown in Figure 5.11(c). Notice that the amplitudes of the reflections in the deconvolved result are less than the amplitudes of the original reflectivity series. The amplitudes of the deconvolved result need to be calibrated to true amplitudes before AVF inversion can be implemented accurately.

5.5.1 Mean amplitude matching

A solution is found by plotting the amplitude spectra of input traces with an embedded wavelet and the output deconvolved result (Figure 5.12). The blue curve in Figure 5.12 is the spectrum of a trace composed of a random reflectivity convolved with a wavelet. The effect of the wavelet is to bandlimit the data outside the range of the dominant frequencies of the wavelet. The dominant frequencies lie roughly between 10 and 35 Hz. The deconvolved result is shown in black. It has the spectrum of a white reflectivity. The rms power balancing carried out during deconvolution uses the entire spectrum to balance the input trace (blue) and the deconvolved result (black). Therefore, as the input trace has a sharp drop in amplitude after 30 Hz, the mean amplitudes of the deconvolved result is somewhere between the high amplitude portion of the input trace (i.e., between 10 - 35 Hz) and the very low amplitudes at all other frequencies. As we can see in Figure 5.12, the amplitudes of the deconvolved result are less than the amplitudes of the input trace in the range of its dominant frequencies. This is why the amplitudes of the deconvolved result in Figure 5.10 are less than the input trace amplitudes. In order to calibrate the amplitudes of the deconvolved result, a ratio of the mean amplitudes of the deconvolved result and the input trace are found for the dominant frequency range of the

input trace. This ratio is used to boost the amplitudes of the deconvolved result. Figure 5.13 is the same as Figure 5.12 except that in it we highlight the region for which the ratio of mean amplitudes is extracted with vertical red lines. After applying the correction, the amplitude spectrum of the corrected deconvolved result and the analytic reflection are shown in Figure 5.14. Notice that the amplitudes of the corrected deconvolved result are much closer to the amplitudes of the analytic reflection coefficient.

5.6 The combined impact of proximal events, noise and wavelet on inversion

With the calibration of the amplitude spectrum of deconvolved traces, through an interpretive step, it is possible to use the corrected spectrum to invert for Q. The individual effects of noise, proximal events and a seismic wavelet have been examined for their effect on the local spectrum of an anelastic reflection. To test AVF inversion, synthetic traces are generated in which all of these adverse effects influence a target anelastic reflection located near the centre of the trace. An example of one of these traces is shown in Figure 5.15. These traces are generated using a random reflectivity and zeroing out a specified number of samples in the middle of the trace to control the separation distance. Then an anelastic reflection is manually added to this empty portion of the trace. These traces are then convolved with a wavelet and random noise is added. AVF inversion can be implemented by first stacking a number of these traces to attenuate the effect of random noise. Then we deconvolve the traces and perform the mean amplitude matching as described in the previous section to calibrate the deconvolved amplitudes. Finally, the traces are input into the FST and the spectrum of the reflection is obtained. Only the high frequency portion is suitable for AVF inversion due to the contamination of the low frequencies by proximal events. Figure 5.16 shows an example of an FST spectrum of the

anelastic reflection coefficient extracted from a trace such as shown in Figure 5.15. It can be seen from Figure 5.16 that deconvolution and then mean amplitude matching yields a good estimate of the spectrum of the anelastic reflection coefficient at high frequencies. However, repeating the experiment with a new random reflectivity, and extracting the deconvolved spectrum as shown in Figure 5.17 we can see that the results are inconsistent. Figure 5.17 is an example of a spectrum which will yield very inaccurate AVF inversion results. The AVF inversion scheme will predict a negative Q value due to the drop in amplitude at 125 Hz.

The workflow of stacking and deconvolution followed by mean amplitude matching and then finally estimating the spectrum before inverting is performed for a number of experiments. In one of these numerical experiments the separation distance and noise level are kept constant and the target Q is varied. In another, model Q and noise level are kept constant but the separation distance is varied. Finally, we perform an experiment where the separation distance and model Q are maintained constant but the noise level is varied. For each individual experiment, the inversion is performed 9 times. The results are displayed in Table (5.1) through to (5.3). Recorded in the tables is the median inversion value, the highest inversion value and the minimum inversion value. In Table (5.1), the model Q ranges from 50 to 5 and for each value of Q the test is performed 9 times. In Table (5.2), the model Q and the noise level are maintained constant and the separation distance is varied and in Table (5.3) we vary the noise level. Table (5.1), (5.2), and (5.3) show that AVF inversion produces inconsistent results especially for small separation distances, high noise levels, and high model Q values. As model Q is lowered, we obtain more consistent results but there are still some erroneous results. For example, in Table (5.1) for model Q of 5 there is an anomalous inversion result of -10. The same inconsistent results hold true for the experiments where separation distance and the noise level are varied. Even at large separation distances and low noise levels

there are inconsistent inversion results.

Table 5.1: Inversion values for varying model Q with constant separation distance and noise level

Actual Q	Inverted Q	Inverted Q (high)	Inverted Q (low)
50	9	53	-74
25	4	87	-23
15	10	93	-70
10	9	116	-39
7	9	24	-9
5	6	11	-10

Table 5.2: Inversion values for varying separation distance and constant noise level. Actual Q used in modeling is 5

separation distance	Inverted Q (median)	Inverted Q (high)	Inverted Q (low)
100	7	10	-10
80	8	21	-5
60	6	27	-6
40	8	36	-6
20	5	52	-30
10	4	22	-6

Table 5.3: Inversion values for varying noise level an constant separation distance. Actual Q used in modeling is 5

noise level (%)	Inverted Q (median)	Inverted Q (high)	Inverted Q (low)
2	10	18	-4
5	12	19	-2
10	8	17	-23

5.7 Conclusions

AVF inversion provides a frequency by frequency method of inverting for anelstitic paramaters of a target from seismic reflection data. It requires as input an estimate of the local spectrum of the anelastic reflection coefficient. In this chapter, we explore practical

issues affecting the implementation of AVF inversion in the presence of random noise and multiple reflection events. It is shown that proximal events interfere with the low frequency portion of the anelastic reflection and progressively affects higher frequencies as the events become closer. Also, an unexpected inconsistency of AVF inversion in the presence of numerous events is observed. Namely, that there is not a systematic decrease in the fidelity of the inversion with proximity of neighboring reflections. A systematic study of AVF inversion consistency in event-dense traces is an important future project. The effect of a source wavelet and deconvolution on AVF inversion is also studied. Deconvolution yields uncalibrated amplitudes which may be corrected for by mean amplitude matching of the deconvolved output and the input over the dominant frequency range of the input. After the calibration of the deconvolved traces, the FST had some remaining inconsistencies in its prediction of the spectrum of the reflection coefficient.

Further, we explore the effect of random noise in this chapter and observe that random noise degrades the fidelity of AVF inversion. To combat this, repeat experiments and stacking was performed and it was found that stacking helps in attenuating the random noise and improves the AVF inversion.

Estimation of an AVF signature from seismic data with sufficiently high fidelity to allow for accurate inversion is, we conclude, a difficult task. Our current signal analysis tools have been optimized for this but until future research is performed we must assume that examples of anelastic AVF inversion from field data will only be possible under ideal conditions.

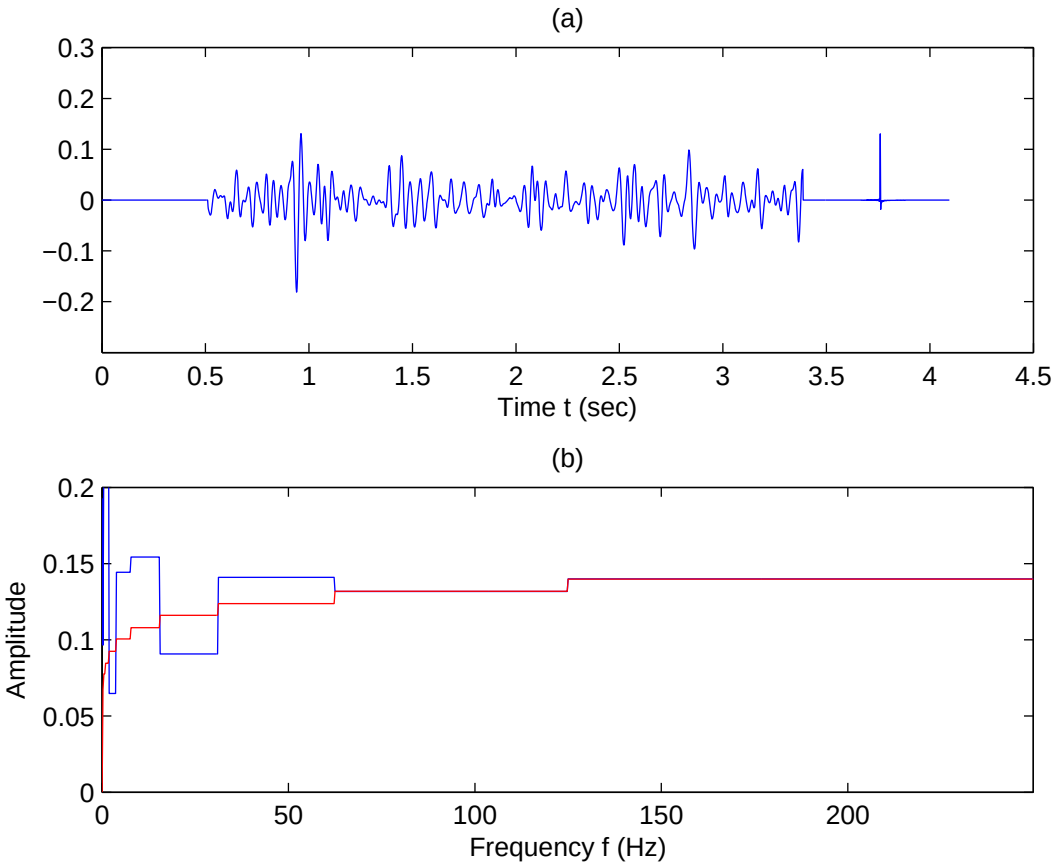

Figure 5.2: In (a) An anelastic reflection on the right and random reflectivity on the far left. Notice now that the separation in time between the anelastic reflection and the other reflection events is very small. In (b) The FST spectrum of the anelastic reflection (red) and the FST spectrum of the anelastic reflection with the random reflectivity present (blue). Notice that the spectrum of the anelastic reflection is interfered with by the random reflectivity for a much greater bandwidth than in Figure 5.1. This is due to the proximity of the nearby reflectivity.

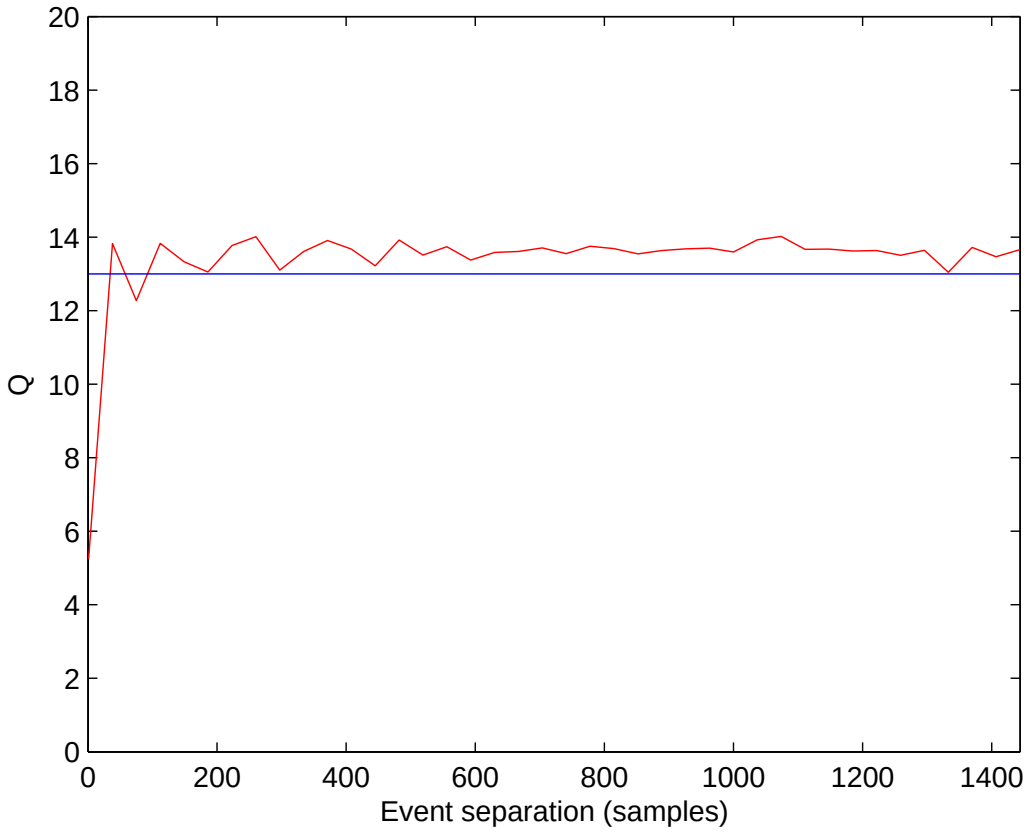

Figure 5.3: AVF inversion accuracy in the presence of proximal reflection events. On the x-axis is the separation in number of samples between the anelastic reflection and the nearest event. The blue line is the actual value of Q used in the modeling and the red line is the inversion result.

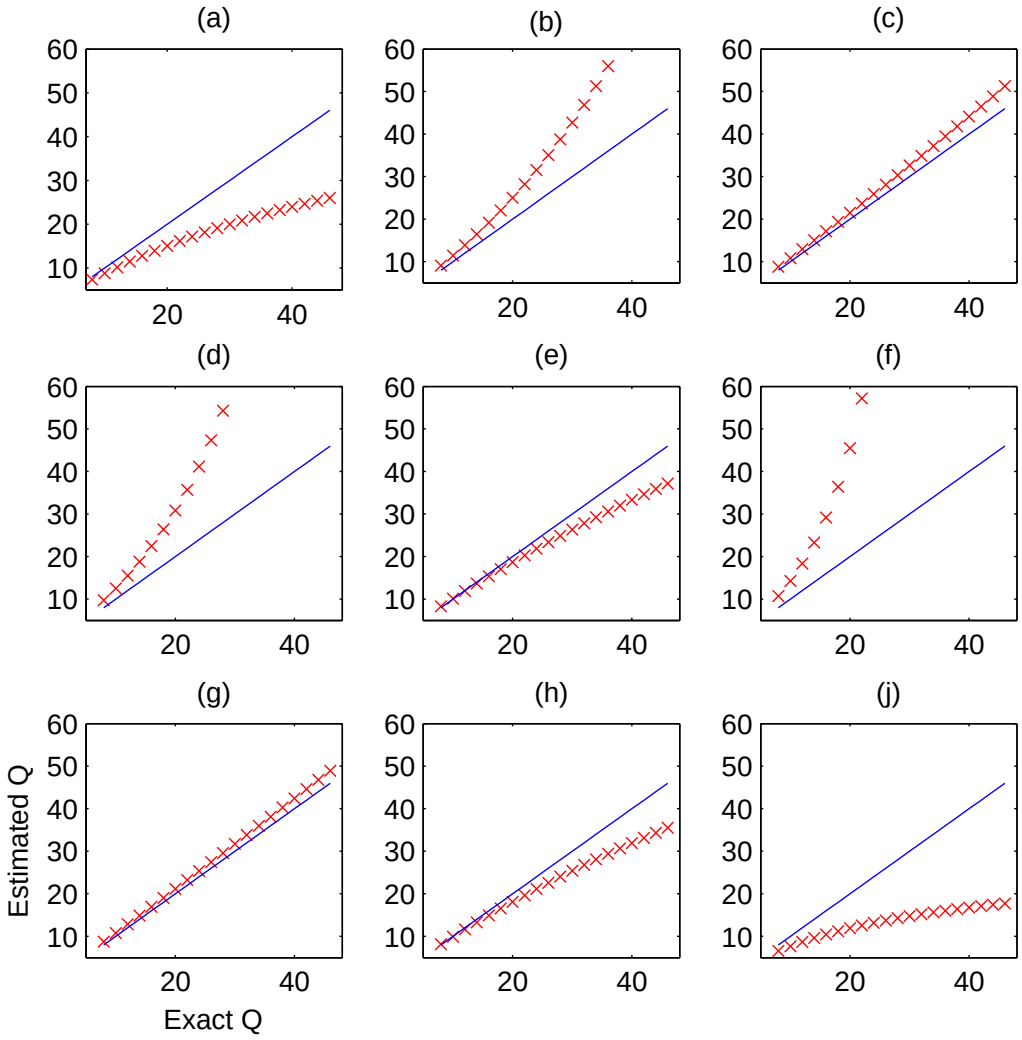

Figure 5.4: 9 panels showing the accuracy of AVF inversion. Each panel represents a different separation distance. (a) Separation distance of 484 samples. (b) 429 samples. (c) 374 samples. (d) 319 samples. (e) 264 samples. (f) 209 samples. (g) 154 samples. (h) 99 samples. (j) 44 samples. In each panel we see the inversion result (red x's) and the actual value of Q (blue). Notice that the separation distance does not appear to be the deciding factor in inversion accuracy. For instance, the inversion result for a separation distance of 99 samples is much better than for a separation distance of 209 samples, which is contrary to what we would expect.

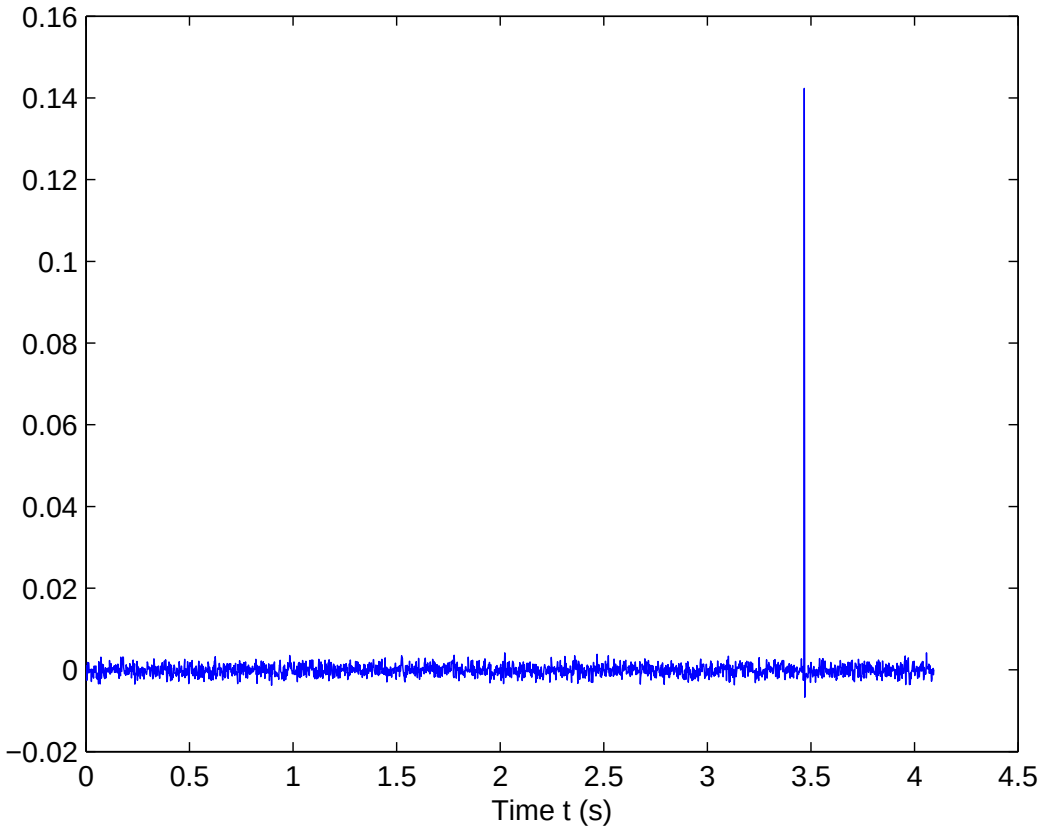

Figure 5.5: A trace with a single anelastic reflection and a SNR of 7.67.

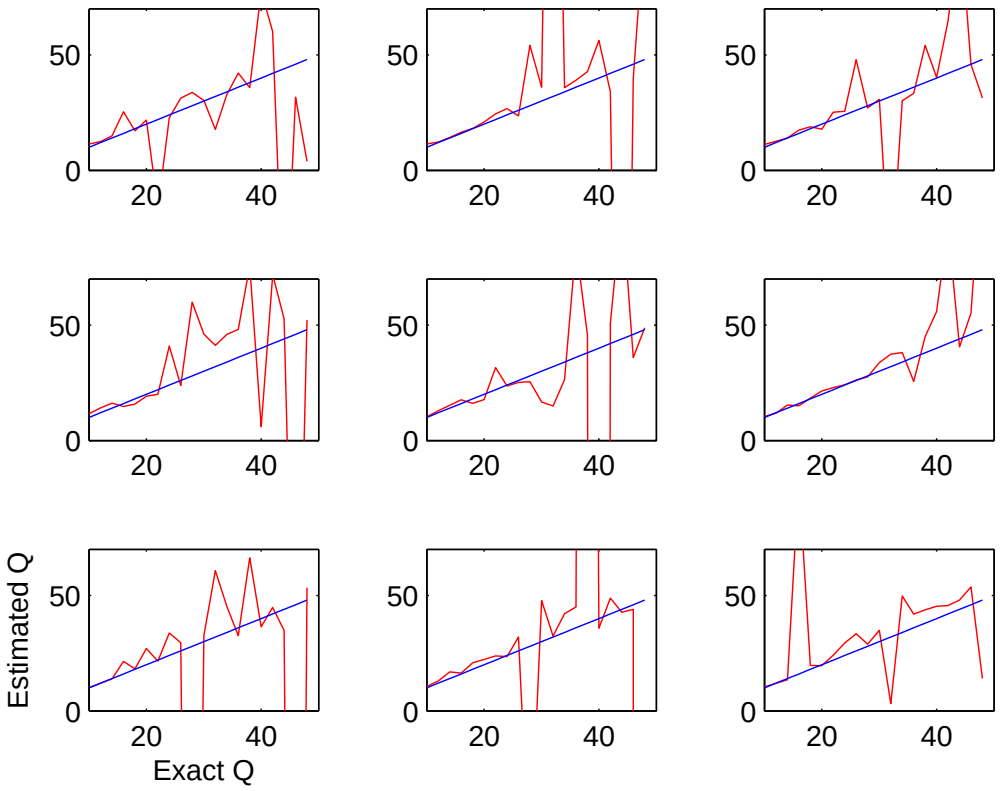

Figure 5.6: Accuracy of AVF inversion in the presence of random noise and no stacking. Each panel is a repeat experiment to gain statistical sampling of the inversion accuracy. Notice that the presence of noise greatly degrades the accuracy of AVF inversion. The SNR is 7.67.

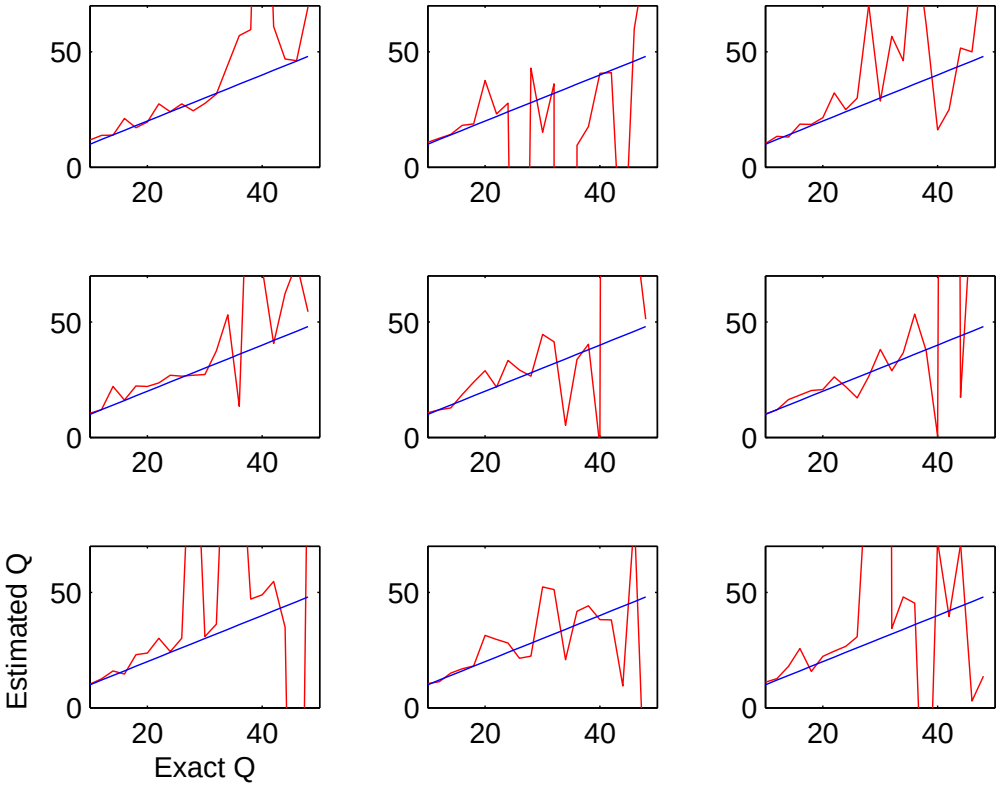

Figure 5.7: Accuracy of AVF inversion in the presence of random noise and 10 stacked traces. Each panel is a repeat experiment to gain statistical sampling of the inversion accuracy. The SNR of the stacked trace is 24.25. Notice that stacking 10 traces has somewhat improved the accuracy of AVF inversion, especially for low Q values.

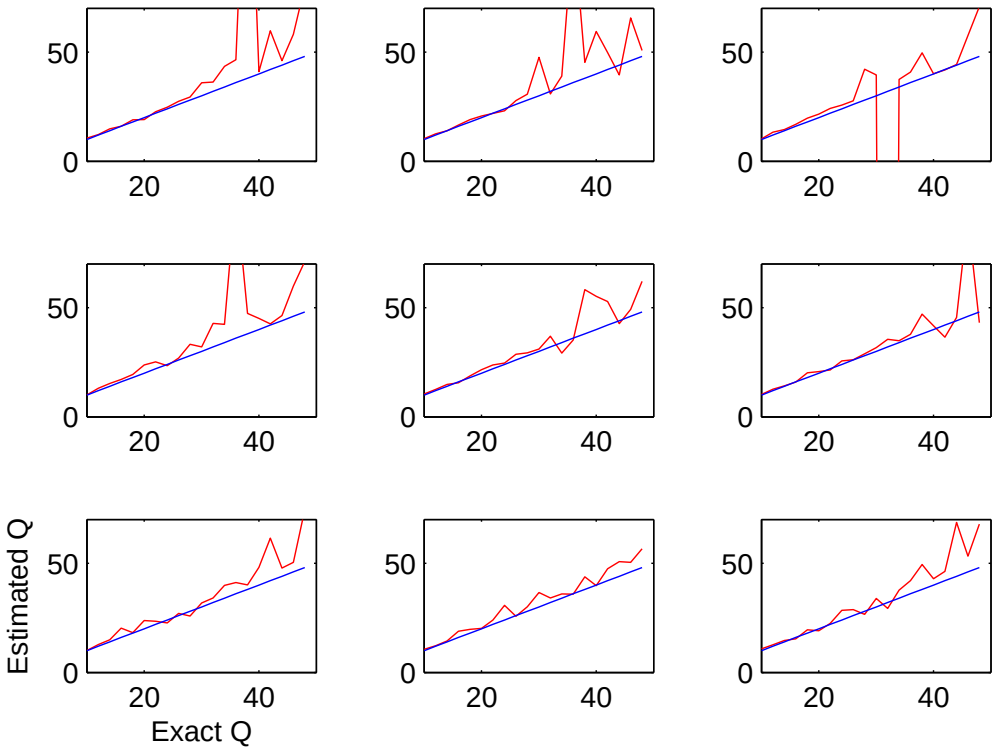

Figure 5.8: Accuracy of AVF inversion in the presence of random noise and 35 stacked traces. Each panel is a repeat experiment to gain statistical sampling of the inversion accuracy. The SNR of the stacked trace is 45.37. Notice that stacking 35 traces has greatly improved the accuracy of AVF inversion, especially for low Q values.

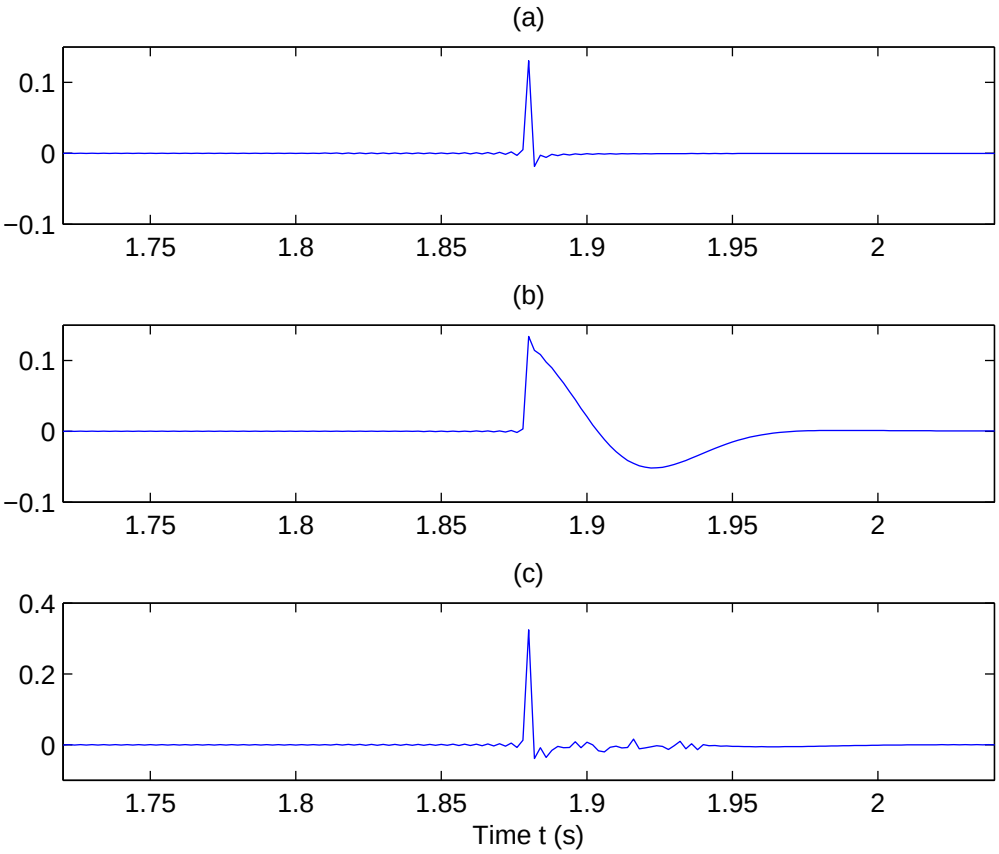

Figure 5.9: In (a) An anelastic reflection coefficient. In (b) The anelastic reflection coefficient is convolved with a minimum phase wavelet and in (c) The result of deconvolving the the trace in (b) using Wiener spiking deconvolution codes from the CREWES toolbox.

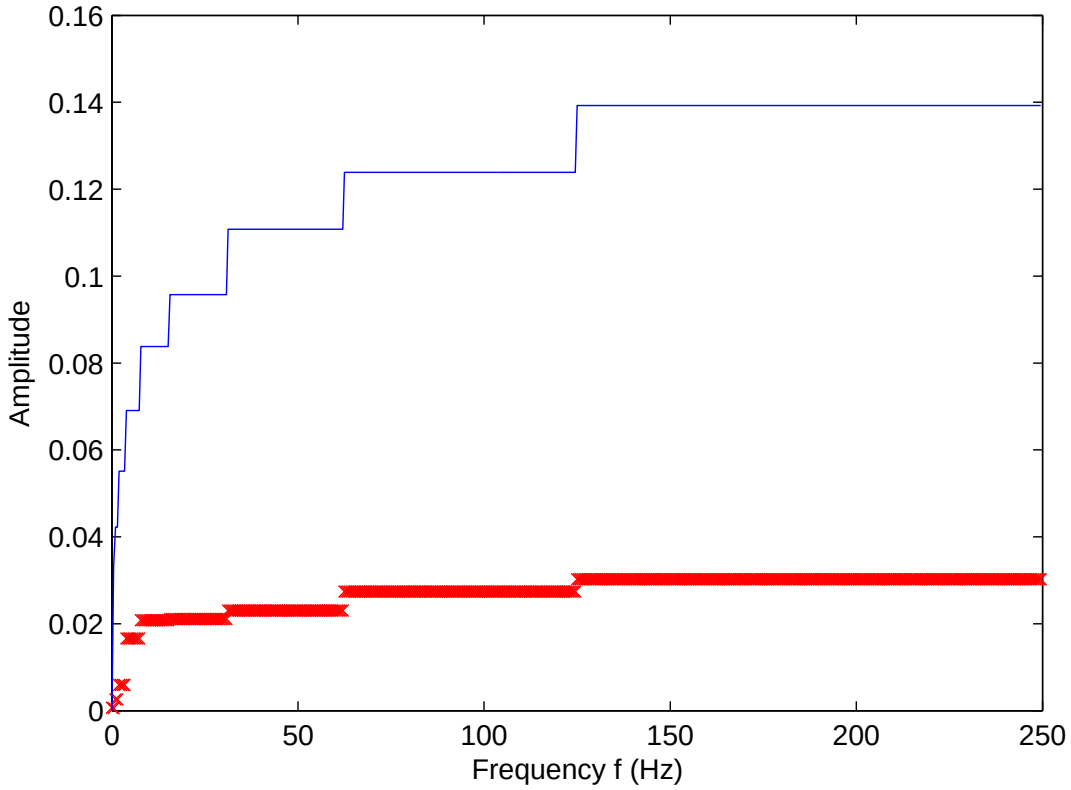

Figure 5.10: The blue curve is the FST spectrum of the analytic anelastic reflection coefficient. This anelastic reflection coefficient was convolved with a minimum phase wavelet and then deconvolved using Wiener deconvolution codes. The red curve is the FST spectrum of the deconvolved result.

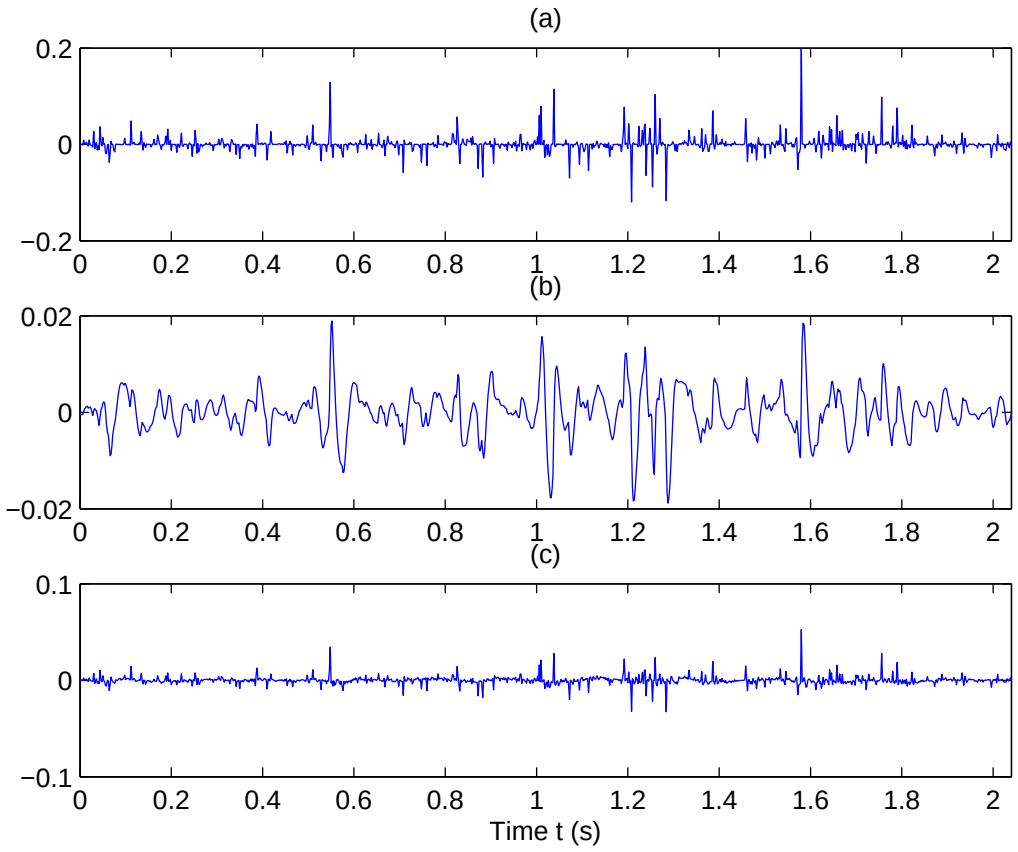

Figure 5.11: In (a) A random reflectivity series. In (b) The reflectivity series is convolved with a minimum phase wavelet and (c) The deconvolved result.

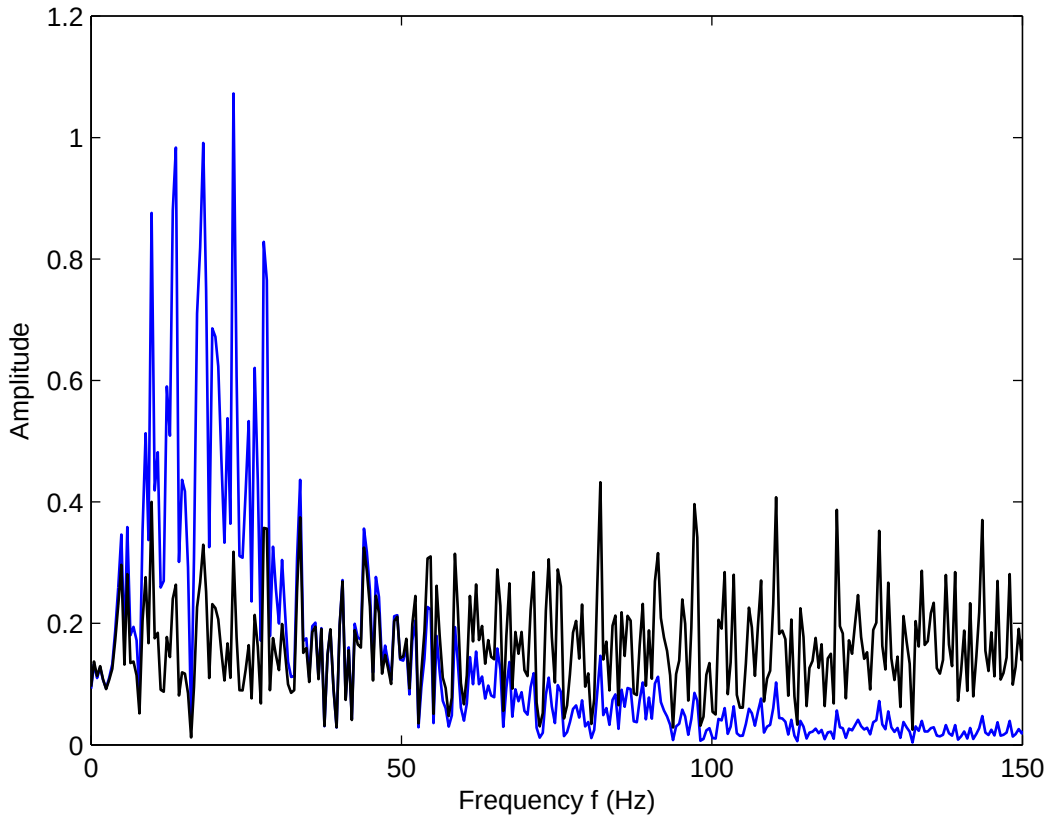

Figure 5.12: The blue curve is the amplitude spectrum of a reflectivity series convolved with a wavelet and serves as the input into the deconvolution code. The black curve is the spectrum of the deconvolved result. RMS power matching of the deconvolution code is performed across the entire bandwidth. Therefore, the deconvolved spectrum has lower amplitudes than the original trace over the bandwidth of the input.

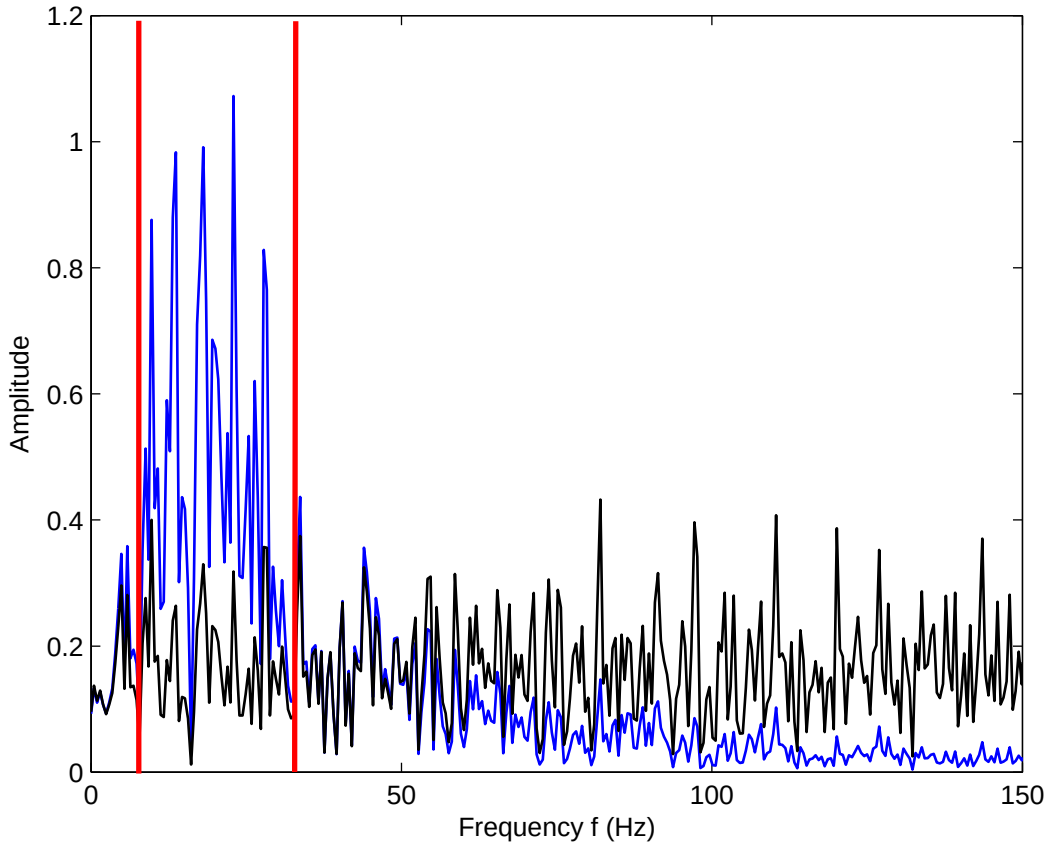

Figure 5.13: The blue curve is the amplitude spectrum of a reflectivity series convolved with a wavelet and serves as the input into the deconvolution code. The black curve is the spectrum of the deconvolved result. RMS power matching of the deconvolution codes is performed across the entire bandwidth so the deconvolved spectrum has lower amplitudes than the original trace over the bandwidth of the source wavelet. The vertical red lines show where the mean amplitude ratio was extracted to calibrate the spectrum of the deconvolved trace to obtain true amplitudes and implement AVF inversion.

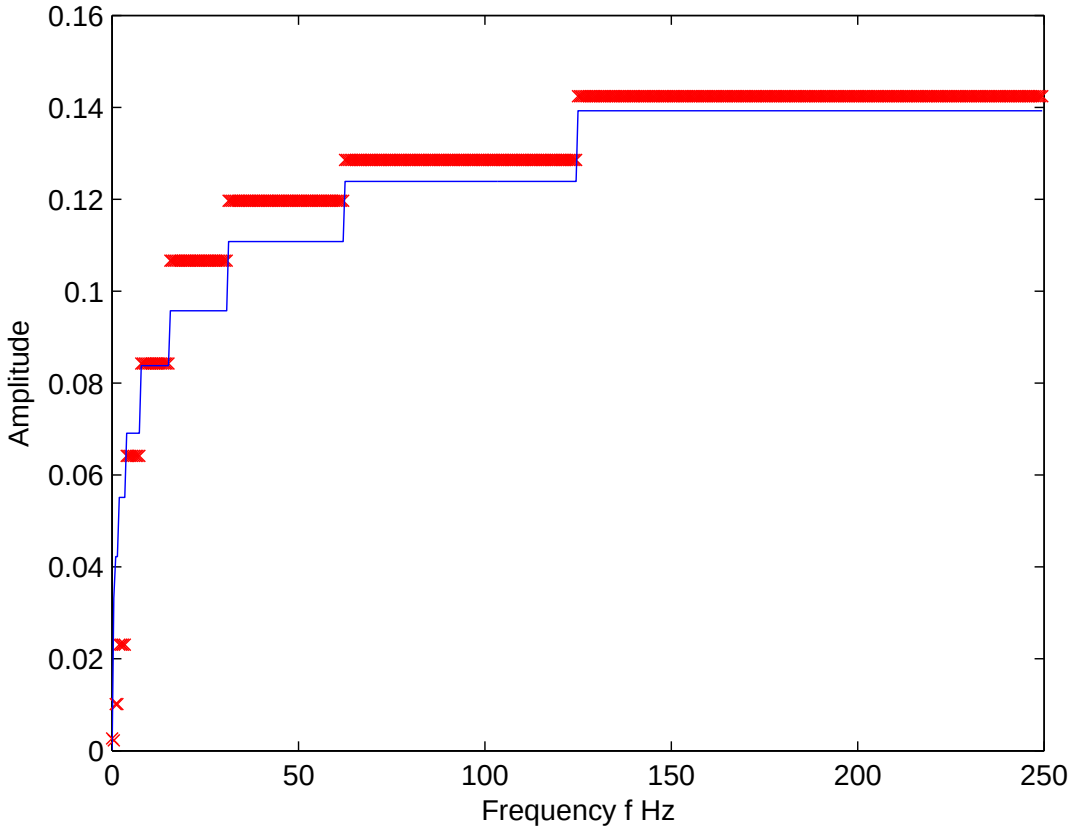

Figure 5.14: The result of mean amplitude matching the deconvolved spectrum. The blue curve is the FST spectrum of an analytic anelastic reflection coefficient. The red curve is the corrected FST spectrum of a deconvolved anelastic reflection coefficient after mean amplitude matching.

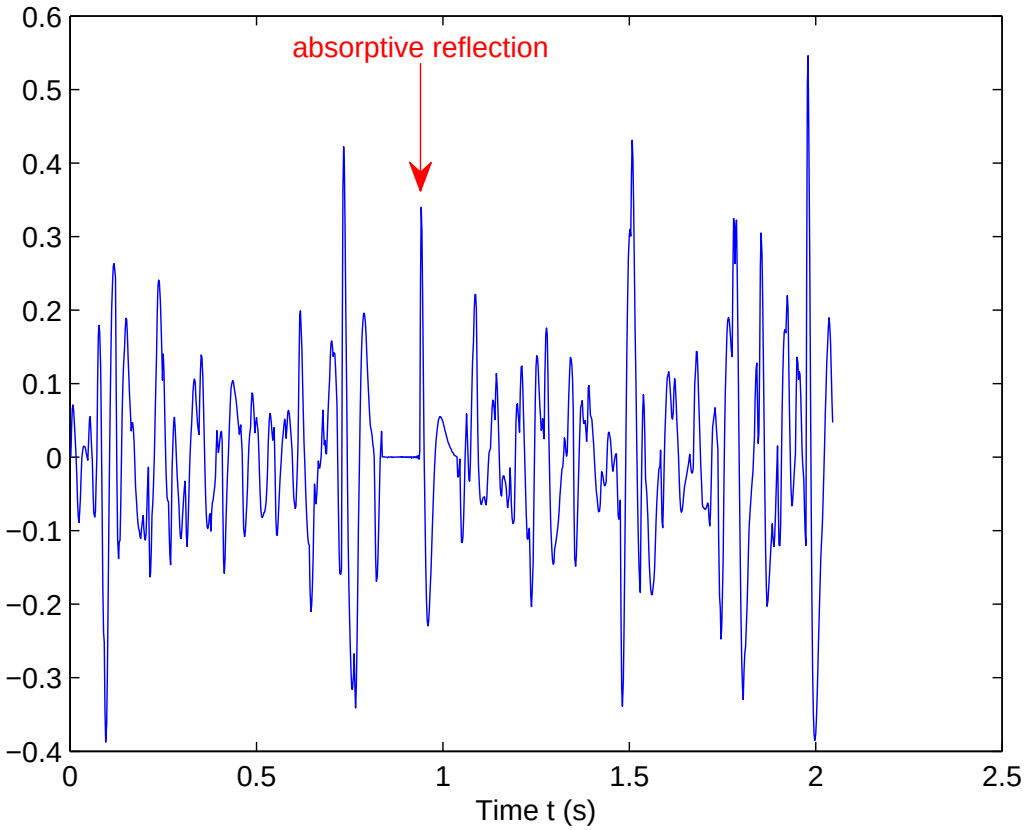

Figure 5.15: A random reflectivity, with an embedded anelastic reflection coefficient. The reflectivity series is convolved with a wavelet and random noise is added.

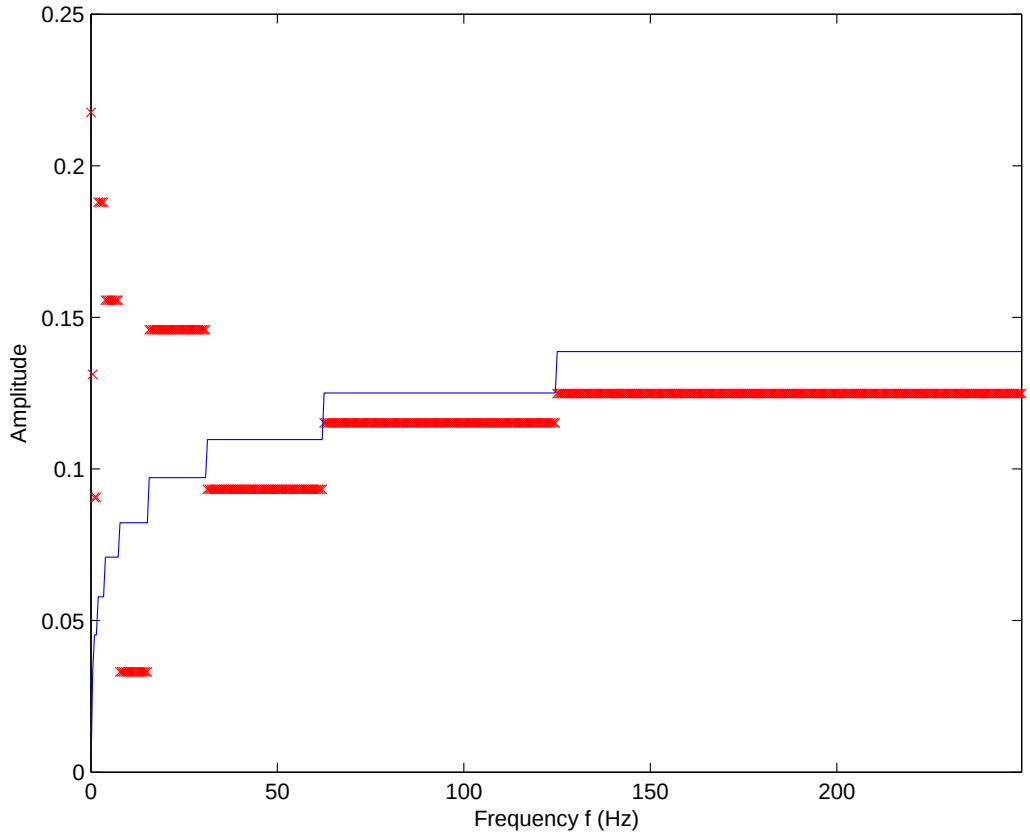

Figure 5.16: The blue curve is the FST spectrum of an analytic anelastic reflection coefficient. The red curve is the calibrated FST spectrum of the anelastic reflection extracted from traces such as shown in Figure 5.15.

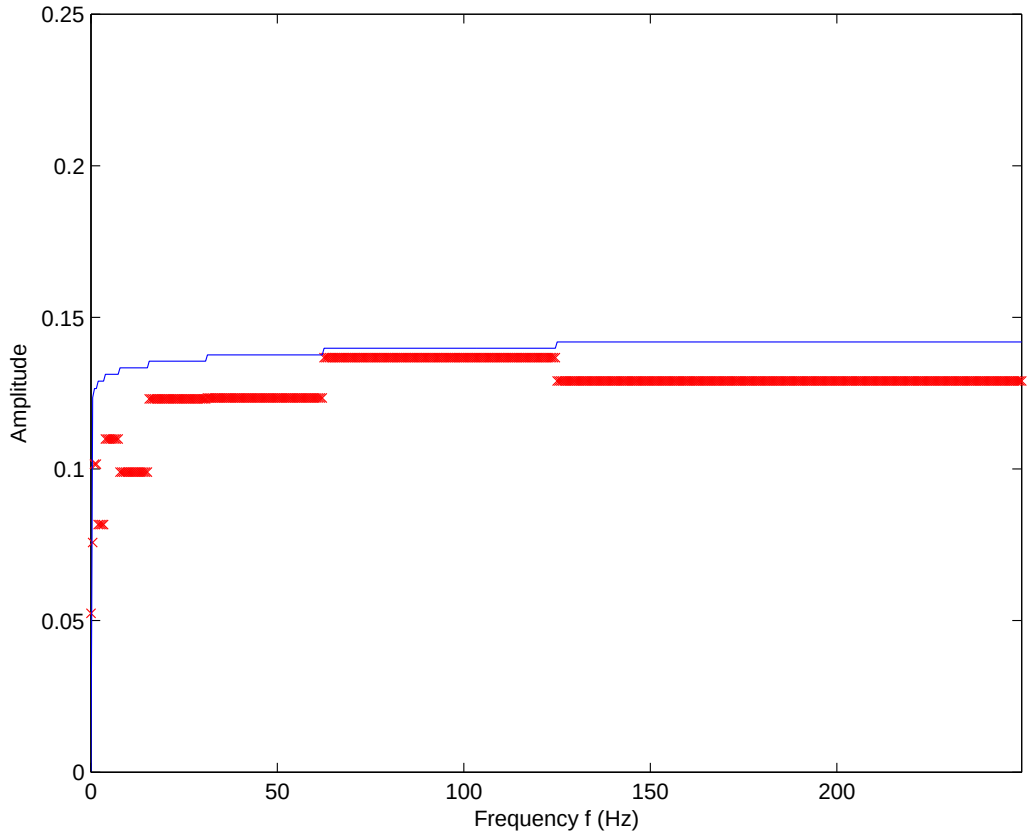

Figure 5.17: The blue curve is the FST spectrum of an analytic anelastic reflection coefficient. The red curve is the calibrated FST spectrum of the anelastic reflection extracted from traces such as shown in Figure 5.15.

Chapter 6

Identification of the AVF signature of an anelastic target in field data

6.1 Introduction

Large contrasts in anelastic properties of the Earth have frequency-dependent reflection coefficients (White, 1965; Kjartansson, 1979; Chapman et al., 2006; Lines et al., 2008; Quintal et al., 2009; Ren et al., 2009; Innanen, 2011). This represents a potentially valuable source of information with which to characterize fluid or gas bearing geophysical targets.

The dispersive amplitude-variation-with-frequency (AVF) signature in these reflections is likely subtle. Nevertheless, some field evidence of these variations has been reported (Odebeatu et al., 2006), and this evidence is further supported by a growing body of laboratory work (Lines. et al., 2011). Before the presence of such data variations in hydrocarbon-relevant field data is accepted community-wide, however, we require a larger number of convincing field cases. Our purpose in this chapter is to describe the methodology by which we might add to this number (or to the number of negative results), and show our initial results.

Evidence that anelastic reflections with dispersive AVF signatures are being generated above the ambient seismic noise level must come, initially, from environments with access to high levels of "ground truth", ideally in the form of instrumented wells. Vertical seismic profiling data sets are optimal in this regard. Vertical seismic profiling (VSP) is a method of seismic data measurement in which the wave field generated by a surface source is measured by receivers at numerous depth in a borehole (Hardage, 1985; Hinds

et al., 1996; Zhang, 2010). A major difference between VSP and surface seismic is that in a VSP experiment, both the upgoing and downgoing wavefields are recorded (Hardage, 1985). VSP surveys are valuable in delineating lithological, structural and stratigraphic properties of the subsurface and, of particular importance to this study, are also useful in determining physical properties of rocks such as absorption (Hardage, 1985; Zhang, 2010; Stewart, 2001).

To produce plausible examples of dispersive AVF signatures in VSP field data, we will require the following:

1. A field site with VSP data from a well which traverses geological structures with strong variations in Q;

2. A robust means of analyzing the local frequency dependence of an event, i.e., a tool for time-frequency decomposition of the seismic traces;

3. A means for separating the amplitude effects of transmission from those of reflection on a candidate AVF-rich event, i.e., a method for estimating the "bare" reflection coefficient;

4. A theory for determining the target Q from the AVF signature of the candidate event, which can be compared to independently derived Q estimates.

In previous chapters we have discussed items 2 (Chapter 3, Calibration of a fast S-transform), 3 (Chapter 2, Theory review) and 4 (Chapter 4, Anelastic reflection coefficients and their estimation). We will next review these and discuss the missing item.

6.1.1 Item 1: study area and VSP data set

The Ross Lake heavy oil field is located in the Southwest of Saskatchewan and is owned and operated by Husky Energy Inc. (Zhang, 2010). See Figure 6.1. The reservoir is

a channel sand, of Cretaceous age, in the Cantaur Formation of the Mannville group (Zhang, 2010). The Mannville group consists of sands and shales and is overlain by the carbonates of the Joli Fou formation (Zhang, 2010). See Figure 6.2 for a stratigraphic column.

In a collaboration between CREWES, Husky Energy, and Schlumberger Canada, a number of VSP experiments were performed in June 2003, including a zero-offset VSP, using the well 11-25-13-17W3. The data were acquired using 3-component receivers and both horizontal and vertical vibrators (Zhang, 2010). The receiver spacing in the borehole was 7.5m.

Zhang (2010) performed a Q analysis of the Ross Lake VSP data using the spectral ratio method (for details of which see, e.g., Hauge, 1981). A profile of Q from this effort can be seen in the far left panel of Figure 6.3. The profile suggests strong depth variability of Q.

6.1.2 Item 2: a calibrated fast S-transform

To identify an AVF signature in the local spectrum of the reflection coefficient, a method of time-frequency decomposition is required. As discussed in Chapter 3 we have a calibrated FST which our testing indicates offers high fidelity estimates of the local spectra of reflection events. The output of the FST are "blocky" local spectra—averages over frequency bands, as opposed to pointwise spectra.

6.1.3 Item 3: a method for estimation of reflection strengths from VSP data

As developed by Lira et al. (2011) and presented in Chapter 2 we have a processing strategy whereby the amplitude of a reflected VSP event may be corrected to remove all transmission influences, leaving the "bare" reflection coefficient. The method is in principle applicable in the time or the frequency domain, and hence in the presence of

Figure 6.1: Map of western Canada showing the Ross Lake heavy oil field. From Zhang (2010), used with permission.

a suitable time-frequency decomposition is able to determine the raw spectrum of the reflection coefficient. It amounts to the division of the upgoing field by the downgoing field at or just above the reflection event. We will refer to this method as Lira's method.

6.1.4 Item 4: AVF inversion of anelastic reflectivity

Finally, we have access to a frequency-by-frequency (AVF) method of inverting for Q from the frequency dependent absorptive reflection coefficient, developed by (Innanen, 2011). In chpater 4, we modified AVF inverse theory for use on data in the fast S-transform domain. In Chapter 5 this approach is tested extensively on synthetic data,

in the presence of noise, a seismic wavelet and proximal events.

6.2 A candidate reflector

There is a large contrast in Q at the boundary between the Joli Fou Formation and the Mannville Group at approximately 1100m depth (Figure 6.3): the quality factor in the Joli Fou carbonates is above 120 whereas Q at the top of the Mannville is about 50. Because of this contrast in Q, the primary event from the top of the Mannville is a potential example of a dispersive AVF reflection (Innanen, 2011). We now focus on the reflection associated with this event, which we will refer to as the Mannville reflection.

6.3 Pre-processing

Having identified a candidate reflector and its associated reflected event in the VSP data set, we must next process these data such that the "bare" reflection coefficient (i.e., the amplitude corrected for all transmission effects) is exposed as a function of frequency. This requires that we separate the direct wave from the reflected wave when they are quite close to each other, and the problem of doing this stably accounts for most of the processing issues discussed here.

We will use Lira's method twice: once, to obtain an estimate of the Mannville reflection coefficient, and once more, as a control, on a primary from the Lea Park/Milk River interface (Figures 6.2 and 6.3) in which there is very little associated contrast in Q. We will the control reflection with the Mannville reflection.

6.3.1 Avoidance of wave field separation

The zero-offset VSP data are plotted in Figure 6.4 with the two interpreted reflections. Lira's method involves forming the ratio of the reflected to the direct events as near as

possible to their point of coincidence. Elsewhere this has been accomplished by applying a wave field separation algorithm based on median filtering (Hinds et al., 1996, for example, see), but we did not, in this case, because the median filtering could potentially remove the AVF signature, if it exists, from the data. This means we will be forced to compare these events at shallower depths, where they are further apart.

6.3.2 Applying the FST and choosing the bandwidth

In order to provide the numerator and denominator for the division called for by Lira's method, we applied the FST to the VSP data, and extracted the spectra at the times of the interpreted events. The data used for the FST spectrum extraction is the zero-offset, stacked z-component of the full (i.e., non separated) wave field at a chosen depth. The data input into the FST does not have an AGC applied to it, however there is an AGC applied to the data in Figure 6.4 to make the reflectors more visible to the reader. The depths of the traces used are discussed further below.

Only a portion of the bandwidth contains useable signal. The low frequency range will be contaminated by nearby seismic events and so we must exclude the low frequencies from analysis; in our case, the exclusion was of frequencies below 31 Hz. Also, Zhang (2010) determined that the signal contains energy only up to 95 Hz so we have included the FST band 62-124 Hz but none higher.

6.3.3 Compensation for the finite Q of the overburden

Since the full (un-separated) wave field is used, to distinguish between the reflection and the direct event we must use receivers which are a significant distance up the borehole from the reflector. In Figure 6.4 the reason is clear: the direct arrival dominates the signal so strongly that the primary is not visible until it travels up to the receiver located at 857m depth, a distance of approximately 240m above the reflector.

This non-negligible distance can re-introduce some of the transmission effects Lira's method is designed to suppress. However, (Lira et al., 2011) showed that the approximation of the reflection coefficient in an attenuative medium is given by

$$R_{est} = \frac{|P|}{|D|} = R \times e^{(i\tilde{k}n-12(z_n-z_x))}. \tag{6.1}$$

Here z_n is the depth to the reflector, z_x is the depth to the receiver and R_{est} is the estimate of the true reflection coefficient, R, obtained by dividing the spectrum of the primary $|P|$ by the spectrum of the direct wave $|D|$. Recall from Chapter 2:

$$\tilde{k}_{n-1} = \frac{\omega}{c_{n-1}}\left[1 + \frac{F(\omega)}{Q_{n-1}}\right], \tag{6.2}$$

where $\tilde{k}_{n-1}$ is the complex wavenumber in the layer above the reflector, c_{n-1} is the velocity in the layer above the reflector, Q_{n-1} is the quality factor in the layer above the reflector and

$$F(\omega) = \frac{i}{2} - \frac{1}{\pi}\log(\omega/\omega_r). \tag{6.3}$$

In our field data set the measurement of the primary is approximately 240m above the reflector, and so we may not assume that $\exp[(i\tilde{k}_{n-1}2(z_n - z_x))] \approx 1$. Instead, we use averages of Zhang's estimates of Q (Q_{ave}) and velocity (c_{ave}) in the region between the reflector and the receiver (Zhang, 2010, as seen in Figure 6.3) and correct our reflection by the inverse operator:

$$\begin{aligned} R_{cor} &\approx \frac{R_{est}}{\exp\left(\left[i\frac{\omega}{c_{n-1}}\left[1 + \frac{F(\omega)}{Q_{n-1}}\right]2(z_n - z_x)\right]\right)} \\ &= \frac{|P|}{|D|}\exp\left(\left[i\frac{-\omega}{c_{n-1}}\left[1 + \frac{F(\omega)}{Q_{n-1}}\right]2(z_n - z_x)\right]\right). \end{aligned} \tag{6.4}$$

6.4 Results

Following the above prescription, we:

1. Locate a depth in the VSP data set at which the Mannville reflection and the direct wave are separable;

2. Calculate the FST spectra of both of these events, and focus on the useable frequency bands;

3. Estimate the Mannville reflection coefficient $R(\omega)$ by dividing the reflected FST spectrum by the direct FST spectrum;

4. Compensate the result for attenuation on the path down and back from the receiver depth to the reflector.

In this section we examine the results, looking for supporting evidence (or otherwise) for anelastic AVF behaviour in reflections from large Q contrasts.

6.4.1 Blocky FST spectra: review

For the reader's "mental benchmarking" we recall that the FST produces averages of spectra over pre-defined frequency bands and has a blocky appearance. Consider Figure 6.5, the blue curve is the analytic spectrum of an anelastic reflection coefficient and the black, blocky curve is the FST spectrum of the anelastic reflection coefficient.

6.4.2 Preliminary positive evidence

In Figure 6.6(a) we see the FST spectrum of the direct wave recorded at the receiver at a depth of 842.3m. In Figure 6.6(b) we see the FST spectrum of the Mannville primary also recorded at 842.3m depth. The amplitudes of both the direct wave and the primary are corrected for geometrical spreading. The blue curve in Figure 6.6(c) is the estimate of the frequency dependent reflection coefficient obtained by dividing the spectrum of the primary (b) by the spectrum of the direct arrival (a) before Q-compensation. The red curve in Figure 6.6(c) is the estimate of the frequency dependent reflection coefficient after Q-compensation. The black vertical line in Figure 6.6(c) illustrates the cutoff below which the low frequencies are excluded due to interference from nearby events.

Figure 6.6c shows that, after Q-compensation, there is an increase in the amplitude of the reflection coefficient at 62 Hz. This behavior is consistent with standard Q models, and represents evidence that the Mannville reflector has the desired dispersive character.

6.4.3 Mitigating evidence

In order to evaluate whether the trend shown in Figure 6.6(c) could be an AVF signature we use Lira's method to extract an estimate of the reflection coefficient of a primary in which there is no contrast in Q. We choose then, a reflection which occurs at roughly 600m, which is interpreted as being associated with the interface between the Lea Park and Milk River Formation (henceforth we refer to this reflection as the Milk River primary; see Figure 6.2 for the stratigraphic column). Figure 6.4 also shows this reflection on the VSP data, interpreted in green.

Again, the signal is so dominated by the direct arrival that we do not see signal for this reflection until over 200m above the reflector. We apply Lira's method of estimating the frequency dependent reflection coefficient as we did for the Mannville reflection. Figure 6.7(a) is the spectrum of the direct wave recorded by the receiver at 392.3m depth and 6.7(b) is the FST spectrum of the primary reflection from the Milk River also recorded at 392.3m depth. The amplitudes of both the direct wave and the primary are corrected for geometrical spreading. Figure 6.7(c) shows the spectra of the estimated reflection coefficient with the blue curve representing the estimate before Q-compensation and the red curve after Q-compensation. Again, the low frequencies are disregarded.

We see that there is an increase with amplitude of the Q-compensated reflection coefficient at roughly 62 Hz in the Milk River reflector also. It is not expected that there would be an AVF signature in the reflection coefficient for this primary as there is no associated contrast in Q. Figure 6.8 shows the spectra for both the Milk River and Mannville primaries for comparison. The frequency dependence of the two are of

comparable order.

We also calculate the spectrum of the reflection coefficients using the first three receivers which record primaries for both reflectors and plot the results (Figure 6.8). Notice that, generally, the Q-compensated reflection coefficients exhibit an increase in amplitude at 62.5 Hz for both the Mannville and Milk River.

Because we use average values of Q (obtained from a spectral shift method) and velocity, the frequency dependence we see in both reflection coefficients could simply be due to over-compensating the amplitudes at high frequencies. Because Q values are so low above the Milk River reflector, the Q compensation step in equation (6.4) may be having an unduly large influence on the results.

6.5 Conclusions

We wish to confirm or refute the presence of the theoretically predicted anelastic AVF behaviour of reflection coefficients from large Q contrasts. To do so, we applied a method developed by (Lira et al., 2011), for estimating the frequency dependent reflection coefficient by comparing direct and reflected VSP events, to a zero-offset VSP data set from the 11-25-13-17W3 well in the Ross Lake Heavy oil field of Southwest Saskatchewan. Using the FST we obtained the spectra of both the primary and direct wave for the Mannville reflection, which a transmission analysis (Zhang, 2010) suggests is associated with a fairly large contrast in Q.

It is observed that there is an increase in the amplitude of the Mannville reflection coefficient at 62Hz, which is consistent with an AVF signature. However, in our control event, the Milk River reflection, which is not thought to be associated with a contrast in Q, we again find an increase in amplitude with frequency.

We suspect that the Q compensation step in the processing of the control (Milk River)

event may be overcorrecting, however, since this reflector's overburden has a very low Q. A project of future work will be to compare the Mannville reflection to a better control, ideally with almost infinite Q in the overburden.

Another project of future work should investigate other forms of separation of the upgoing and downgoing fields. Avoiding the Q compensation step entirely will likely add stability to our search.

When we are more satisfied with our estimate of the spectra we will also invert the spectral information to estimate the target Q. The proximity of the inverted result to the (independently derived) Q profile will be further evidence for or against the presence of the AVF signature.

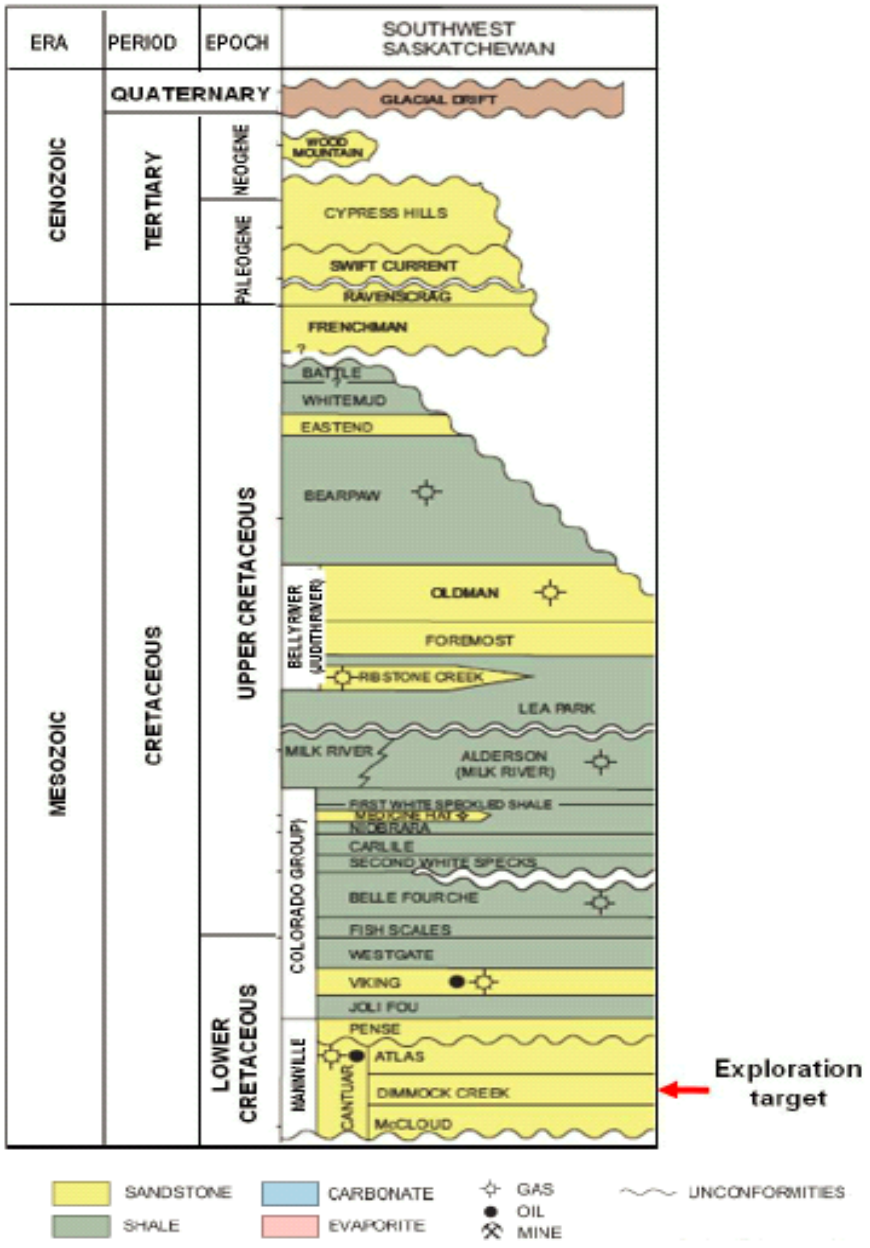

Figure 6.2: Stratigraphic column of study area. At the 11-25-13-17W3 well, the depth to Mannville formation is about 1100 meters. From Saskatchewan Industry and Resources, 2006 adapted from (Zhang, 2010).

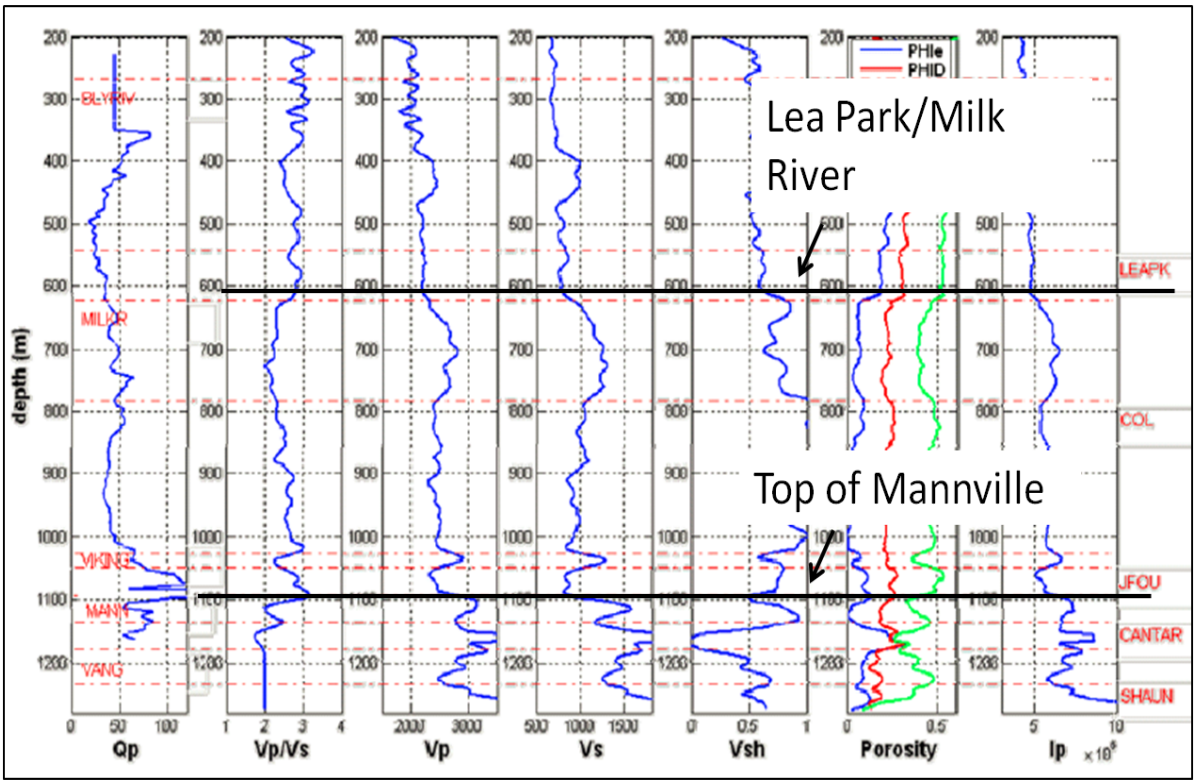

Figure 6.3: Ross Lake parameter profiles. On the left-most panel is the Q profile derived using a spectral shift method. Indicated are two reflecting horizons, the top of the Mannville group and the Lea Park/Milk River interface. From (Zhang, 2010), used with permission.

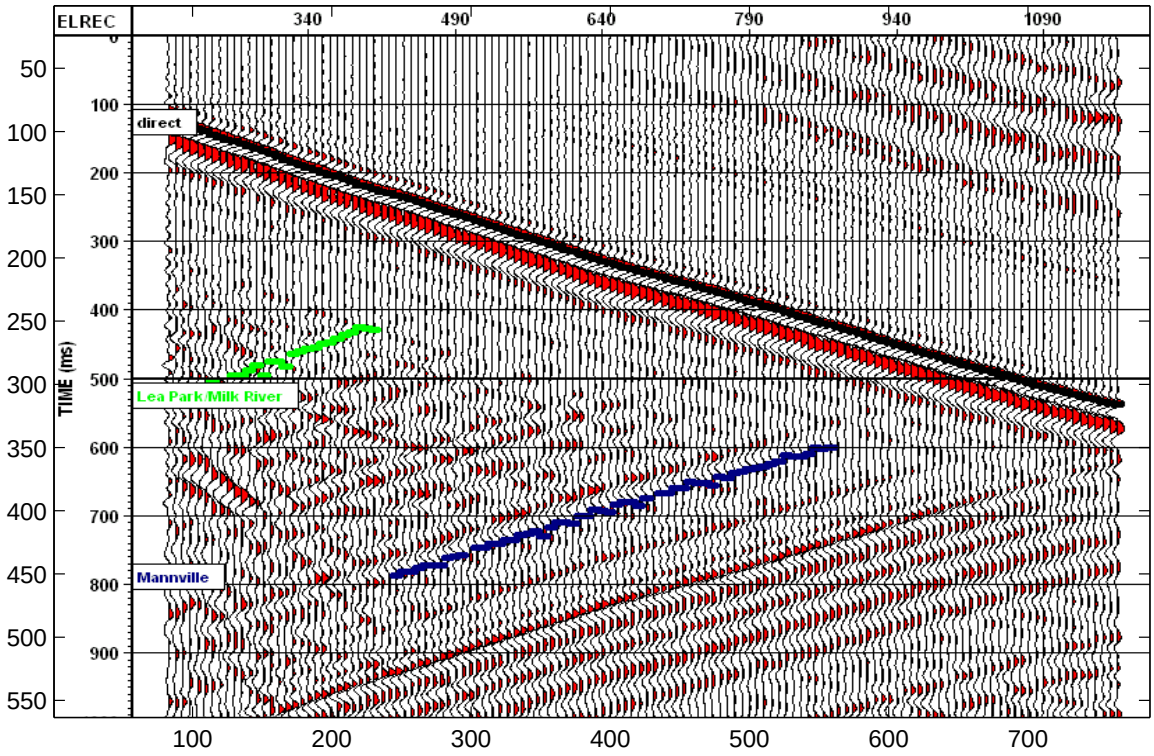

Figure 6.4: VSP data from the 11-25-13-17W3 well in the Ross Lake heavy oil field. The interpreted Mannville (blue) and Milk River (green) primaries are displayed. The direct arrival is displayed in black. An AGC is applied here to make the reflectors more easily visible.

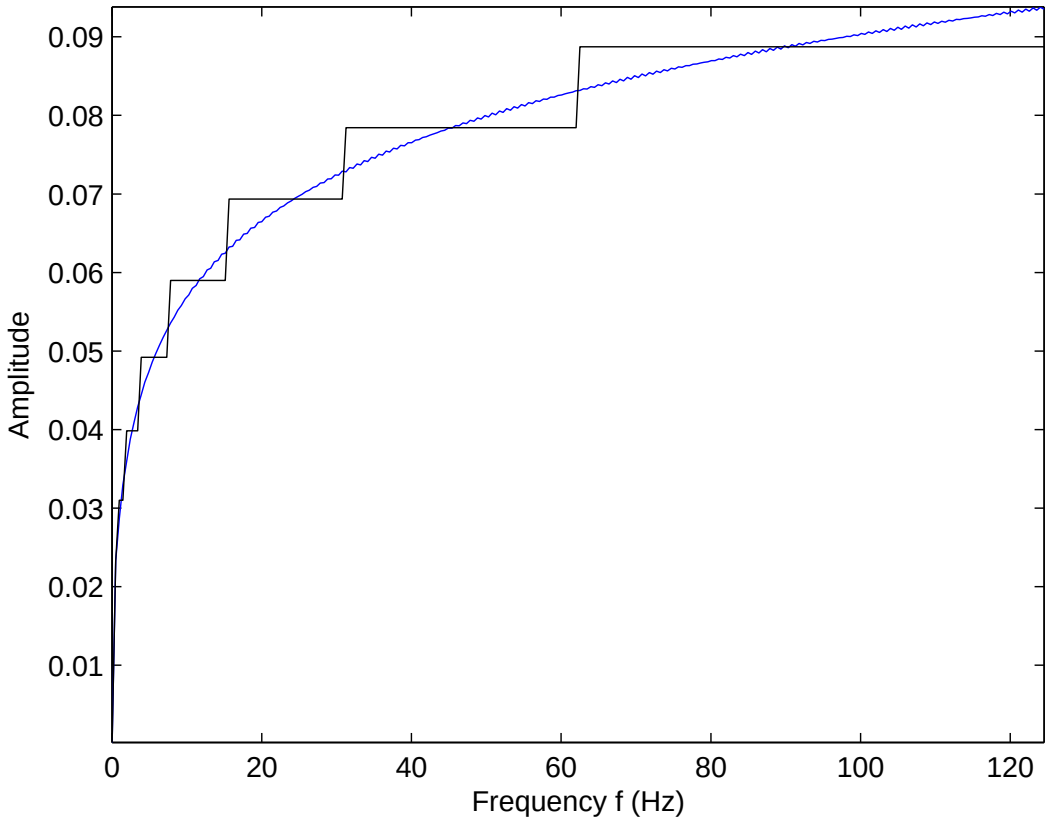

Figure 6.5: Analytic anelastic reflection coefficient (blue). The FST estimate of the reflection coefficient (black).

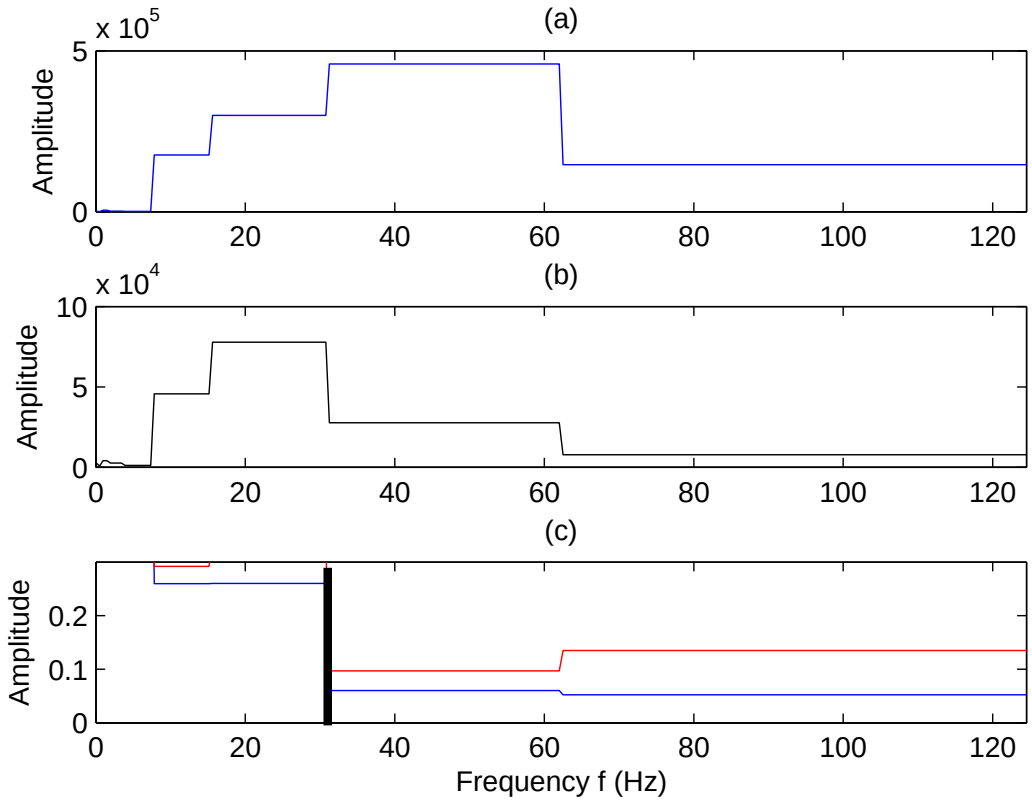

Figure 6.6: Evidence of dispersive AVF reflections. (a) The spectrum of the direct arrival recorded by the receiver at 842.3 m depth; (b) The spectrum of the primary reflection from the top of the Mannville formation and recorded by the receiver at 842.3 m depth. (c) The estimate of the reflection coefficient with Q-compensation (red) and without (blue).

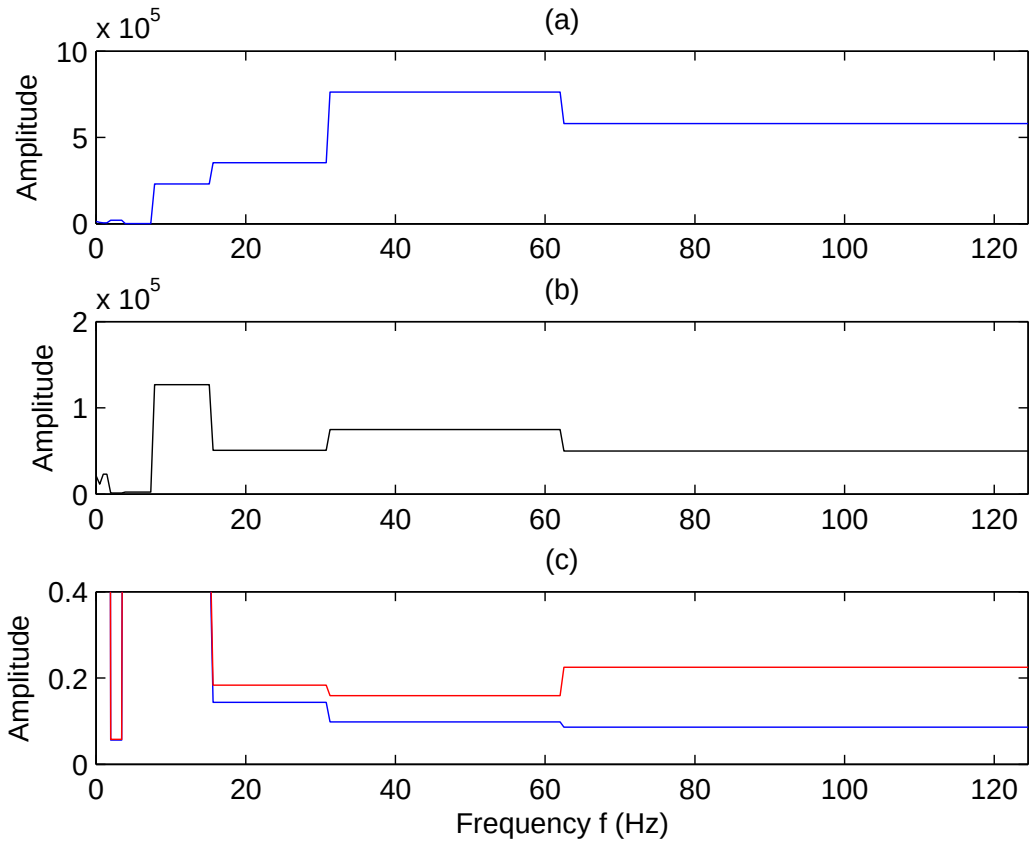

Figure 6.7: (a) The spectrum of the direct arrival recorded by the receiver at 392.3 m; (b) The spectrum of the primary reflection from the top of the Milk River formation and recorded by the receiver at 392.3 m; (c) The estimate of the reflection coefficient with Q-compensation (red) and without (blue).

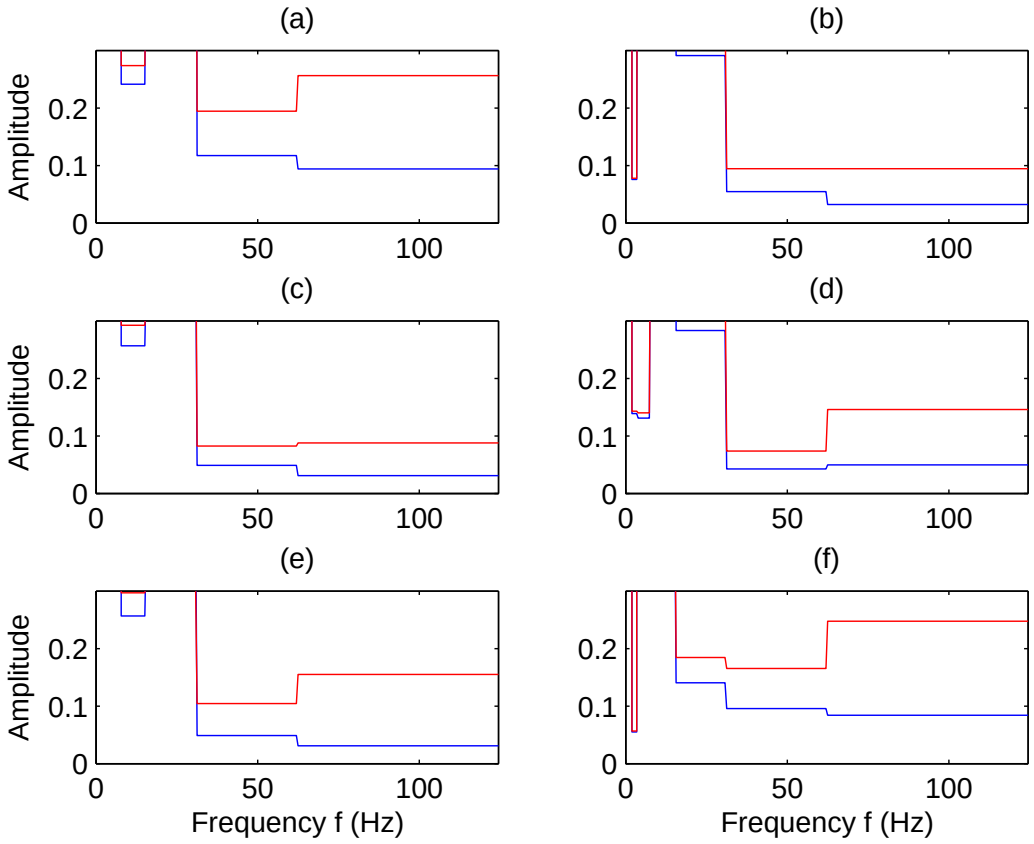

Figure 6.8: Comparison of the Mannville and Milk River reflection coefficients as calculated from the first three receivers to record primaries. In (a) The Mannville reflection coefficient calculated from the receiver located at 857.4 m depth. (c) The Mannville reflection coefficient calculated from the receiver located at 849.8 m depth. (e) The Mannville reflection coefficient calculated from the receiver located at 842.3 m depth. (b) Milk River reflection coefficient calculated from the receiver located at 407.4 m depth. (d) Milk River reflection coefficient calculated from the receiver located at 399.8 m depth. (f) Milk River reflection coefficient calculated from the receiver located at 392.3 m depth. In all panels the blue curves are the spectra of the reflection coefficients without Q-compensation and the red curves are the spectra of the reflection coefficients with Q-compensation.

Chapter 7

Other advances in inversion of anelastic reflectivity

7.1 Introduction

An effective AVF workflow requires that we have

1. A method of time-frequency decomposition which provides accurate estimates of local spectra of reflection coefficients, and

2. Processing steps to account for/mitigate the effect that other seismic phenomena have on the spectrum of a reflection coefficient.

To satisfy item (1) we calibrate a fast S-transform (FST) algorithm to provide high fidelity estimates of the local spectrum of reflection events (Chapter 3). Further, in Chapter 4 we reformulate linear AVF inverse theory to take FST spectra as input and test inversion accuracy using the modified equation to find accurate results. In Chapter 5 we satisfy item (2) by examining the adverse effect of random noise, a source wavelet, and proximal events on AVF inversion and make recommendations to mitigate these effects. We find that the increase in signal to noise created by stacking diminishes the adverse effect of random noise. Disregarding the low-frequency portion of the target reflection coefficients spectrum improves inversion accuracy in the presence of nearby events but surprisingly, we find accuracy of inversion inconsistent even with this measure in place. To remove the effect of a seismic wavelet, in Chapter 5 we deconvolve the trace and calibrate the result. We have determined that deconvolution leaves a footprint on the spectrum of the reflection coefficient, yielding inconsistent inversion results.

In this Chapter we explore two ideas of inverting anelastic reflectivity. The first is a least-squares approach to AVF inversion. The reasoning behind a least-squares AVF inversion methodology is to obtain a more robust method of satisfying item (2) above. Removing the wavelet from the spectrum of anelastic reflection coefficients, via deconvolution, leaves a footprint which yields inconsistent inversion results. In this chapter, we bring an estimate of the wavelet into the linear AVF inversion equation and find a least-squares solution with the hope of finding consistent AVF inversion results.

In the second part of this chapter we study full waveform inversion (FWI) of anelastic reflectivity. We calculate analytic data for a simple anelastic Earth model consisting of an elastic overburden overlaying a highly anelastic target. The analytic data is one dimensional, normal incidence and is used to calculate the first step of the gradient function for FWI. We then interpret the gradient to draw insight into how FWI will reconstruct the proper model.

7.2 Least-squares AVF inversion

7.2.1 Introduction

In Chapter 5 we explore the effects that a wavelet, random noise, and proximal seismic events will have on the spectrum of a target absorptive reflection coefficient. Recommendations for implementing AVF inversion in the presence of these effects are made but we find inconsistent inversion accuracy. It is because of this that we develop a method here of casting the AVF inverse problem as a least-squares minimization problem. The opportunity for optimization and regularization offered by a least-squares approach may bring stability to the output of AVF inversion in the presence of wavelet, noise, proximal events, etc. We develop the following methodologies of least-squares AVF inversion in the following environments:

1. at normal incidence and no wavelet,

2. at oblique incidence,

3. with source wavelet intact,

4. using the FST spectra as input.

The angle dependence of reflection coefficients is studied in the least-squares framework. The effect of the wavelet is taken into account by utilizing the estimate of the wavelet in the linear AVF inversion equation as opposed to deconvolving the trace prior to implementation of AVF inversion. This approach of utilizing the wavelet estimate in the least-squares algorithm may also help stabilize the AVF inversion result. Finally, we use output from a fast S-transform (FST) (for details, see Brown et al. (2010) and Chapter 2) as input into our least-squares AVF approach and test using numerically modeled data.

7.2.2 Normal incidence, source wavelet removed

We start with the expression for the linearized anelastic reflection coefficient for an elastic overburden overlaying a highly attenuative target given by (for derivation see Chapter 2 or Innanen, 2011)

$$R(\omega) \approx -\frac{1}{2} a_Q F(\omega) + \frac{1}{4} a_C, \tag{7.1}$$

where the reflection coefficient, $R(\omega)$, is complex and a function of frequency and a_Q and a_C are the perturbation parameters in Q and acoustic seismic velocity respectively and $F(\omega) = \frac{i}{2} - \frac{1}{\pi} log(\omega/\omega_r)$. The AVF inverse problem is to determine a_Q and a_C from measurements of $R(\omega)$. By differencing the reflection coefficient across frequencies the perturbation in Q can be solved for (Innanen, 2011). In Chapter 5 we discuss AVF inversion on a target anelastic reflection coefficient in the presence of a wavelet, random noise, and numerous proximal events. We found that the inversion accuracy can be

adversely affected by these phenomena. For this reason, we cast the AVF inverse problem in a least-squares formalism in order to stabilize the results of AVF inversion. Beginning with equation (7.1) we can treat N instances of $R(\omega)$ and re-write in matrix form,

$$\begin{pmatrix} R(\omega_1) \\ R(\omega_2) \\ \vdots \\ R(\omega_N) \end{pmatrix} = \begin{pmatrix} \frac{1}{4} & -\frac{1}{2}\mathrm{F}(\omega_1) \\ \frac{1}{4} & -\frac{1}{2}\mathrm{F}(\omega_2) \\ \vdots & \vdots \\ \frac{1}{4} & -\frac{1}{2}\mathrm{F}(\omega_N) \end{pmatrix} \begin{pmatrix} a_C \\ a_Q \end{pmatrix} \tag{7.2}$$

Equation (7.2) highlights the fact that, given $R(\omega)$ at more than two frequencies, solving for a_C and a_Q is an overdetermined problem. To cast the problem as a least-squares minimization problem we can view equation (7.2) in the form

$$\mathbf{d}=\mathbf{G}\mathbf{m}, \tag{7.3}$$

where the data vector $\mathbf{d}$ is $R(\omega)$, $\mathbf{G}$ is the operator and the model vector $\mathbf{m}$ is a_C and a_Q. Least-squares minimizing the error between $\mathbf{d}$ and $\mathbf{G}\mathbf{m}$ and solving for $\mathbf{m}$ yields

$$\mathbf{m} = (\mathbf{G}^H\mathbf{G})^{-1}\mathbf{G}^H\mathbf{d}. \tag{7.4}$$

Here H is the Hermitian transpose. We could modify this least-squares approach to AVF inversion to include weights, a model objective, etc. To test the effectiveness of this approach we model anelastic reflection coefficients and invert using equation (7.4). The modeling is performed for an impulsive plane wave incident upon a planar boundary separating an elastic overburden with a highly anelastic target (such as illustrated in Figure 4.1). Target Q is varied from 10 to 105. The spectra of the traces are then obtained using an FFT and equation (7.4) is implemented to solve for a_C and a_Q for each of these traces. In Figure 7.1(a) we see an example trace in which Q of the target is 40, and in Figure 7.1(b) is the spectrum of this anelastic reflection coefficient. Consider Figure 7.2 and Figure 7.3, the accuracy of the inversion of a_C and a_Q is shown. Notice

in Figure 7.3 that the inversion for a_Q fails at low Q values. This is to be expected since we linearized the expression for the anelastic reflection coefficient by assuming small a_Q (for example, see Chapter 2, or Innanen, 2011).

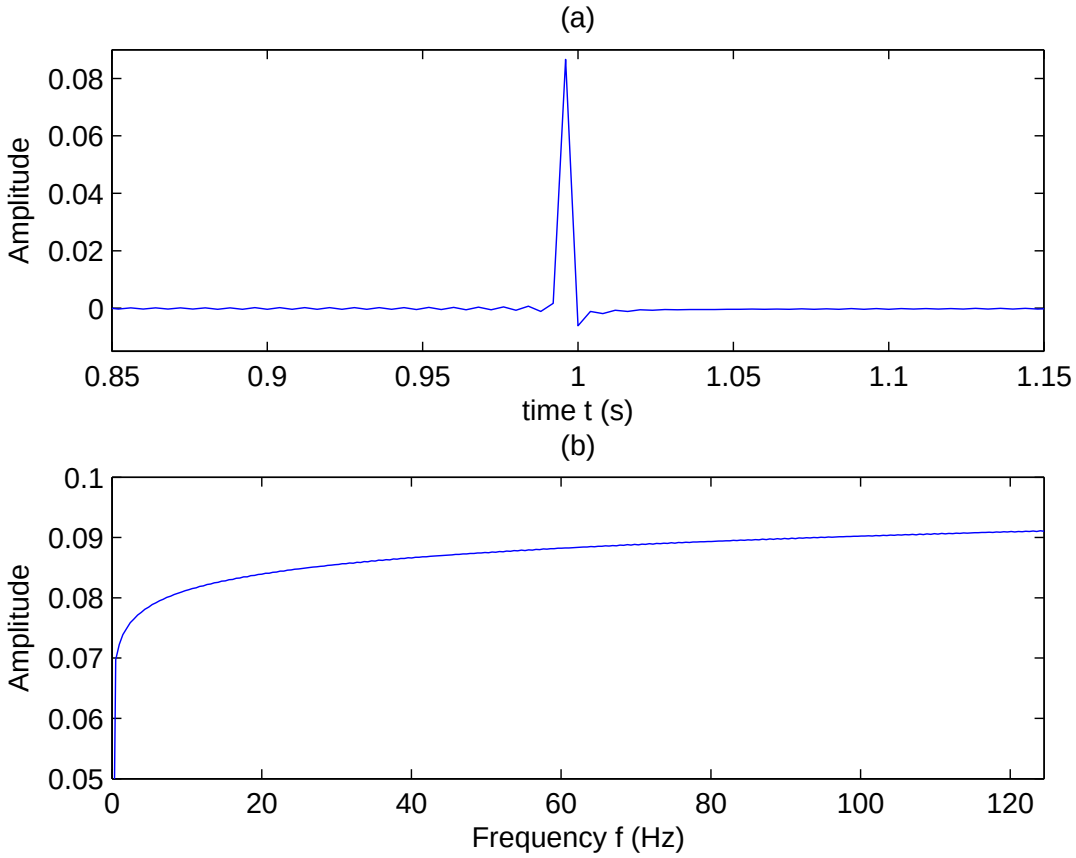

Figure 7.1: (a) A synthetic seismic trace with a single anelastic reflection and no source wavelet. Q of the target is 40. (b) Amplitude spectrum of the anelastic reflection coefficient in (a). $c_0 = 1500m/s$, $c_1 = 1800m/s$, $Q_1 = 40$.

7.2.3 Oblique incidence, source wavelet intact

In Chapters 4-5 we have investigated the inversion of AVF data at normal incidence, either testing with no wavelet, or deconvolving the wavelet by designing the deconvolution filter away from the reflection of interest. In practise, we may have access to an estimate of

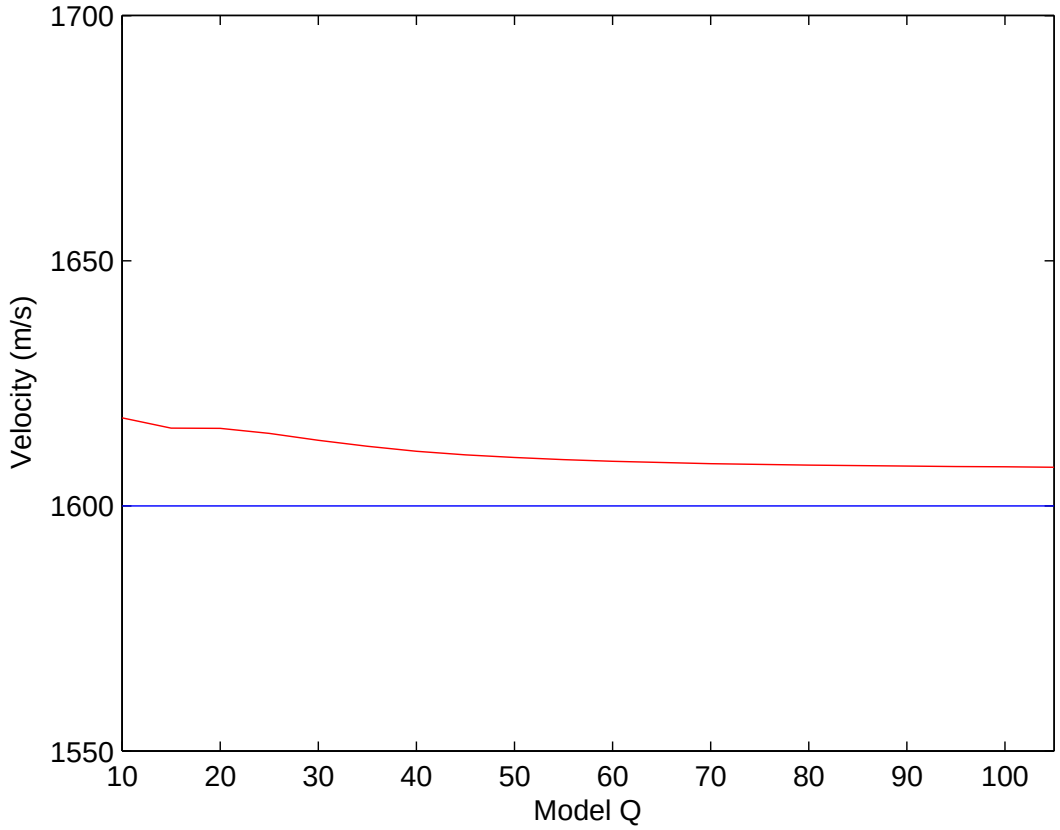

Figure 7.2: Comparison of the inversion of target velocity (red) and the actual target velocity (blue) vs. the Q used in the modeling.

the wavelet, and our data will not be restricted to normal incidence. In this section we extend the inversion framework to accommodate a wavelet estimate and plane wave data at oblique incidence.

Oblique incidence

We first extend the normal incidence formula in equation (7.1) to oblique incidence (for derivation, see Innanen, 2011) given by the expression

$$R(\omega,\theta) = \left(-\frac{1}{2}a_Q F(\omega) + \frac{1}{4}a_C\right)\left(1+\sin^2\theta\right). \tag{7.5}$$

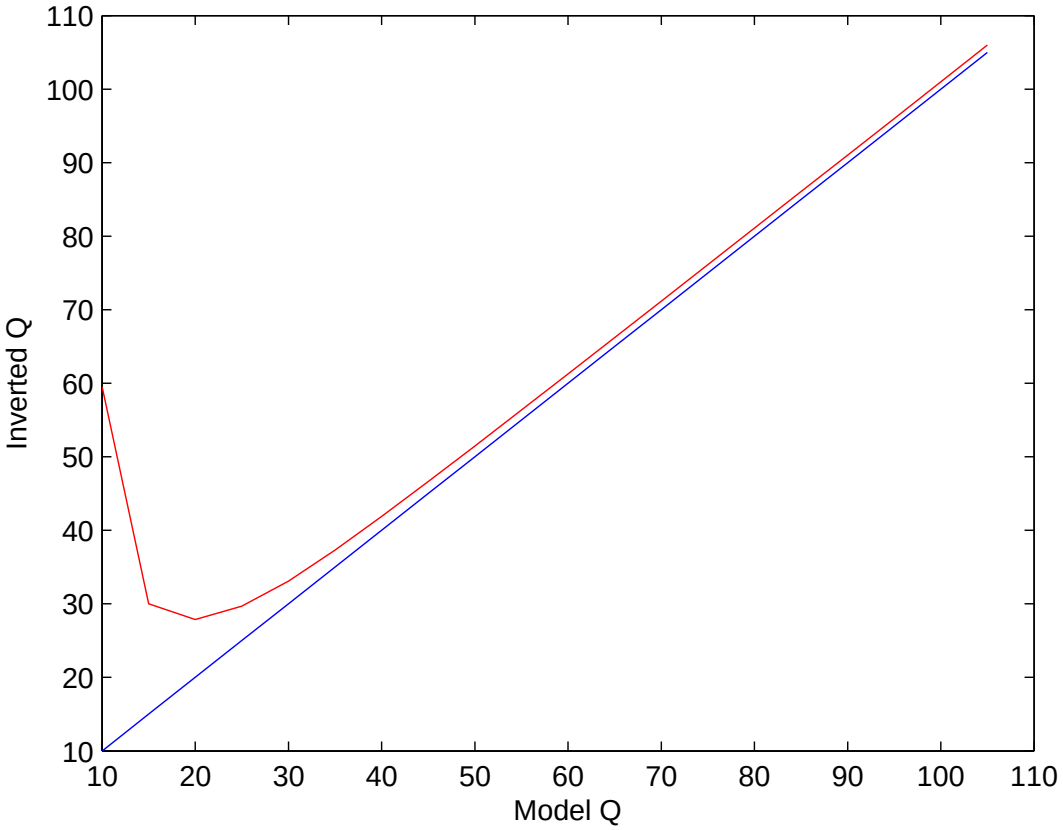

Figure 7.3: Comparison of the inversion of target Q (red) and the actual target Q (blue). Notice the inversion fails at low Q. This is due to linearization error.

Here θ is the angle of incidence and $R(\omega, \theta)$ is the linearized, frequency dependent and angle dependent reflection coefficient. In the same way as equation (7.1) is cast in a least-squares framework so too is equation (7.5). We start by rewriting equation (7.5), for a given angle of incidence θ_m as

$$\begin{pmatrix} R(\omega_1, \theta_m) \\ R(\omega_2, \theta_m) \\ \vdots \\ R(\omega_N, \theta_m) \end{pmatrix} = \begin{pmatrix} \frac{1}{4}\left(1 + \sin^2\theta_m\right) & -\frac{1}{2}\mathrm{F}(\omega_1)\left(1 + \sin^2\theta_m\right) \\ \frac{1}{4}\left(1 + \sin^2\theta_m\right) & -\frac{1}{2}\mathrm{F}(\omega_2)\left(1 + \sin^2\theta_m\right) \\ \vdots & \vdots \\ \frac{1}{4}\left(1 + \sin^2\theta_m\right) & -\frac{1}{2}\mathrm{F}(\omega_N)\left(1 + \sin^2\theta_m\right) \end{pmatrix} \begin{pmatrix} a_C \\ a_Q \end{pmatrix}. \tag{7.6}$$

With equation 7.6 we may find the least-squares solution for a_C and a_Q. As we are moving away from our simple normal incidence model by considering oblique incidence reflections, we should use a model for reflection coefficients which includes contrasts in density. But as the basic character of the AVF problem is exposed using this simple model we stick to using it for now. Any attempt to apply this least-squares AVF inversion to non-normal incidence field data will need to account for density contrasts. The AVF inversion equations are readily adaptable to include density and so we leave this as a topic of future research.

Source wavelet intact

Consider Figure 7.4, in it we see a seismic trace consisting of an anelastic reflection coefficient convolved with a wavelet (Figure 7.4(a)), and the amplitude spectrum of this synthetic trace (7.4(b)). If we knew the wavelet we could simply remove its spectrum from the trace to obtain the amplitude spectrum of the anelastic reflection coefficient by itself (Figure 7.4(c)). In Chapter 5 we attempt to remove the source wavelet from the trace by performing standard Weiner deconvolution on the trace. However, we find that deconvolution imposes a footprint on the amplitude spectra of the anelastic reflection coefficients, adversely affecting inversion accuracy. A more robust method of accounting for the source wavelet may be found if we bring an estimate of the wavelet into the linear AVF equation and find a least-squares solution. In order to include a source wavelet in AVF theory, we need only multiply the reflection coefficient with the wavelet in the frequency domain. We can use the Wiener deconvolution to obtain an estimate of the wavelet to be used in inversion. Since equation (7.1) and equation (7.5) are already in

the frequency domain, we can simply re-write equation (7.5) as

$$R'(\omega,\theta) = R(\omega,\theta)S(\omega) = \left(-\frac{1}{2}a_Q F(\omega) + \frac{1}{4}a_C\right)\left(1+\sin^2\theta\right)S(\omega). \tag{7.7}$$

Here $S(\omega)$ is the spectrum of the source wavelet and $R'(\omega,\theta)$ is reflection coefficient multiplied by the source wavelet. $R'(\omega,\theta)$ will be contained in the data vector $\mathbf{d}$ in equation (7.3). To cast equation (7.7) as a least-squares inverse problem we first re-write for a given angle of incidence, θ_m, as

$$\begin{pmatrix} R'(\omega_1,\theta_m) \\ R'(\omega_2,\theta_m) \\ \vdots \\ R'(\omega_N,\theta_m) \end{pmatrix} = \begin{pmatrix} \frac{1}{4}\left(1+\sin^2\theta_m\right)S(\omega_1) & -\frac{1}{2}F(\omega_1)\left(1+\sin^2\theta_m\right)S(\omega_1) \\ \frac{1}{4}\left(1+\sin^2\theta_m\right)S(\omega_2) & -\frac{1}{2}F(\omega_2)\left(1+\sin^2\theta_m\right)S(\omega_2) \\ \vdots & \vdots \\ \frac{1}{4}\left(1+\sin^2\theta_m\right)S(\omega_N) & -\frac{1}{2}F(\omega_N)\left(1+\sin^2\theta_m\right)S(\omega_N) \end{pmatrix} \begin{pmatrix} a_C \\ a_Q \end{pmatrix}. \tag{7.8}$$

Now we let

$$\mathbf{d} = \begin{pmatrix} R'(\omega_1,\theta_m) \\ R'(\omega_2,\theta_m) \\ \vdots \\ R'(\omega_N,\theta_m) \end{pmatrix}, \tag{7.9}$$

and

$$\mathbf{G} = \begin{pmatrix} \frac{1}{4}\left(1+\sin^2\theta_m\right)S(\omega_1) & -\frac{1}{2}F(\omega_1)\left(1+\sin^2\theta_m\right)S(\omega_1) \\ \frac{1}{4}\left(1+\sin^2\theta_m\right)S(\omega_2) & -\frac{1}{2}F(\omega_2)\left(1+\sin^2\theta_m\right)S(\omega_2) \\ \vdots & \vdots \\ \frac{1}{4}\left(1+\sin^2\theta_m\right)S(\omega_N) & -\frac{1}{2}F(\omega_N)\left(1+\sin^2\theta_m\right)S(\omega_N) \end{pmatrix}, \tag{7.10}$$

and finally

$$\mathbf{m} = \begin{pmatrix} a_C \\ a_Q \end{pmatrix}, \tag{7.11}$$

which allows us to write the least-squares solution for $\mathbf{m}$ as

$$\mathbf{m} = (\mathbf{G}^H\mathbf{G})^{-1}\mathbf{G}^H\mathbf{d}. \tag{7.12}$$

7.2.4 Synthetic examples

To test this least-squares AVF inversion framework, angle dependent reflection coefficients are calculated and a minimum phase wavelet is convolved with the reflection coefficients, such as shown in Figure 7.4(a). A standard Weiner deconvolution code from the CREWES matlab toolbox is used to obtain an estimate of the wavelet to be used in equation (7.8). Figure 7.5 shows the inversion result for the wavespeed, the red line corresponds to the inversion result and the black line is the actual wavespeed. The inversion fails at high angles of incidence (greater than 40 degrees). This is due to the fact that equation (7.5) is a linearized expression obtained by expanding around small $\sin^2\theta$. Figure 7.6 shows the inversion result for Q in red and the actual Q in black, again the failure of the inversion at high angles of incidence is due to the linearization error. Figure 7.5 and Figure 7.6 show that this least-squares approach has the ability to invert for the wavespeed and Q of the target for angles of incidence up to about 40 degrees. This is a promising result as it shows that an estimate of the wavelet using standard deconvolution codes can be implemented with the AVF inverse equation to obtain reliable estimates of target Q.

7.3 Least-squares AVF inversion using the fast S-transform

The goal of developing this least-squares approach for solving the AVF inverse problem is to stabilize the inversion results in the presence of a source wavelet. In Chapter 5 we saw that the inversion results on deconvolved data are inconsistent due to the footprint that deconvolution imposes on the spectrum of the reflection coefficient. We have now seen that the source wavelet can be brought into the equation for dispersive reflection coefficients and then a_C and a_Q can be solved for in a least-squares sense. However, in order for this to be useful to us, we must be able to implement least-squares AVF

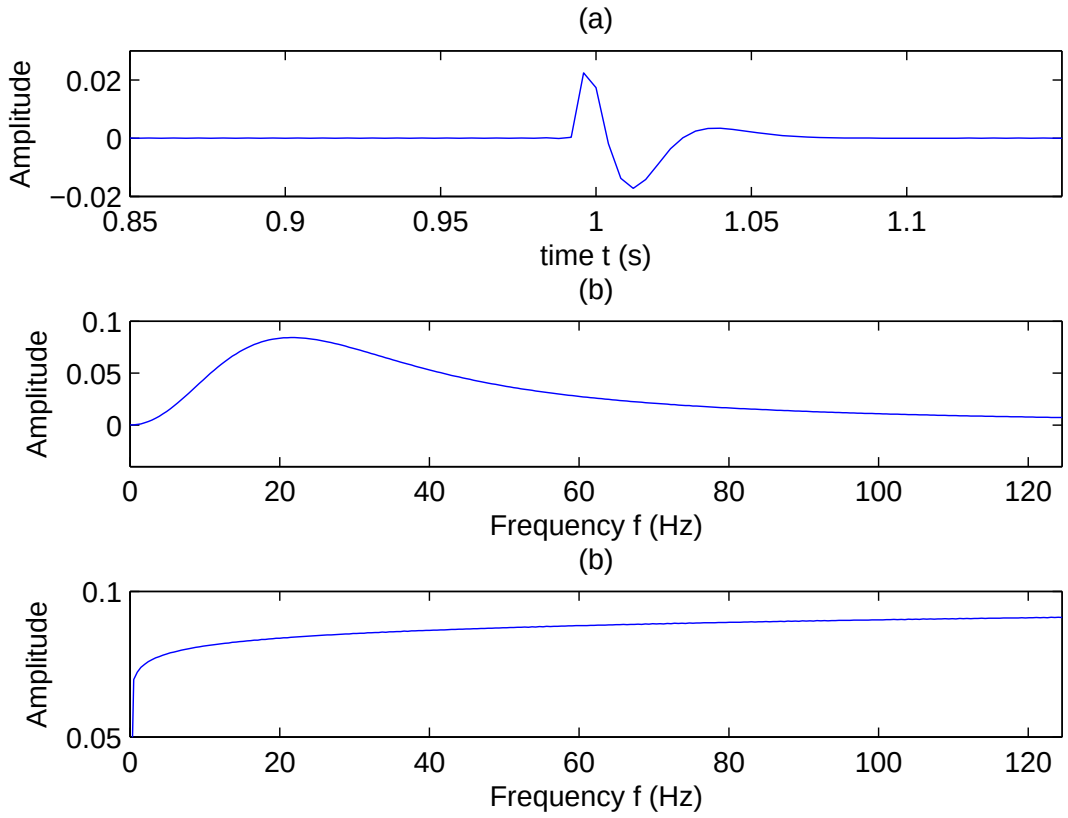

Figure 7.4: In (a) An anelastic reflection coefficient convolved with a wavelet. (b) The amplitude spectrum of reflection in (a). In (c) the spectrum of the anelastic reflection coefficient alone.

inversion using estimates of the spectra of reflection events from the FST. In order to modify the least-squares approach to accept input from the FST recall that the FST calculates averages of the local spectra over frequency bands. First consider the wavelet free case. The S-domain amplitudes of the reflection coefficient are given by

$$\tilde{R}_j = \frac{\sum_{i=j_s}^{j_e} R(\omega_i)}{(j_e - j_s + 1)}, \tag{7.13}$$

where $\tilde{R}_j$ is the average of $R(\omega)$ over the j_{th} FST frquency band which spans the continuous spectrum from sample j_s to j_e. We similarly define $\tilde{F}_j$ as the average of $F(\omega)$ over

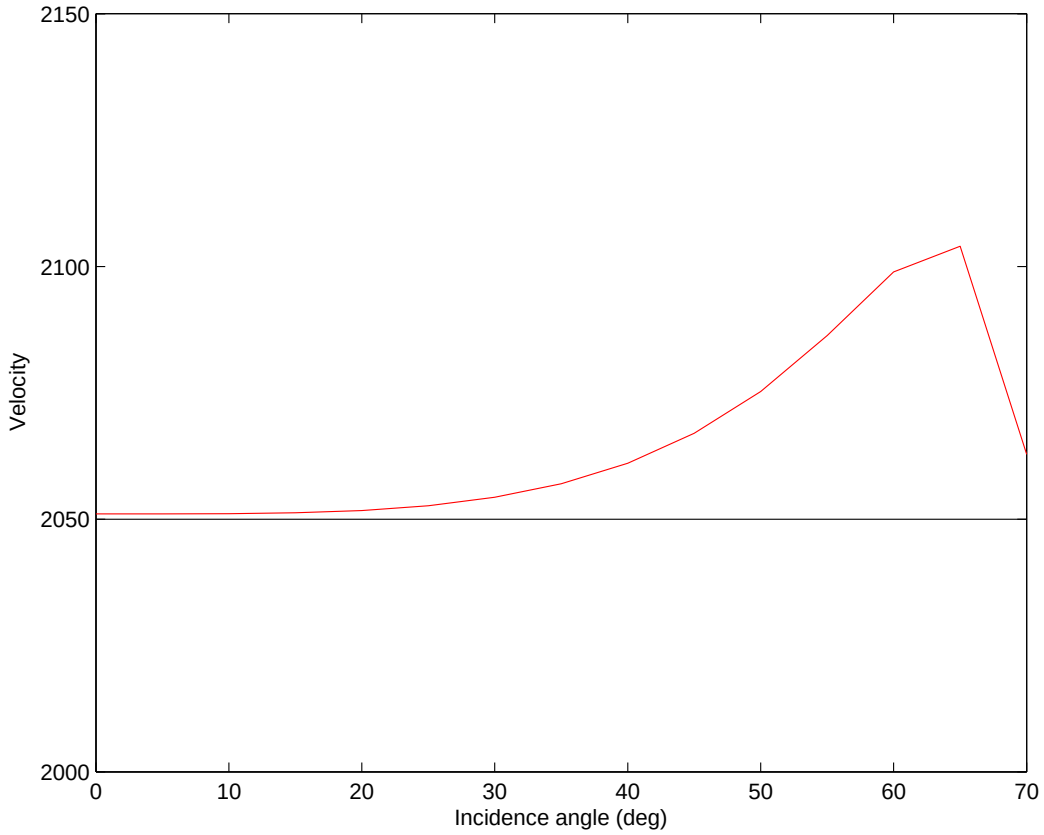

Figure 7.5: Comparison of the inverted target velocity (red) and the actual target velocity (black) vs. incidence angle. Notice the inversion fails at high angles of incidence. This is due to linearization error.

the same band

$$\tilde{F}_j = \frac{\sum_{i=j_s}^{j_e} F(\omega_i)}{(j_e - j_s + 1)}. \tag{7.14}$$

Now equation (7.1) can be re-written to take input from the FST as follows

$$\tilde{R}_j \approx \left(-\frac{1}{2} a_Q \tilde{F}_j + \frac{1}{4} a_C \right), \tag{7.15}$$

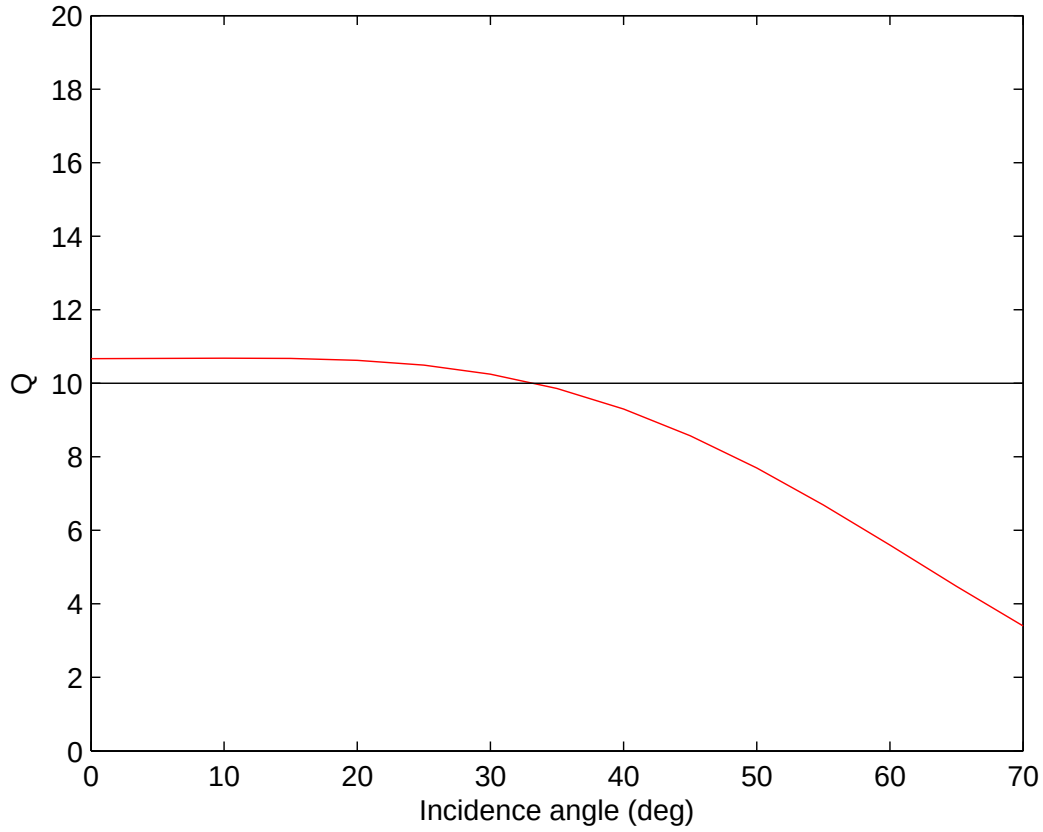

Figure 7.6: Comparison of the inversion of target Q (red) and the actual target Q (black) vs. incidence angle. Notice the inversion fails at high angles of incidence. This is due to linearization error.

if there are M bands in the S-domain, equation 7.15 can be re-written in matrix form as

$$\begin{pmatrix} \tilde{R}_1 \\ \tilde{R}_2 \\ \vdots \\ \tilde{R_M} \end{pmatrix} = \begin{pmatrix} \frac{1}{4} & -\frac{1}{2}\tilde{F}_1 \\ \frac{1}{4} & -\frac{1}{2}\tilde{F}_2 \\ \vdots & \vdots \\ \frac{1}{4} & -\frac{1}{2}\tilde{F_M} \end{pmatrix} \begin{pmatrix} a_C \\ a_Q \end{pmatrix}. \tag{7.16}$$

We may invert equation (7.16) for a_C and a_Q by finding the least-squares solution. We test AVF inversion accuracy on synthetic data with input from the FST. Anelastic reflections are modeled at normal incidence and with no wavelet. The FST is used to estimate the

local spectrum of the anelastic reflection coefficient and the least-squares approach is used to invert for velocity and Q of the target. The experiment is repeated for a range of Q values, while the pertrubation is kept small, and the results are shown in Figure 7.7 and 7.8. In these figures the actual target parameters are shown in blue and the inverted target parameters are shown in red. The black curve in Figure 7.8 represents the inversion result using the analytic spectrum (i.e. the inversion result using equation (7.2)). The inversion for velocity is accurate and the inversion for Q is accurate except at low Q. We see the inversion result fails using analytic spectra as well. The failure of the inversion at low Q is due to linearization error and our choice of ω_r.

Now consider the case where the reflection coefficient is convolved with a source wavelet: define S_M as the average of the amplitude spectrum of the source wavelet $S(\omega)$ from sample j_s to j_e

$$\tilde{S}_j = \frac{\sum_{i=j_s}^{j_e} S(\omega_i)}{(j_e - j_s + 1)}. \tag{7.17}$$

We re-write equation 7.7 (at normal incidence) to take input from the FST in the presence of a source wavelet

$$\tilde{Rs}_j = \tilde{R}_j \tilde{S}_j = \left(-\frac{1}{2} a_Q \tilde{F}_j \tilde{S}_j + \frac{1}{4} a_C \tilde{S}_j \right). \tag{7.18}$$

Here $\tilde{Rs}$ is the FST spectrum of the reflection coefficient convolved with the wavelet. We may invert for a_C and a_Q by finding the least-squares solution. Once again, we test AVF inversion accuracy on synthetic data with the source wavelet intact. We obtain an estimate of the wavelet using Weiner deconvolution codes. We then use the FST to obtain $\tilde{Rs}$ and then invert for velocity and Q of the target. The experiment is repeated for a range of Q values and the results are shown in Figure 7.9 and 7.10. Notice that the velocity inversion is accurate but the inversion for Q fails. It is unclear to us why the least-squares inversion for Q breaks down in the presence of a wavelet when the FST is used to estimate the input spectra.

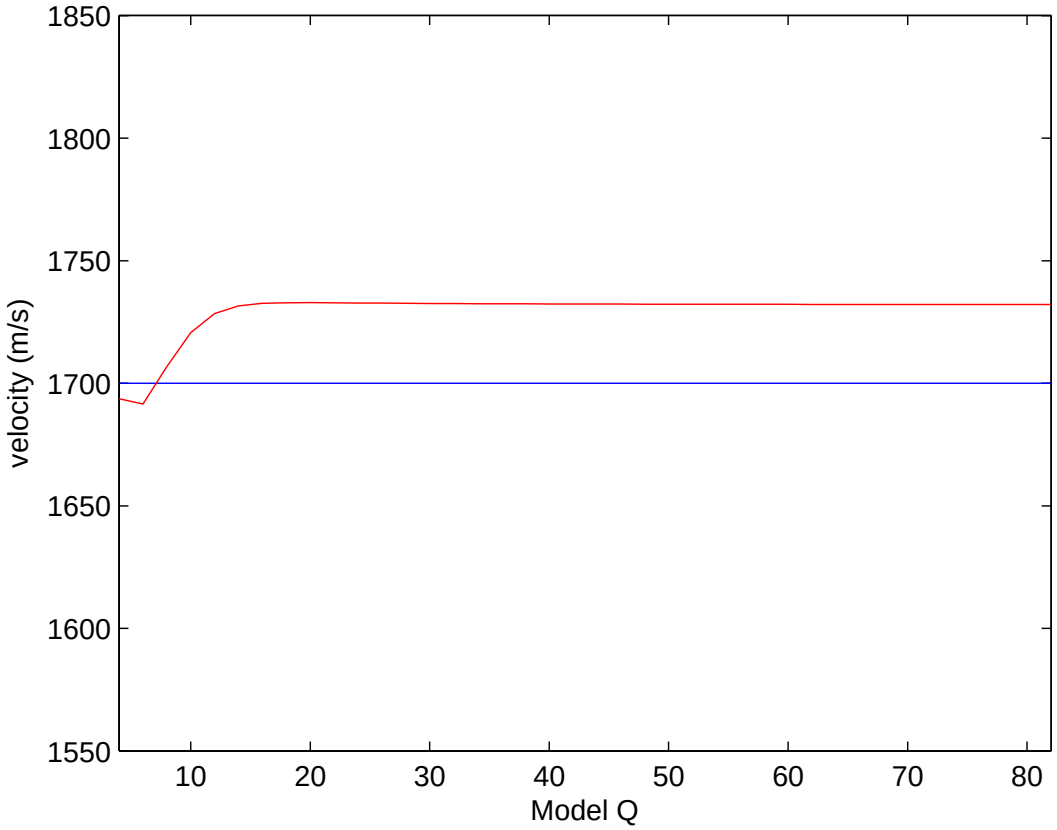

Figure 7.7: Comparison of the inversion of target velocity (red) and the actual target velocity (blue) using the FST to estimate the spectrum of the reflection coefficient. a_C is kept small.

7.4 Full waveform inversion of anelastic reflectivity

7.4.1 Introduction

Full waveform inversion (FWI) is taking on an increasingly important role in seismic exploration. As this role grows, we must develop (1) implementations and algorithms, and (2) our understanding of the basic nature of FWI. In this chapter we are concerned with the second of these issues. Particular issues associated with inversion of anelastic media have been discussed by Hicks and Pratt (2001) and Malinowski et al. (2011). Here

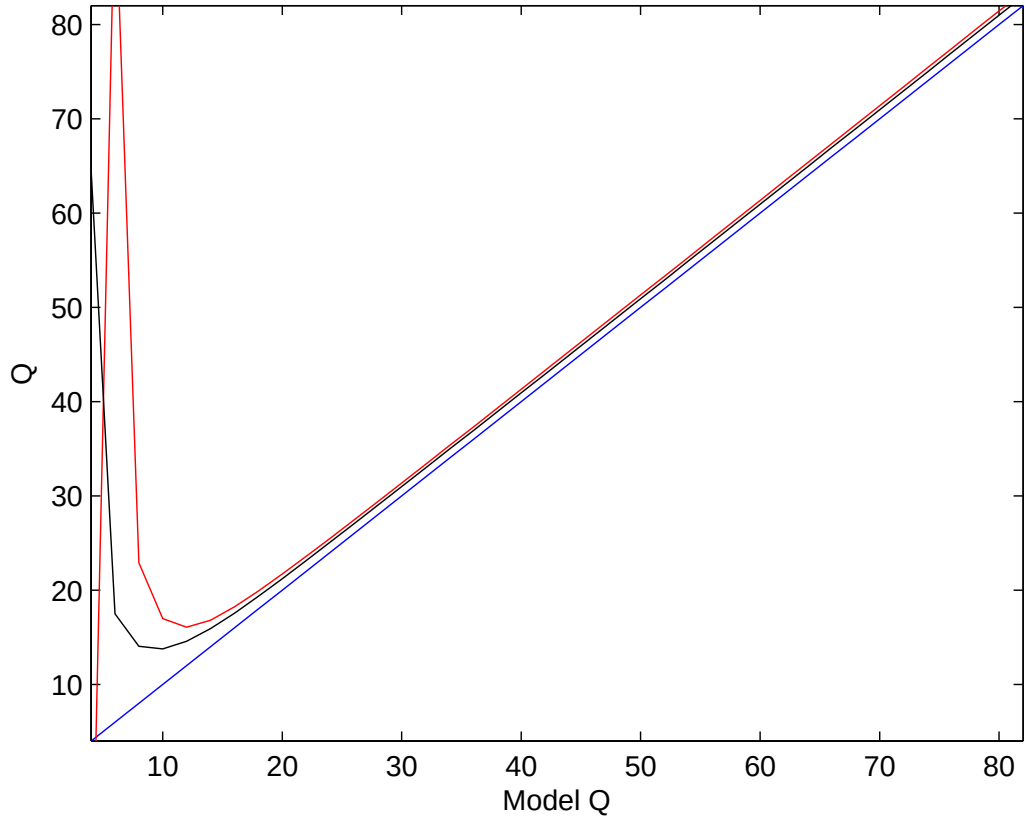

Figure 7.8: Comparison of the inversion of target Q using the FST spectrum (red) and using the analytic spectrum (black). The actual target Q is shown in blue. a_C is kept small.

we add to these discussions by developing an analytic example of the first iteration of anelastic FWI. The first gradient of full waveform inversion is calculated for analytic data of a very simple attenuating Earth model. This simple Earth model consists of an elastic overburden overlaying an attenuative target with the interface between the layers occurring at a depth of 300m. The source and receiver are colocated at the surface and so the analytic data calculated is one dimensional and normal incidence. The analytic data for this simple model is used to calculate the first step of the gradient function for full waveform inversion. The gradient is analyzed and we attempt to draw insight into

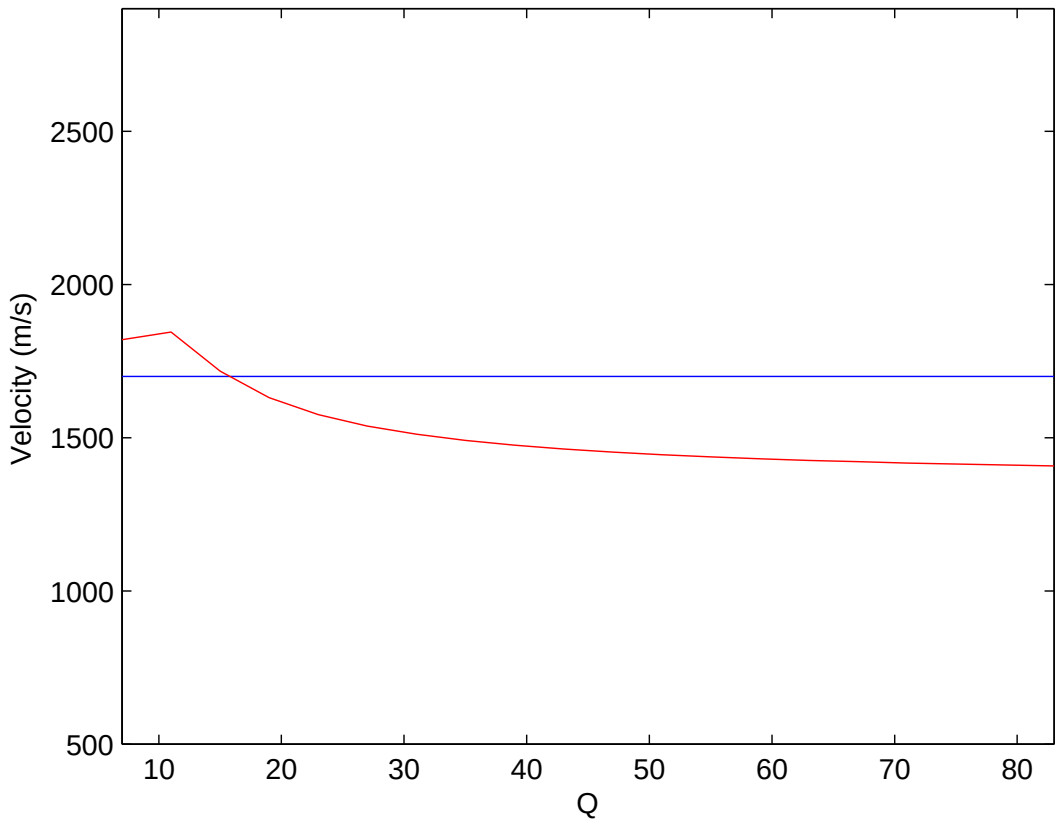

Figure 7.9: Comparison of the inversion of target velocity (red) and the actual target velocity (blue) using the FST to estimate the spectrum of the reflection in the presence of a source wavelet.

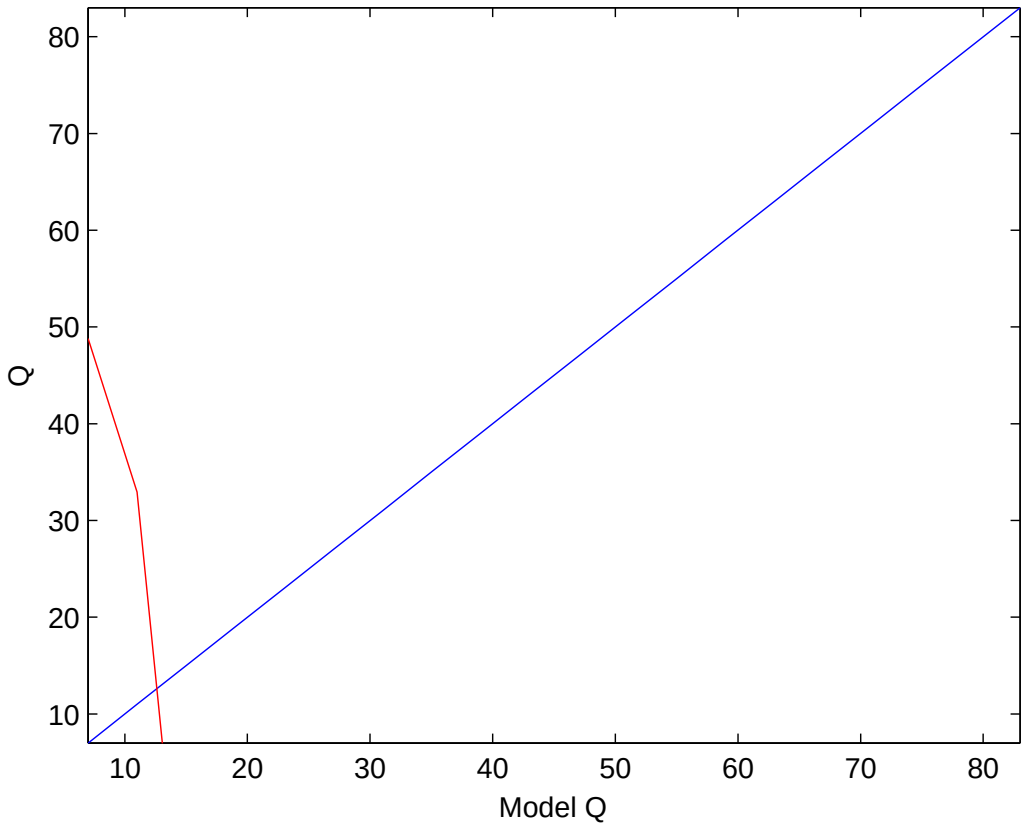

Figure 7.10: Comparison of the inversion of target Q (red) and the actual target Q (blue) using the FST to estimate the spectrum of the reflection in the presence of a source wavelet. The inversion for Q fails.

how full waveform inversion will reconstruct the proper model in this setting.

7.4.2 Analytic data and initial model

In this example the actual medium is a two layer model in which both layers have velocity c_0. There is a contrast in Q, however, as the first layer is elastic and the second layer is anelastic with a Q value of 40. Therefore there is a single primary in the data. We define the perturbations in wavespeed (a_C) and Q (a_Q) as

$$a_C = 1 - \frac{c_0^2}{c_1^2}$$
$$a_Q = \frac{1}{Q}$$

Figure 7.11(a) shows the simple attenuating Earth model. The blue line in Figure 7.11 corresponds to the perturbation in velocity, a_C, and the red line corresponds to the perturbation in Q, a_Q. Notice that since there is no contrast in the acoustic properties of the medium and so the profile of a_C is constant at zero. However, the profile of a_Q jumps at $300m$, which corresponds to the contrast in Q at that depth. Also, the starting model to be used in the calculation of the gradient is that of a homogeneous acoustic model with velocity c_0, which is shown in Figure 7.11(b). For a source and receiver colocated at the surface the analytic, one-dimensional normal incidence data for this Earth model can be written as

$$D(\omega) = \frac{1}{i2k_0} + R(\omega)\frac{e^{i2k_0 z_1}}{i2k_0},$$

where $k_0 = \frac{\omega}{c_0}$, z_1 is the depth to the reflector and since there is no acoustic impedance contrast, the reflection coefficient is given approximately by (Innanen, 2011)

$$\begin{aligned} R(\omega) &\approx -\frac{1}{2}a_Q F(\omega) \\ &\approx -\frac{1}{2}a_Q\left(\tfrac{i}{2} - \frac{1}{\pi}\log(\omega/\omega_r)\right) \end{aligned}$$

7.4.3 Full waveform inversion of analytic data

A well-known result of the theory of FWI is that the gradient is given by the equation (Tarantola, 1984; Pratt, 1999; Margrave et al., 2010)

$$g(z) = \int_{-\infty}^{\infty} d\omega \omega^2 G(0,z,\omega) G(z,0,\omega) \delta P^*(0,0,\omega) \tag{7.19}$$

where $g(z)$ is the first step of the gradient, $G(0,z,\omega)$ is the Green's function for a wave traveling from source position $z_s = 0$ to depth z and $G(z,0,\omega)$ is the Green's function for a wave traveling from source position $z_s = z$ to a receiver at $z = 0$. $\delta P^*(0,0,\omega)$ is the complex conjugate of the data residuals. In order to calculate the data residuals, we need another Green's function, $G(0,0,\omega)$ which is the analytic data we obtain from our initial model. The needed Greens functions can be written as

$$\begin{aligned} G(0,0,\omega) &= \frac{1}{i2k_0}, \\ G(z,0,\omega) &= \frac{e^{ik_0 z}}{i2k_0}, \\ G(0,z,\omega) &= \frac{e^{ik_0 z}}{i2k_0}. \end{aligned}$$

We can therefore write the data residuals as

$$\delta P(0,0,\omega) = D(\omega) - G(0,0,\omega) = R(\omega)\frac{e^{i2k_0 z_1}}{i2k_0},$$

taking the complex conjugate we obtain

$$\delta P^*(0,0,\omega) = -\frac{1}{2} a_Q \left(\frac{i}{2} + \frac{1}{\pi} \log(\omega/\omega_r) \right) \frac{e^{-i2k_0 z_1}}{i2k_0},$$

now we can calculate the gradient

$$\begin{aligned} g(z) &= \int_{-\infty}^{\infty} d\omega \omega^2 G(0,z,\omega) G(z,0,\omega) \delta P^*(0,0,\omega) \\ &= \int_{-\infty}^{\infty} d\omega \omega^2 \left[\frac{e^{ik_0 z}}{i2k_0}\right]^2 \left[-\frac{1}{2} a_Q \left(\frac{i}{2} + \frac{1}{\pi}\log(\omega/\omega_r)\right) \frac{e^{-i2k_0 z_1}}{i2k_0}\right] \\ &= \frac{c_0^2}{4} \int_{-\infty}^{\infty} d\omega \frac{e^{i2k_0(z-z_1)}}{i2k_0} \left[\frac{i}{4} a_Q + a_Q \frac{\log(\omega/\omega_r)}{2\pi}\right] \\ &= \frac{ic_0^3}{32} a_Q \int_{-\infty}^{\infty} d(2k_0) \frac{e^{i2k_0(z-z_1)}}{i2k_0} + \frac{c_0^2}{8\pi} a_Q \int_{-\infty}^{\infty} d\omega \frac{e^{i2k_0(z-z_1)}}{i2k_0} \log(\omega/\omega_r) \\ &= \frac{ic_0^3}{32} a_Q H(z-z_1) + \frac{c_0^2}{8\pi} a_Q \int_{-\infty}^{\infty} d\omega \frac{e^{i2k_0(z-z_1)}}{i2k_0} \log(\omega/\omega_r) \\ &= g_1 + g_2 \end{aligned} \tag{7.20}$$

where $H(z-z_1)$ is a Heaviside function. The first term in the gradient, g_1, is a step function which turns on at the depth of the reflector z_1, but notice that there is a complex i in front of the Heaviside and therefore the step is wholly imaginary. This seems intuitively correct as we know that in order to model attenuation we let wavenumber or velocity have an imaginary component. Also, the second term, g_2, contains an $\frac{e^{i2k_0(z-z_1)}}{i2k_0}$, which when integrated alone would produce a Heaviside function which steps at the appropriate depth of the reflector, z_1. However, there is a $\log(\omega/\omega_r)$ also contained in the integral which acts as filter and hence performing the integral should yield a step function which has been in some way filtered. The integral g_2 was evaluated numerically. Figure 7.11(c) shows the wholly imaginary step function g_1 vs depth. Figure 7.11(d) shows the absolute value of g_2, it also has a step at z_1. However, it is not a sharp step but rather has a droopy like appearance. This is due to the filtering that the $\log(\omega/\omega_r)$ performs on the step function.

7.4.4 An alternative approach

The equation defining the gradient(equation (7.19)) is obtained by minimizing the objective function (Innanen, 2012)

$$\Phi = \frac{1}{2}\int_{-\infty}^{\infty} d\omega |\delta P^*|^2. \tag{7.21}$$

As we see in equation (7.20), the first calculation of the gradient is complicated by the presence of the $F(\omega)$ in the data residuals δP^*. To obtain a more readily interpretable form for the first step of the gradient we minimize a convenient objective function defined as:

$$\Phi = \frac{1}{2}\int_{-\infty}^{\infty} d\omega \frac{|\delta P^*|^2}{F(\omega)}. \tag{7.22}$$

The equation for the gradient, obtained by minimizing this objective function is given by

$$g(z) = \int_{-\infty}^{\infty} d\omega \frac{\omega^2}{F(\omega)} G(0,z,\omega)G(z,0,\omega)\delta P^*(0,0,\omega). \tag{7.23}$$

An finally, by re-calculating the gradient for our analytic data we obtain

$$g(z) = \frac{c_0^3}{16} a_Q H(z - z_1). \tag{7.24}$$

This gradient is a real Heaviside located at z_1 and proportional to a_Q. This form is more convenient than our previous calculation as the $F(\omega)$ function vanishes. We readily interpret equation 7.24 as predicting a contrast in Q located at the appropriate depth z_1 and being proportional to the perturbation in Q. Of course, our choice of objective function is convenient for a reflection coefficient caused by a contrast in Q only.

7.5 Conclusions

In this chapter, the AVF inverse problem was recast as a least sqaures minimization problem and this least-squares approach was adapted for angle dependent reflections and a seismic wavelet. In Chapter 5 it is shown that AVF inversion is inconsistent in the

presence of noise, numerous reflection events, and a wavelet. The hope of this least-squares approach is to stabilize AVF inversion in the presence of these phenomena. It is shown that for incidence angles up to about 40 degrees reliable estimates of both wavespeed and Q are obtainable, even in the presence of a source wavelet. Further, it is shown that using standard deconvolution codes to obtain an estimate of the wavelet, a reliable inversion result is achieved. Any hope of implementing AVF on seismic field data will require an estimate of the local spectrum of seismic reflections using time-frequency decomposition. We tested this least-squares AVF inversion using the FST estimate of an absorptive reflection coefficient as input. We observe that the inversion results are accurate. However, when we use the FST to estimate the spectra of reflections in the presence of a source wavelet, inversion for Q fails even while the inversion for velocity remains accurate. It is not known why this occurs but it is the subject of future work to resolve this situation.

Also in this chapter, the first step of the gradient for full waveform inversion is calculated on analytic data for a simple Earth model. This simple Earth model consisted of an elastic overburden overlaying an attenuative target. One dimensional, normal incidence data is generated for this model and is used to calculate the first step of the gradient function. We find that the gradient predicted an imaginary step function located at the depth of the attenuative target. This imaginary step function seems to be an intuitively correct result as introducing absorption into the wave equation usually involves allowing the wavespeed to have an imaginary component. Because of dispersion, the real part of the gradient was a step function which is filtered by $\log(\omega/\omega_r)$. The insight we gain is in seeing what the next iterations must accomplish if they are to converge to the correct answer. The imaginary part appears to be moving well towards the right answer, whereas the dispersion and its effect on the real part has left much remaining work to be done to reconstruct the correct result. Since both are here related to the same parameter, we

suggest and will consider as a matter of future research the idea of using the former to help condition the latter. By minimizing a more convenient objective function we obtain a more readily interpretable form for the first gradient.

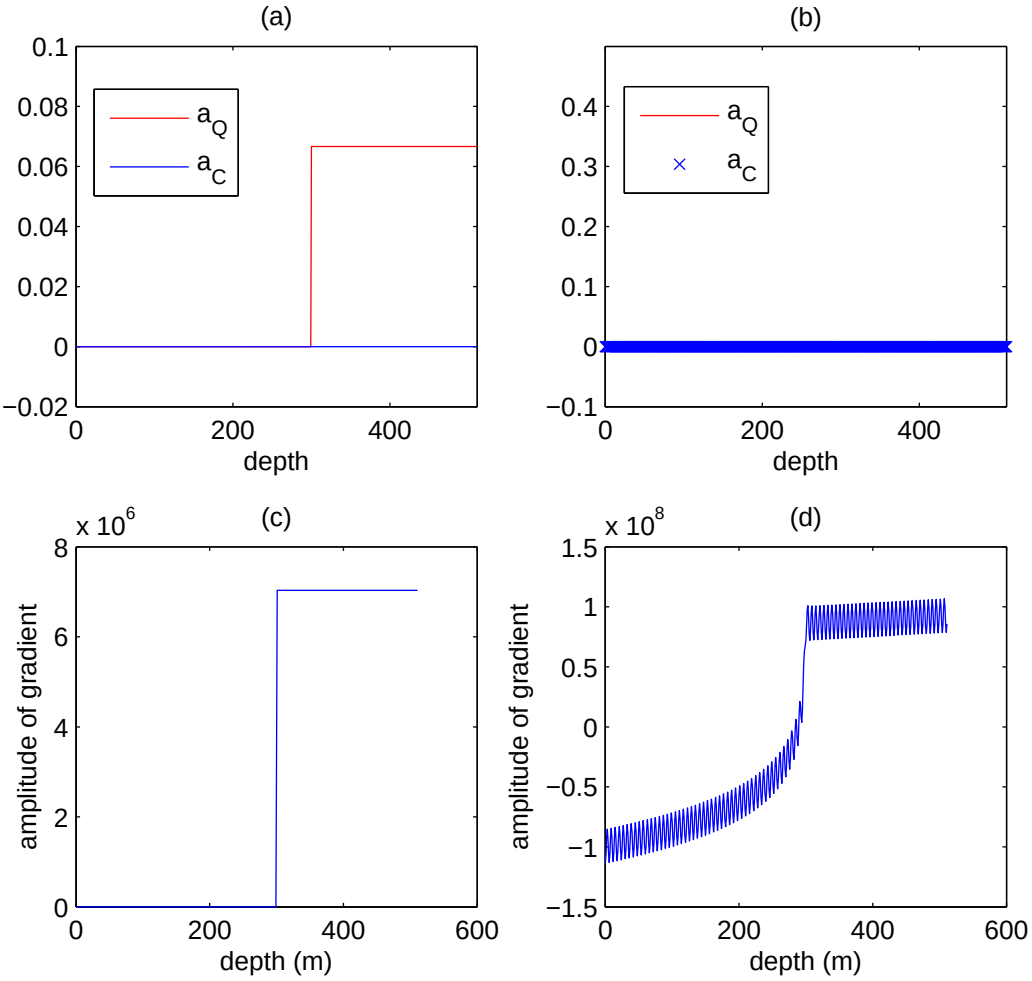

Figure 7.11: In (a) a simple attenuative Earth model consisting of an elastic overburden overlaying an anelastic target. The is a contrast in Q at 300m. In (b) the starting model for FWI is homogeneous and perfectly acoustic. In (c) the imaginary part of the gradient g_1 and in (d) the real part of the gradient g_2.

Chapter 8

Conclusions

The aim of this thesis was to develop a processing workflow for seismic AVF inversion suitable for implementation on field data. To develop this workflow a number of items were needed:

1. A method of time-frequency decomposition which provides high fidelity estimates of the local spectra of seismic reflections

2. The ability to mitigate the adverse effects that random noise, source wavelets, and proximal events has on the spectrum of target reflection coefficients

3. A field data set with a potential AVF reflection

To meet the requirements of item (1) we calibrated a fast S-transform (FST) developed by Brown et al. (2010) (Chapter 3) and we reformulated AVF inversion to be carried out in the S-domain (Chapter 4). To satisfy item (2), in Chapter 5 we examined how random noise, source wavelets, and proximal events influence AVF inversion accuracy and we made recommendations to mitigate these effects. We found a surprising result in our study of nearby/proximal events. We expected that the closer a target reflection is to other events, the more their spectra will interfere. Evidently this is not always the case in the FST domain. We find that in some cases, events farther away may strongly interfere with the spectrum of a target reflection coefficient. This surprising phenomenon should be studied further as it makes it difficult to quantify which portion of a target's spectrum is high fidelity as a function of its proximity to other events.

In Chapter 6 we identified a potential candidate for a measurable anelastic reflection in the Ross Lake VSP data set. We identified and extracted our target reflection (top

of the Mannville) believed to have a possible AVF signature. We also identified and extracted a control reflection (top of Milk River) not believed to be asssociated with a contrast in Q. We were forced to perform additional Q-compensation to account for the attenuation of the primaries in the interval between reflector and receiver. Comparing the spectrum of the target Mannville reflection coefficient with the spectrum of the control Milk River reflection coefficient we observe a similar dispersive character in both. This inconclusive result motivates us to continue to search for another field data set where one of the following are met:

- There is a stronger contrast in Q and therefore more likely to produce a stronger AVF signature; or,

- We need not perform additional Q-compensation either because the overburden is highly elastic or we have wavefield separation techniques we are confident will not alter the local spectra of the primary and direct arrivals.

Deconvolution imposes a footprint on the local spectrum of anelastic reflections which results in inconsistent AVF inversion accuracy. Because of this, in Chapter 7 we re-cast the AVF inversion in a least-squares framework in the hope of producing more robust AVF inversion results in the presence of a wavelet. This methodology has the advantage that we may bring an estimate of the wavelet into the linear AVF equations and then find a least-squares solution for the model parameters a_C and a_Q. We also observe accurate inversion results in the presence of a source wavelet on analytic data. The least-squares formalism also provides a natural framework for AVF inversion of oblique incidence reflections. On analytic data, we observe accurate inversion results on angles of incidence less than 40 degrees.

8.1 Final remark

Future research efforts should be undertaken to increase our ability to detect, quantify, and interpret AVF signatures when they are strong and well isolated, and to detect them when conditions are less than ideal. Of particular importance is that AVF signatures may be most strongly observed at low frequencies, the same part of the bandwidth rendered useless by interference from nearby events. Spectral estimation techniques designed specifically to be used on fractions of cycles may be a fruitful line of future research. However, field examples with strong Q contrasts likely do exist which would be detectable with the methods used in this thesis. It is mostly a matter of finding one.

Bibliography

Aki, Keiiti and Paul G. Richards. *Quantitative Seismology.* 2nd edition. University Science Books, 2002.

Amundsen, Lasse and Rune Mittet. "Estimation of phase velocities and Q-factors from zero-offset, vertical seismic profile data." *Geophysics* 59 (1994): 500–517.

Best, A.I., C. McCann, and J. Sothcott. "The relationships between the velocities, attenuations and petrophysical properties of reservoir sedimentary rocks1." *Geophysical Prospecting* 42 (1994): 151–178.

Bird, Chris, Mostafa Naghizadeh, and Kristopher Innanen. "Amplitude calibration of a fast S-transform." *CREWES Sponsor's Meeting 2010* 22 (2010): 1–12.

Brown, Robert A., M. Louis Lauzon, and Richard Frayne. "A General Description of Linear Time-Frequency Transforms and Formulation of a Fast, Invertible Transform That Samples the Continuous S-Transform Spectrum Nonredundantly." *IEEE Transactions on Signal Processing* 58 (2010): 281–290.

Chapman, M., E. Liu, and X. Y. Li. "The influence of fluid-sensitive dispersion and attenuation on AVO analysis." *Geophysical Journal International* 167 (2006): 89–105.

Dasgupta, Rahul and Roger A. Clark. "Estimation of Q from surface seismic reflection data." *Geophysics* 63 (1998): 2120–2128.

Dietrich, Michel and Michel Bouchon. "Measurements of attenuation from vertical seismic profiles by iterative modeling." *Geophysics* 50 (1985): 931–949.

Du, Jing, Songhui Lin, Weiguo Sun, Shengli Oilfield, and Guochang Liu. "Seismic at-

tenuation estimation using S transform with regularized inversion." *SEG Technical Program Expanded Abstracts* 29 (2010): 2901–2905.

Gibson, Peter C., Michael P. Lamoureux, and Gary F. Margrave. "Letter to the Editor: Stockwell and Wavelet Transforms." 10.1007/s00041-006-6087-9. *Journal of Fourier Analysis and Applications* 12 (2006): 713–721.

Hardage, B. A. *Vertical seismic profiling, Part A: Principles, 2nd Ed.,* in Handbook of geophysical exploration. Ed. S. Treitel K. Helbig. Volume 14A . Geophysical Press, 1985.

Hargreaves, N. D. and A. J. Calvert. "Inverse Q filtering by Fourier transform." *Geophysics* 56 (1991): 519–527.

Hauge, Paul S. "Measurements of attenuation from vertical seismic profiles." *Geophysics* 46 (1981): 1548–1558.

Hicks, G. and G. Pratt. "Reflection waveform inversion using local descent methods: estimating attenuation and velocity over a gas-sand deposit." *Geophysics* 66 (2001): 598–612.

Hinds, R. C., N. L. Anderson, and R. D. Kuzmiski. *VSP Interpretive Processing: Theory and Practice*. Society of Exploration Geophysicists, 1996.

Innanen, Kristopher. "Inversion of the seismic AVF/AVA signatures of highly attenuative targets." *Geophysics* 76 (2011): R1–R14.

Innanen, Kristopher. *Geophysics 673 Course notes*. 2012.

Innanen, Kristopher and J. E. Lira. "Direct non-linear Q-compensation of primaries in layered media: theory and synthetic examples." *SEG Las Vegas 2008 Annual Meeting* (2008): 2957–2962.

Innanen, Kristopher and Jose E. Lira. "Direct nonlinear Q-compensation of seismic primaries reflecting from a stratified, two-parameter absorptive medium." *Geophysics* 75 (2010): V13–V23.

Irving, James D. and Rosemary J. Knight. "Removal of wavelet dispersion from ground-penetrating radar data." *Geophysics* 68 (2003): 960–970.

Kjartansson, Einar. *Attenuation of seismic waves in rocks and applications in energy exploration*. Stanford University, 1979.

Lanning, Eric. N. *Estimating seismic attenuation using VSP measurements*. University Microfilms International, 1985.

Lines., Laurence, C. Sondergeld., K. Innanen., J. Wong., S. Treitel., and T. Ulrych. "Experimental confirmation of "Reflections on Q"." *CREWES Annual Report* 23 (2011).

Lines, Laurence, Fereidoon Vasheghani, and Sven Treitel. "Reflections on Q." *CSEG Recorder* December (2008): 36–38.

Lira, J. E., A. B. Weglein, Chris Bird, and K. A. Innanen. "Determination of reflection coefficients by comparison of direct and reflected VSP events." *CREWES Sponsor's Meeting 2011* 23 (2011): 1–13.

Lira, J. E. M., K. A. Innanen, A. B. Weglein, and A. C. Ramirez. "Correction of primary amplitudes for plane-wave transmission loss through an acoustic or absorptive overburden with the inverse scattering series internal multiple attenuation algorithm: an initial study and 1D numerical examples." *Journal of Seismic Exploration* 19 (2010): SI9–SI14.

Malinowski, M., S. Operto, and A. Ribodetti. "High-resolution seismic attenuation imaging from wide-aperture onshore data by visco-acoustic frequency-domain full-waveform inversion." *Geophysical Journal International* 186 (2011): 1179–1204.

Margrave, G. F. "Theory of nonstationary linear filtering in the Fourier domain with application to time-variant filtering." *Geophysics* 63 (1997): 244.

Margrave, G. F., D. Henley, M. P. Lamoureux, V. Iliescu, and J. Grossman. "Gabor deconvolution revisited." *Proc. 76th Ann. Mtg., Dallas TX.* . Soc. Expl. Geophys., 2003.

Margrave, Gary. F., Robert. J. Ferguson, and Chad. M. Hogan. "Full waveform inversion with wave equation migration and well control." *CREWES Annual Report* 22 (2010).

Miao, Xiaogui, Dragana Todorovic-Marinic, and Tyler Klatt. "Enhancing seismic insight by spectral decomposition." *SEG Technical Program Expanded Abstracts* 26 (2007): 1437–1441.

Naghizadeh, Mostafa and Kristopher Innanen. "Fast Generalized Fourier Interpolation of Nonstationary Seismic Data." *CREWES Sponsor's Meeting 2010* (2010).

Nur, Amos. M., Joel. D. Wallis, Kenneth. Winkler, and John DeVilbiss. "Effects of Fluid Saturation on Waves in Porous Rock and Relations to Hydraulic Permeability." *SPE Journal* 20 (1980): 450–458.

Odebeatu, Emeka, Jinghua Zhang, Mark Chapman, and Xiang-Yang Li. "Application of spectral decomposition to detection of dispersion anomalies associated with gas saturation." *The Leading Edge* February (2006): 206–210.

O'Doherty, R. F. and N. A. Anstey. "Reflections on Amplitudes." *Geophysical Prospecting* 19 (1971): 430–458.

Pinnegar, C. R. "Polarization analysis and polarization filtering of three-component signals with the time-frequency S transform." *Geophysical Journal International* 165 (2006): 596–606.

Pinnegar, C. R. and D. W. Eaton. "Application of the S transform to prestack noise attenuation filtering." *Journal of Geophysical Research* 108 (2003).

Pinnegar, C. Robert and Lalu Mansinha. "The S-transform with windows of arbitrary and varying shape." *Geophysics* 68 (2003): 381–385.

Pratt, R. Gerhard. "Seismic waveform inversion in the frequency domain, Part 1: Theory and verification in a physical scale model." *Geophysics* 64 (1999): 888–901.

Quan, Youli and Jerry M. Harris. "Seismic tomography using the frequency shift method." *Geophysics* 62 (1997): 895–905.

Quintal, Beatriz, Stefan M. Schmalholz, and Yuri Y. Podladchikov. "Low-frequency reflections from a thin layer with high attenuation caused by interlayer flow." *Geophysics* 74 (2009): Y7–Y7.

Reine, Carl, Mirko van der Baan, and Roger Clark. "The robustness of seismic attenuation measurements using fixed- and variable-window time-frequency transforms." *Geophysics* 74 (2009): WA123–WA135.

Ren, H., G. Goloshubin, and F. J. Hilterman. "Poroelastic analysis of amplitude-versus-frequency variations." *Geophysics* 74 (2009): N49–N54.

Sheriff, R. and L. Geldart. *Exploration Seismology.* 2nd edition. Cambridge University Press, 1995.

Spencer, T. W., J. R. Sonnad, and T. M. Butler. "Seismic Q—Stratigraphy or dissipation." *Geophysics* 47 (1982): 16–24.

Stewart, Robert. *Vertical Seismic Profiling : the one-dimensional forward and inverse problems*. Massachusetts Institute of Technology, 1983.

Stewart, Robert R. "VSP: An in-depth seismic understanding." *CSEG Recorder* September (2001): 79–83.

Stockwell, R. G., L. Mansinha, and R. Lowe. "Localization of the complex spectrum: The S transform." *IEEE Trans. Signal Process* 44 (1996): 2957–2962.

Tarantola, Albert. "Inversion of seismic reflection data in the acoustic approximation." *Geophysics* 49 (1984): 1259–1266.

Tian, Fang, Shu min Chen, Er hua Zhang, Jing huai Gao, Wen chao Chen, Zhi yu Zhang, and You ming Li. "Generalized S transform and its applications for analysis of seismic thin beds." *SEG Technical Program Expanded Abstracts* 21 (2002): 2217–2220.

Toksoz, M. Nafi. and David H. Johnston. *Seismic Wave Attenuation*. Society of Exploration Geophysicists, 1981.

Tonn, Rainer. "The Determination of the seismic quality factor Q from VSP data: a comparison of different computational methods1." *Geophysical Prospecting* 39 (1991): 1–27.

Vasheghani, Fereidoon. *Seismic estimation of heavy oil viscosity*. PhD thesis, University of Calgary, 2011.

Vasheghani, Fereidoon and Laurence Lines. "Viscosity and Q in heavy-oil reservoir characterization." *The Leading Edge* July (2009): 856–860.

White, J. E. "Reflections from lossy media." *Journal of the Acoustical Society of America* 38 (1965): 604–607.

Wu., X., M. Chapman., A. Wilson., and Li. Xi. "Estimating seismic dispersion from pre-stack data using frequency-dependent AVO inversion." *SEG Expanded Abstracts* 29 (2010): 425–429.

Yang, Yushan, Yuanyuan Li, and Tianyou Liu. "1D viscoelastic waveform inversion for Q structures from the surface seismic and zero-offset VSP data." *Geophysics* 74 (2009): WCC141–WCC148.

Zhang, Zimin. *Assessing attenuation, fractures, and anisotropy using logs, vertical seismic profile, and three-component seismic data: heavy oilfield and potash mining examples.* University of Calgary, 2010.